Università degli studi ROMA TRE

SCUOLA DOTTORALE IN INGEGNERIA
Dottorato di ricerca in Scienze dell’Ingegneria Civile
XXI Ciclo

Tesi di Dottorato

Modellazione numerica delle inondazioni fluviali

Numerical modelling of fluvial inundations

Dottorando: Ing. Pietro Prestininzi
Docente guida: Prof. Guido Calenda
Coordinatore del dottorato: Prof. Leopoldo Franco

Roma, Febbraio 2009

Collana delle tesi di Dottorato di Ricerca
In Scienze dell’Ingegneria Civile
Università degli Studi Roma Tre
Tesi n° 24

Sommario

Lo scopo di questa tesi è quello di indagare diversi possibili approcci alla modellazione numerica delle inondazioni fluviali. L'approccio modellistico matematico adottato in questo lavoro è quello maggiormente accettato per la simulazione di inondazioni su larga scala ed è basato sull'utilizzo del set di equazioni dette "delle acque basse" (SWE, Shallow Water Equations), in forma bidimensionale.

La moltitudine e la complessità dei fenomeni che intervengono nella formazione di un evento di piena impone inevitabilmente di includere nella presente indagine solo alcuni di essi. In particolare si è voluto concentrare l'attenzione sulla caratterizzazione delle modalità di propagazione di un'inondazione.

In una <u>prima fase</u> si sono analizzate le tipologie di eventi in cui l'onda di espansione fosse di tipo non impulsivo, mossa quindi principalmente dalla forza gravitazionale. Tale classe di fenomeni rappresenta gran parte delle inondazioni che si verificano in natura: esondazioni fluviali, inondazioni di aree costiere dovute a correnti di marea, espansioni controllate dei corsi d'acqua in bacini di laminazione, sono solo alcuni esempi. Questa restrizione operata sulla tipologia di eventi analizzati, se esclude una modesta fetta di fenomeni di interesse, consente d'altra parte di operare semplificazioni notevoli al set delle SWE. Dalla forma originaria delle SWE, rappresentata da una set di equazioni differenziali alle derivate parziali (PDE, Partial Differential Equations) di tipo iperbolico, si può dedurre un sistema semplificato di forma parabolica, (PSWE). Grazie a queste assunzioni il sistema originario, la cui soluzione numerica risulta pesante e spesso non applicabile a problemi di larga scala, diviene più facilmente gestibile e consente di allocare le risorse di calcolo resesi disponibili ad aspetti più importanti, quali ad esempio una dettagliata descrizione topografica o una più accurata modellazione delle condizioni al contorno.

La limitazione del campo di applicabilità delle PSWE, se interpretabile dal punto di vista analitico grazie ad alcune semplificazioni, non si riflette in una netta distinzione negli eventi naturali. L'eterogeneità dei fenomeni e la loro rapida evoluzione sfuma i contorni che si tenta di tracciare. E' stato quindi necessario verificare l'accuratezza del modello non inerziale nel riprodurre un'inondazione fortemente impulsiva, simulata grazie ad un prototipo in scala. La quantificazione dell'errore derivante dal confronto con un esperimento controllato è generalizzabile a eventi su

scala reale, e consente quindi l’applicazione di tali modelli in modo più consapevole.

Una seconda parte della tesi ha riguardato lo sviluppo di un codice per la risoluzione delle SWE in forma completa adottando tecniche numeriche all’avanguardia. In particolare si è concentrata l’attenzione sulla capacità di tali modelli di simulare eventi fortemente impulsivi, nei quali si osserva la formazione e la propagazione di discontinuità nelle grandezze caratteristiche. L’approccio numerico conduce alla frontiera della ricerca in questo campo e pone problematiche stimolanti, alle cui soluzioni già proposte in letteratura si è tentato di apportare contributi innovativi. Si è indagata la capacità di mantenere un alto ordine di accuratezza anche in presenza di termini sorgente di pendenza e attrito al fondo, in concomitanza con transizioni asciutto-bagnato. L’inclusione nel modello concettuale del fenomeno del risalto idraulico, matematicamente interpretato come discontinuità e numericamente colto grazie a schemi shock-capturing, esacerba le questioni di propagazione su fondo asciutto e di gestione di topografie accidentate. La trattazione delle transizioni asciutto-bagnato è sempre risultato un aspetto critico della modellazione numerica delle SWE. Spesso le strategie adottate si sono rivelate farraginose e artificiose. Si è quindi proposto un approccio più fisicamente basato, che minimizza l’utilizzo di artifici numerici che spesso inficiano l’accuratezza propria degli complessità degli schemi numerici avanzati. Le soluzioni proposte sono quindi validate mediante il confronto con dati sperimentali e analitici.

Abstract

The scope of this thesis is to investigate different possible approaches to the numerical modelling of fluvial floods. The mathematical model adopted is most commonly used for large scale inundations, based on the bidimensional SWE (Shallow Water Equations).

The number and complexity of phenomena involved in a flood event obliges to focus only on some of them. Therefore major attention has been paid to the characterization of the modalities of propagation.

In the first part of the thesis non-impulsive inundation waves have been analyzed, where the gravitational force prevails over the inertial one. These features can be found in most of the natural flood events such as fluvial overflows, tidal inundations of coastal areas, controlled flow over flood expansion fields. Even if this restriction on the type of events excludes some of events of interest, it yields important simplifications to the SWE set. These assumptions allow to pose the original hyperbolic set of PDE (Partial Differential Equations) into a parabolic form. The complete SWE set, whose numerical solution is still computationally demanding so that its application to real cases is quite challenging, becomes more easily manageable and allows to assign the saved computational resources to the accurate modelling of some essential aspects such as the description of topography, boundary conditions and resistance forces.

The applicability restrictions of the PSWE, if theoretically deductable with some simplifications, does not provide clear criteria applicable to real world events. The extreme heterogeneity and their rapid time variability makes these criteria even more difficult to use. It then became necessary to verify the accuracy of the diffusive model when simulating a highly inertial inundation wave, reproduced with a physical experiment.

The second part of the thesis deals with the development of a numerical code to solve the full dynamic form of the SWE, making use of the latest numerical techniques available. The attention has been focused on the ability of these kind of models to simulate highly impulsive floods, where the formation and the propagation of physical shocks often occur. The shock-capturing numerical approach leads to the frontier of the research in this topic and yield several issues whose solution was given some innovative contributions in this thesis. The ability of maintaining a high order of accuracy was assessed, even when source terms as bed and friction slope are to be modelled. The inclusion of the hydraulic bore modelling, mathematically interpreted as a shock, exacerbates the issues

related to the propagation over dry bed, especially when dealing with complex topography. The wet-dry transitions, always a crucial topic in the SWE numerical treatment, have been here managed in a way that minimizes the use of procedures whose lack of numerical foundation often ruins the accuracy of the overall scheme. The proposed results were then validated by means of comparisons with both experimental and analytical solutions.

Contents

List of Figures

List of Tables

Notation

Operators:

$\nabla \cdot \bullet \rightarrow$ divergence

$\frac{\mathrm{D}\bullet}{\mathrm{D}t} \rightarrow$ material derivative

$\vec{\nabla} \rightarrow$ gradient

$\nabla^2 \bullet \rightarrow$ laplacian

$\bullet_k \rightarrow$ partial spatial derivative along kth direction

Symbols:

$\bullet^{(k)} \rightarrow$ kth element in a series

$\bullet' \rightarrow$ nondimensional quantity

$\underline{\bullet} \rightarrow$ tensor (bold character for vectorial quantities)

Abbreviations:

GW → Gravity Wave
IVP → Initially Value Problem
KW → Kinematic Wave
NIW → NonInertia Wave
NSE → Navier Stokes Equations
ODE → Ordinary Differential Equations
PDE → Partial Differential Equations
PSWE → Parabolic Shallow Water Equations
SWE → Shallow Water Equations
QSW → Quasi steady Wave

Quantities:
(the ones non listed here are defined in the text)

$x, y, z \rightarrow$ spatial coordinates $(x \;\; y \;\; z) = \mathbf{x}$

$\mathbf{V} \rightarrow$ velocity field

$u, v, w \rightarrow$ velocity components along spatial coordinates $(u \;\; v \;\; w) = \mathbf{V}$

$t \rightarrow$ time

$\rho \rightarrow$ density

$p \rightarrow$ pressure

$\bar{\mu} \rightarrow$ dynamic viscosity

$\bar{\mathbf{G}} \rightarrow$ vector $\begin{pmatrix} 0 & 0 & -g \end{pmatrix}$

$\varphi^{(n)} \rightarrow$ n^{th} element in the expansion series of the velocity potential

1. Introduction

1.1 Environmental Hydraulics

Many natural systems such as sea, rivers and lakes area the places where water flows mainly in the form of free surface flows. A large amount of complex phenomena takes place in these environments and is the main topic of Environmental Hydraulics. Most of them have a close influence on humans' everyday life, such as, water supply planning, irrigation management, pollution dispersion, erosion, biodiversity preservation, etc. Other more particular topics can be perceived as not directly influencing our lives, but are at least equally worth given close attention. Large sea currents path, flows within lakes, tsunami waves generation, inundation waves propagation, are only a few of those topics which have been considered to be essentially basic research and without a direct impact on decision planning of human activities. A change of this point of view occurred in the last decades, and is still going on, as these large scale studies have become more accessible to the average researcher. In fact when the numeric analysis, whose bases indeed date back to the 19th century, found its possible application tools in the 70's spread of computational facilities (at least in the new continent), the research in this field was given a great acceleration. Another successive but independent occurrence that enhanced the raise of the Applied Environmental Hydraulics was the chain of hydraulic extreme events that took place in the last decade. Inundations, tsunamis, droughts, hurricanes, more and more often come to our knowledge. Is it because some sort of climate change is currently going on, is it because people are just more aware of them, is it because we are forced to interfere with them due to a lack of resources (land, water, etc.), but the world seems to be at their mercy. The reasons, though interesting and stimulating, are not the topic of this work. The duty of scientists in Environmental Hydraulics is to find mitigations to those effects, essentially predicting their occurrence, where possible, and assessing their risk. This is generally accomplished by means of a model, which is the main instrument of interpreting the reality.

1.2 Model Development and improvement

> *Ritengo che compito della teoria sia costruire un'immagine del mondo esterno che esiste solo in noi, che ci serva da guida in tutti i nostri pensieri ed esperimenti; cioè, per così dire, ci serva da guida nel compimento del processo di ragionamento, la cui realizzazione è, in grande, ciò che nella creazione di ogni idea in noi si compie in piccolo... La prima elaborazione e il costante perfezionamento del modello è quindi il compito principale della teoria. La fantasia è sempre la sua culla, l'intelletto vigile il suo educatore (Boltzmann,*
> *Sul significato delle teorie,*
> *Graz 16/07/1890).*

The model is the natural way the human being perceives the reality. When the brain is stimulated by an external event, it naturally filters out all those stimulations which are thought not to be relevant for interpreting the event. This filter is mainly based on previous experiences. This unconscious process is consciously resembled every time we try to explain a natural phenomenon. The concept of model as the main tool to interpret reality can be found in Kant (1787) as the *schema*: it is the bridge between sensitivity and intellect which is used for processing the exterior *sensible* forms, by means of abstract, *pure* concepts of the mind.

The construction of models as a basis of the comprehension is then adopted in every field of human knowledge, and has found its codification in the scientific fields. Variegated phenomena in fact require a careful and precise inspection aimed at isolating the most important features of an observable fact, and relate them to simulate it. As the understanding of the phenomenon improves, together with the methods of analysis, features are added to or taken away from the model. The power of the comprehension by means of a model is that the process is theoretically self-refining, as new information acquired improves model quality. The prediction capacities of the model are continuously compared to new events and this contrast deeply contributes to the critical appraisal of model performances and is a crucial part of the model improvement.

1.3 The role of numerical modelling in the Hydraulic Risk Assessment (HRA) field

Numerical modelling is nowadays a crucial stage in the field of Environmental Hydraulic. The developing of efficient and accurate numerical techniques, together with the large availability of computational facilities, have made numerical models accessible to designers and engineers. Numerical modelling has gained such a central role thanks to its capacity to provide the required objective characterization of many complex phenomena. Numerical models do not provide solution to problems, but can guide the designer towards optimised results, or give support to statements which, otherwise, would need to be confirmed through other much more tortuous ways (mainly physical modelling). Unfortunately, the *chimera* that a numerical model can be applied to complex problems in the same way a calculator is used to solve a sudoku game, is still present. The complexity of the problems for which these models are built for, forces the final users to be extremely competent in the specific field, and aware of all the assumptions which lie beneath the surface of the numerical approach.

If compared to other hydraulic fields, such as industrial processes and aerodynamics, the application of the numerical models to natural problems is relatively young. It can be dated back to the late 90s, though the mathematical characterization of the processes is much older. This delay can be due to different causes. First of all the heterogeneity of the phenomena involved force the analyst to interact with other specialists, e.g. the groundwater engineer whose research field is the contaminant diffusion must cope with the hydrogeologist and chemist. Another reason can be related to the uncertainty coming from input data, as it is generally huge for events that massively span in space and time, and these models are seldom developed to provide a stochastic characterization of results. Another factor is the deep peculiarities that distinguish every single case in environmental hydraulics: the design of an innovative foil keel shape can be carried out by means of standard, though sophisticated, numerical codes; the determination of a runoff hydrograph for a 100 km^2 basin generally does not follow the same procedure employed for larger basins:

the phenomena that occur are basically the same, but scale effects are difficult to account for in a single model. Finally, as these instruments are often developed to optimize solutions in very critical fields, there is some kind of reluctance, especially on the public administration side, in adopting a tool that makes use of the latest numerical method. For the sake of truth it must be said that this unwillingness is constantly decreasing.

The HRA field is actually the composition of many other subareas, e.g. the meteorological, rainfall-runoff, underground water, fluid dynamics analysis, can all be further divided into other categories. All of these presently make large use of numerical techniques.

This thesis is in the *flood simulation* area, whose purpose is to study the propagation of inundation waves originating from different sources: fluvial flows, rupture of retention structures, inundation of coastal areas caused by tidal oscillations. Its contents will be introduced in the next sections.

1.4 Objectives and outline of this thesis

The first attempts to apply numerical simulations to the flood propagation subject can be traced back to the 60s (Isaacson et al. 1958, Martin et al. 1969, 1971, Cunge et al. 1964, 1980, Price 1974, Katopodes and Strelkoff 1977, Abbot 1979). Notwithstanding the half century of work in the field, the topic is still "*in fieri*" and its evolution has undergone steep jumps in the last decade. The reasons of these sudden accelerations can be ascribed to external contributions coming from other disciplines, mainly gas dynamics. The area is still fertile to original contributions, principally oriented to analyse the applicability of the models to real scale events. A question is well likely to emerge in this context, and regards the level of complexity of the mathematical-numerical approach justifiable by the level of uncertainty of input data. Moreover this complexity needs to be even more firmly guided by the accuracy of the prediction required by the type of analysis for which the model is employed.

The almost entire research in the field of numerical simulations of flood propagation is based on the set of the SWE. This set of equations can be derived from the Navier-Stokes Equations (NSE) with some assumptions on the entity of free surface perturbations (see section 2.1 for details). These assumptions are justified by the observation of the natural behaviour of inundation waves, where the flows involved are predominantly horizontal and the flooded areas area generally much larger than the water depth. Further observation of such phenomena reveal that a considerably large part of the flood events are characterized by spatially and temporally low variation of the velocity field. Moreover, the events where the velocity field clearly shows large gradients and fast variations, often exhibit this peculiarities only in restricted parts of their space-time domain. The SWE, indeed, account for the correct representation of this inertial behaviour, thus the aforementioned question strongly emerges: is it always necessary to include this effects in the conceptual model? Additionally, it is worth asking what payback would be gained if a model was built without including those effects. This thesis will deal with those (and more) questions in its first part: the parabolic approximation of the SWE (PSWE), which consists in neglecting the inertial contributes to the motion of a mass of fluid, is presented and discussed. A numerical model able to solve the PSWE is developed and the applicability range of the parabolic approximation is verified with the application to a controlled physical experiment.

In the second part of the thesis a further model is developed, which is able to solve the complete form of the SWE, making use of the latest numerical techniques available. The model is then validated against some analytical solutions and a laboratory experiment. The complexity of the methods required by the full dynamic version of the SWE makes the applicability of the model to large scale events more difficult, which, incidentally, justifies the use of simplified models such as the PSWE. Some new ideas to deal with the peculiar problems of the numerical methods employed to solve the SWE are presented.

2. Shallow Water Models

> *“Così può accadere che il matematico, continuamente occupato con le sue formule e accecato dalla loro perfezione intrinseca, prenda le correlazioni di queste fra loro per ciò che esiste veramente e distolga lo sguardo dal mondo reale (Boltzmann,*
> *Sul significato delle teorie,*
> *Graz 16/07/1890).*

2.1 Deduction of the SWE set

In this chapter the SWE set will be deduced from the Navier Stokes Equations (NSE). The latter is the most general set of PDE describing the variation of the velocity field in a continuous fluid due to the action of body and surface forces. The NSE can be easily derived from the basic principles of conservation of mass and momentum. The tensorial form of the NSE for incompressible newtonian fluids is:

$$\begin{aligned} &\nabla \cdot \mathbf{V} = \mathbf{0} \\ &\rho \frac{\mathrm{D}\mathbf{V}}{\mathrm{D}t} = -\vec{\nabla} p + \rho \bar{\mathbf{G}} + \overline{\mu} \nabla^2 \mathbf{V} \end{aligned} \tag{2.1}$$

The classical way of deriving the SWE is to make some assumptions on the distribution of the velocity/pressure to simplify the integration along the vertical direction. The most straightforward is to assume a negligible vertical acceleration

$$\frac{\partial w}{\partial t} = 0 \Rightarrow \frac{\partial p}{\partial z} = -\rho g \tag{2.2}$$

Here a different and quite uncommon (at least in the fluvial hydraulics) approach is presented, which instead does not make any assumption on the kinematic quantities or their distribution (Mei 1999). The essence of this more elegant derivation is that it is possible to show that some peculiarities of the SWE are actually consequence of the kind of phenomena we want to model. For this purpose it is not necessary to work on the full form of the NSE: in (2.1) the viscous stress term $\mu \nabla^2 \mathbf{V}$ can be dropped to obtain the so-called Euler equations. Under the assumption of conservative mass and pressure fields acting on the fluid, the vorticity is constant in time in force of the Kelvin Theorem. If the velocity field is initially irrotational, Euler equations will keep the vorticity null through time; the scalar potential ϕ of the harmonic field $\mathbf{V}$ therefore satisfies Laplace equation:

$$\mathbf{V}=\vec{\nabla}\phi\Rightarrow\nabla^2\phi=0 \tag{2.3}$$

as can be easily deduced using the mass continuity equation (2.1). Differentiation will be substituted by subscript notation from here on.

Aiming at solving free surface problems, eq (2.3) needs specific boundary conditions for $z=\eta$; bottom is here considered flat and horizontal so that the corresponding boundary condition can be specified at $z=-h$:

$$\phi_z=\eta_t+\eta_x\phi_x+\eta_y\phi_y\leftarrow z=\eta \tag{2.4}$$

$$\phi_t+\left(\phi_x{}^2+\phi_y{}^2+\phi_z{}^2\right)=0\leftarrow z=\eta \tag{2.5}$$

$$\phi_z=0\leftarrow z=-h \tag{2.6}$$

It is necessary to define two nondimensional parameters:

$$\begin{aligned}\mu&=\frac{h}{L}\\ \varepsilon&=\frac{A}{h}\end{aligned} \tag{2.7}$$

The analysis can be made clearer if the quantities are made nondimensional, so the following definitions are posed (nondimensional quantities are referred to with prime notation):

$$\begin{aligned} &x',y'=\frac{x,y}{L}\\ &z'=\frac{z}{h}\\ &\eta'=\frac{\eta}{A}\\ &t=t\frac{c}{L}\\ &\phi'=\phi\bigg/\frac{ALc}{h} \end{aligned} \tag{2.8}$$

where the velocity potential has been made nondimensional using the amplitude of potential oscillations of the linear theory ($\varepsilon<<1$), depending on the wave length L, the wave amplitude *A*, the undisturbed depth *h*, the linear celerity *c*. The derivation of nondimensional velocity components leads to the following expressions:

$$\begin{bmatrix} u\\ v\\ w \end{bmatrix}=\begin{bmatrix} \phi_x\\ \phi_y\\ \phi_z \end{bmatrix}=\frac{Ac}{h}\begin{bmatrix} u'\\ v'\\ \frac{L}{h}w' \end{bmatrix}=\frac{Ac}{h}\begin{bmatrix} \phi'_{x'}\\ \phi'_{y'}\\ \frac{L}{h}\phi'_{z'} \end{bmatrix} \tag{2.9}$$

Substituting (2.9) into (2.3), (2.4), (2.5), (2.6) , and making use of definitions (2.7) respectively results into:

$$\mu^2\left(\phi'_{x'x'}+\phi'_{y'y'}\right)+\phi'_{z'z'}=0\leftarrow z'\in\left(-1,\varepsilon\eta'\right) \tag{2.10}$$

$$\phi'_{z'}=\mu^2\left(\eta'_{t'}+\varepsilon\eta'_{x'}\phi'_{x'}+\varepsilon\eta'_{y'}\phi'_{y'}\right)\leftarrow z'=\varepsilon\eta' \tag{2.11}$$

$$\phi'_{t'}+\frac{Ag}{2c^2}\left[\phi'^{\,2}_{x'}+\phi'^{\,2}_{y'}+\left(\frac{\phi'_{z'}}{\mu}\right)^2\right]=0\leftarrow z'=\varepsilon\eta' \tag{2.12}$$

$$\phi'_{z'}=0\leftarrow z'=-1 \tag{2.13}$$

Prime notation will be dropped from here on.

The essence of this approach resides in the expansion of ϕ as a power series of z :

$$\phi(x,y,z,t)=\sum_{n=0}^{\infty}(z+1)^n\varphi^{(n)}(x,y,t) \tag{2.14}$$

the following expressions result from simple successive differentiations:

$$\begin{aligned}
\phi_{x,y}&=\sum_{n=0}^{\infty}(z+1)^n\frac{\partial\varphi^{(n)}}{\partial(x,y)}\\
\phi_{xx,yy}&=\sum_{n=0}^{\infty}(z+1)^n\frac{\partial^2\varphi^{(n)}}{\partial\left(x^2,y^2\right)}\\
\phi_{z}&=\sum_{n=0}^{\infty}(z+1)^n(n+1)\varphi^{(n+1)}\\
\phi_{zz}&=\sum_{n=0}^{\infty}(z+1)^n(n+2)(n+1)\varphi^{(n+2)}
\end{aligned} \tag{2.15}$$

substituting (2.15) into (2.10) yields:

$$\sum_{n=0}^{\infty}(z+1)^n\underbrace{\left[\mu^2\left(\varphi_{xx}^{(n)}+\varphi_{yy}^{(n)}\right)+(n+2)(n+1)\varphi^{(n+2)}\right]}_{k_n}=0 \tag{2.16}$$

As the entire sum must be null $\forall z\in(-1,\varepsilon\eta)$, and being k_n independent of z , it follows that each k_n must be null, leading to a recursive definition for φ_n :

$$\varphi_{n+2}=\frac{-\mu^2\left(\varphi_{xx}^{(n)}+\varphi_{yy}^{(n)}\right)}{(n+2)(n+1)}\quad\forall n \tag{2.17}$$

Using bottom boundary condition (2.13) into the third of eq (2.15) it can be shown that $\varphi^{(1)}=0$; (2.17) then allows to state that the series has null terms for odd values of n. Every term in the expansion (2.14) can be thus made dependent only on $\varphi^{(0)}$:

$$\phi=\sum_{n=0}^{\infty}\frac{(-1)^n\mu^{2n}}{2n!}\left(z+1\right)^{2n}\nabla_{xy}^{2(n)}\varphi^{(0)} \tag{2.18}$$

where the operator $\nabla_{xy}^{2(n)}$ means n applications of Laplacian operator restricted to the xy plane $\nabla_{xy}^{2}\square=\left(\square_{xx}+\square_{yy}\right)$. It is worth noting that in the original expansion (2.14) the magnitude of each term φ_n was not a priori decreasing with n (it was introduces as a Taylor expansion). This is only true in eq. (2.18), provided $\mu<1$. The expansion can be thus seen as a perturbation method for the potential field, with $\varphi^{(0)}$, the leading term, still unknown. Note that $\varphi^{(0)}$ is the value of ϕ at the bottom and the non dimensional horizontal velocities are $\mathbf{u}_0=(u_0\ v_0)=\vec{\nabla}\phi\big|_{z=-1}=\vec{\nabla}\varphi^{(0)}$. Substituting derivatives of ϕ based on eq. (2.18) into surface boundary conditions (2.11) and (2.12), and writing potential spatial derivatives as function of u_0, the expressions for the distributions of horizontal velocities and pressure along z are:

$$\begin{aligned}
&(u\ v)=\vec{\nabla}\phi=\mathbf{u}_0-\frac{\mu^2}{2}(z+1)^2\vec{\nabla}\nabla\cdot\mathbf{u}_0+O\left(\mu^4\right)\\
&w=\phi_z=-\mu^2(z+1)\nabla\cdot\mathbf{u}_0+O\left(\mu^4\right)\\
&\frac{p}{\rho c^2}=(\varepsilon\eta-z)-\frac{\varepsilon\mu^2}{2}\left[(\varepsilon\eta+1)^2-(z+1)^2\right]\left\{\nabla\cdot\mathbf{u}_{0t}+\varepsilon\left[\mathbf{u}_0\cdot\nabla^2\mathbf{u}_0-(\nabla\cdot\mathbf{u}_0)^2\right]\right\}+O\left(\mu^4\right)
\end{aligned} \tag{2.19}$$

It is now possible to show that the SWE are the 3D Euler equations, expanded with respect to μ and truncated to the first order. This truncation obviously is allowed only if $\mu<<1$, that is the perturbations can be considered “long waves”. This means that only the first terms in the right members of (2.19) are non null: the horizontal velocities are constant and equal to the velocity at the bottom; the vertical velocity does not have any term proportional to $O(\mu)=O(1)$ and is therefore null; the pressure is proportional to $-z$ and is null at $z=\varepsilon\eta$, i.e. is hydrostatic. This derivation, which may, and probably is, slightly tedious, is formally more coherent to the concept of “model” explained in section 1.2 if compared to the classical ones: in fact here the purpose of the analyst, i.e. the study of long waves, is the factor that leads the search of a suitable model. Moreover it’s the observation of an evident feature (the wave length) that influences the construction of the model. The resulting model can be extended to the desired precision, just including higher order terms. The error committed neglecting each term can be evaluated as a function of wave length μ . The SWE are the lowest order possible.

2.2 Properties of the SWE

As seen in the previous section, the SWE are a possible solution of the NSE feasible if one is interested in studying free surface problems with depth small with respect to wave perturbations’ length. No proviso has been made on wave amplitude, so the equations derived are non linear.

In view of successive needs, it is here necessary to stress the peculiar form of the equations just derived. As stated above the NSE are derived as conservation laws of a finite mass of fluid. This means that the quantities (such as mass, momentum or energy) are balanced within a control volume. This way of deducing balance laws leads to an integral form of the equations. The equations (2.1) are indeed formulated as local or differential equations. To understand the difference between these two formulations it is possible to examine a general conservation law for a scalar q in a multidimensional space:

$$\frac{\partial}{\partial t}\int_{\Omega} q(\mathbf{x},t)dv=\int_{\partial\Omega}\mathbf{f}(\mathbf{x},t)\cdot\hat{n}dA \tag{2.20}$$

This is the natural integral form emerging from balance principles over a control volume Ω whose measure is v , and $\mathbf{f}$ is the flux across the boundary of Ω. In general, integral forms of conservation laws are more difficult to handle, and are often recast into differential form. To obtain a differential form, eq (2.20) can be rewritten as:

$$\int_{\Omega} \frac{\partial}{\partial t} q(\mathbf{x},t) dv = \int_{\Omega} \nabla \cdot \mathbf{f}(\mathbf{x},t) dv \qquad (2.21)$$

Eq. (2.21) must be valid for any volume Ω, so the integrand of both members must be equal as well:

$$\frac{\partial}{\partial t} q(\mathbf{x},t) = \nabla \cdot \mathbf{f}(\mathbf{x},t) \qquad (2.22)$$

which is the differential form of the original integral law.
The crucial point is that some assumptions must be made in order to allow the derivation of (2.21) from (2.20): the functions q and $\mathbf{f}$ must have continuous partial derivatives (i.e. must be smooth) in the volume Ω. This implies that all the functions that will develop discontinuities (such as shocks) are not solutions of (2.22) while being still solutions of (2.20). This deep difference must be taken into account when such solutions are encountered.

In order to illustrate the eigenstructure of the SWE, their differential form is here recalled in terms of conserved variables $(h \;\; uh \;\; vh)$:

$$\frac{\partial \mathbf{U}}{\partial t} + \nabla \cdot \underline{\underline{\mathbf{E}}} = \mathbf{S} \qquad (2.23)$$

where the vector of conserved variables is:

$$\mathbf{U} = \begin{pmatrix} h \\ uh \\ vh \end{pmatrix} = \begin{pmatrix} u_1 \\ u_2 \\ u_3 \end{pmatrix} \qquad (2.24)$$

the matrix of fluxes is:

$$\underline{\mathbf{E}}=(\mathbf{F}\ \mathbf{G})=\begin{pmatrix} u_2 & u_3 \\ u_2^2/u_1+gu_1^2/2 & u_2u_3/u_1 \\ u_2u_3/u_1 & u_3^2/u_1+gu_1^2/2 \end{pmatrix}=\begin{pmatrix} hu & hv \\ hu^2+gh^2/2 & huv \\ huv & hv^2+gh^2/2 \end{pmatrix} \tag{2.25}$$

the vector of source terms is:

$$\mathbf{S}=\begin{pmatrix} s_1 & s_2 & s_3 \end{pmatrix} \tag{2.26}$$

Given the SWE are spatially 2D, two different Jacobian matrices arise, namely:

$$\underline{\mathbf{A}}(\mathbf{U})=\begin{pmatrix} 0 & 1 & 0 \\ c^2-u^2 & 2u & 0 \\ -uv & v & u \end{pmatrix} \tag{2.27}$$

$$\underline{\mathbf{B}}(\mathbf{U})=\begin{pmatrix} 0 & 0 & 1 \\ -uv & v & u \\ c^2-v^2 & 0 & 2v \end{pmatrix} \tag{2.28}$$

where $c=\sqrt{gh}$. Their eigenvalues are respectively given by:

$$\begin{aligned} \lambda_1^x &= u-c=\frac{u_2}{u_1}-c & \qquad \lambda_1^y &= v-c=\frac{u_3}{u_1}-c \\ \lambda_2^x &= u=\frac{u_2}{u_1} & \lambda_2^y &= v=\frac{u_3}{u_1} \\ \lambda_3^x &= u+c=\frac{u_2}{u_1}+c & \lambda_3^y &= v+c=\frac{u_3}{u_1}+c \end{aligned} \tag{2.29}$$

The eigenvectors $\mathbf{R}^{(i)}$ are the solutions to the systems:

$$\underline{\mathbf{A}}\mathbf{R}^{(i)}=\lambda_i\mathbf{R}^{(i)} \tag{2.30}$$

$$\underline{\mathbf{B}}\mathbf{R}^{(i)}=\lambda_i\mathbf{R}^{(i)} \tag{2.31}$$

If a linear combination of these matrices is constructed with non-zero vectors of coefficients:

$$\underline{\mathbf{C}}(\mathbf{U})=a\underline{\mathbf{A}}(\mathbf{U})+b\underline{\mathbf{B}}(\mathbf{U}) \tag{2.32}$$

the SWE system is said to be *hyperbolic* if the eigenvalues of $\underline{\mathbf{C}}$ are all real, and *strictly hyperbolic* if, in addition, they are all distinct. These eigenvalues are easily obtainable as:

$$\begin{aligned} \lambda_1^{\underline{\mathbf{C}}} &= au+bv-c\sqrt{a^2+b^2} \\ \lambda_2^{\underline{\mathbf{C}}} &= au+bv \\ \lambda_3^{\underline{\mathbf{C}}} &= au+bv+c\sqrt{a^2+b^2} \end{aligned} \tag{2.33}$$

Thus the SWE are:

i *hyperbolic* if $h\geq 0 \Rightarrow c\geq 0$
  i.1 *strictly hyperbolic* for $h>0 \Rightarrow c\neq 0$
ii *non-hyperbolic* for $h<0 \Rightarrow c\notin \mathrm{R}$

From here on the x-split 2D SWE will be analysed, namely

$$\mathbf{U}_t+\mathbf{F}_x=\mathbf{0} \tag{2.34}$$

The eigenvectors emerging from definition (2.30) and the x-eigenvalues in (2.29), are the following:

$$\begin{aligned} \mathbf{R}^{(1)} &= \alpha\begin{pmatrix}1 & u-c & v\end{pmatrix}=\alpha\begin{pmatrix}1 & \frac{u_2}{u_1}-\sqrt{gu_1} & \frac{u_3}{u_1}\end{pmatrix} \\ \mathbf{R}^{(2)} &= \beta\begin{pmatrix}0 & 0 & 1\end{pmatrix} \\ \mathbf{R}^{(3)} &= \gamma\begin{pmatrix}1 & u+c & v\end{pmatrix}=\gamma\begin{pmatrix}1 & \frac{u_2}{u_1}+\sqrt{gu_1} & \frac{u_3}{u_1}\end{pmatrix} \end{aligned} \tag{2.35}$$

Not accounting for the loss of hyperbolicity due to the presence of negative non-physical depth (condition *ii*), condition *i* assures that the eigenvectors are independent so that each of them defines a vectorial field in the phase space. For the SWE the dimension of this space is 3. Each eigenvalue defines a scalar field in the same space. In order to investigate the nature of the characteristic fields of the system of equations, it is necessary to compare the vectorial field of every eigenvector with the vectorial field defined by the gradient of the correspondent eigenvalue: if their scalar product is null, namely

$$\nabla\lambda_i(\mathbf{U})\cdot\mathbf{R}^{(i)}(\mathbf{U})=0 \quad \forall\mathbf{U} \tag{2.36}$$

then the characteristic field is *linearly degenerate*. If the two vectors are never aligned, namely:

$$\nabla\lambda_i(\mathbf{U})\cdot\mathbf{R}^{(i)}(\mathbf{U})\neq 0 \quad \forall\mathbf{U} \tag{2.37}$$

then the characteristic field is *genuinely non-linear*.
Given eq. (2.29), the gradients are given by:

$$\begin{aligned}
\nabla\lambda_1^x &= \begin{pmatrix} -\dfrac{u_2}{u_1^2}-\dfrac{1}{2}\sqrt{\dfrac{g}{u_1}} & \dfrac{1}{u_1} & 0 \end{pmatrix}\\
\nabla\lambda_2^x &= \begin{pmatrix} -\dfrac{u_2}{u_1^2} & \dfrac{1}{u_1} & 0 \end{pmatrix}\\
\nabla\lambda_3^x &= \begin{pmatrix} -\dfrac{u_2}{u_1^2}+\dfrac{1}{2}\sqrt{\dfrac{g}{u_1}} & \dfrac{1}{u_1} & 0 \end{pmatrix}
\end{aligned} \tag{2.38}$$

Given the definitions (2.36) and (2.37), the SWE have a characteristic field *linearly degenerate* for λ_2 while eigenvalues λ_1 and λ_3 are associated with *genuinely non-linear* fields. The first type of fields comprises perturbations that travel with a non-linear speed $s_{x,y}=u,v\pm c$. The speed of the waves of the second type is instead equal to the advection velocity $s_{x,y}=u,v$.

2.2.1 The Riemann problem and its solution

The wave patterns described in the previous section appear in the solution of the so-called Riemann problem.

The Riemann problem is the initial value problem defined by the augmentation of eq (2.34) and the following initial conditions:

$$\mathbf{U}(x,0)=\begin{cases}\mathbf{U}_L \leftarrow x<0\\ \mathbf{U}_R \leftarrow x>0\end{cases} \tag{2.39}$$

As the above eigenstructure analysis states, three characteristic families can arise in the solution of the problem, each one associated with an eigenvalue. It is useful to illustrate the wave structure in the time-space plane as in Figure 2.1:

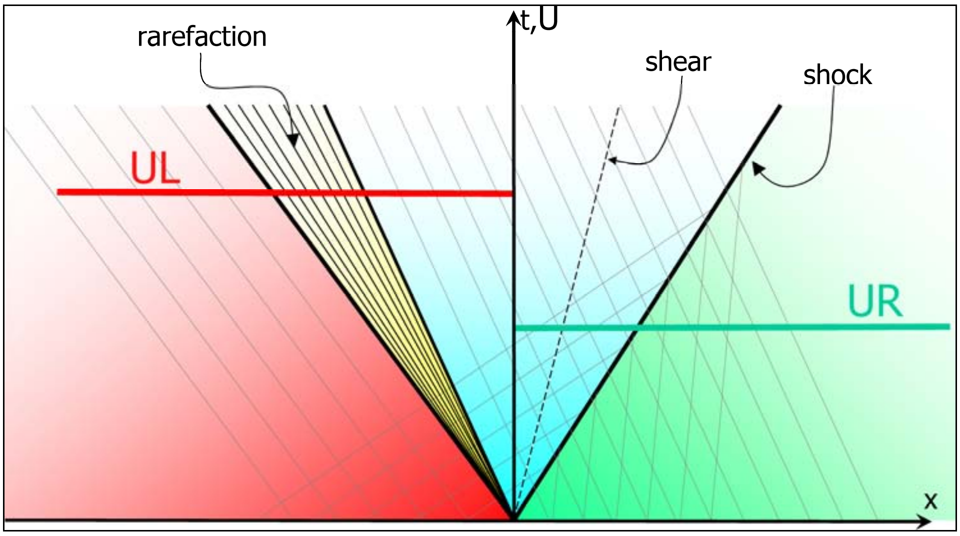

Figure 2.1 – Riemann problem and its solution in the (x, t-U) plane. Left and right wedges, red and green areas, where the initial conditions hold; star region, light blue, where the U is constant but unknown; rarefaction wave, in yellow, where U varies (linearly for the SWE).

The lines in the space-time plot refer to discontinuities of some of the variables. The left and right states define a family of characteristic lines (light gray traces in Figure 2.1) whose slope depends on the initial values (2.39). Obviously the left slope is generally different from right slope, thus a separation between the zones of influence of the two different conditions (2.39) must exist. This boundary is a wave in the x-t plane. The two external waves separate the *x-t* plane into 3 wedges: the left (right) one is the area where the initial left (right) condition still holds, thus $\mathbf{U}=\mathbf{U}_L$ ($\mathbf{U}=\mathbf{U}_R$) (i.e. no information on the perturbation that took place at *x=0* and *t=0* has yet arrived); the solution in the middle region (called *star* region) is actually unknown and depends on the values of $\mathbf{U}_L$ and $\mathbf{U}_R$. The two external wave can have two natures: a shock wave or a rarefaction wave (respectively a bore and a depression in the case of SWE). The respective compressive (bore) or expansive (depression) nature of the wave depends on the speeds of the characteristic fields it separates, namely the value of the two eigenvalues:

$$\begin{aligned} &\lambda_i\left(\mathbf{U}^-\right)<\lambda_i\left(\mathbf{U}^+\right)\Rightarrow \text{rarefaction} \\ &\lambda_i\left(\mathbf{U}^+\right)<S_i<\lambda_i\left(\mathbf{U}^-\right)\Rightarrow \text{shock} \end{aligned} \tag{2.40}$$

where the + or – apices respectively indicate the region to the right and to the left of the wave and S_i denotes the speed of the shock. When the characteristic lines converge, they run into the shock path, when they diverge they bound the so-called *rarefaction fan*. These boundaries are called *head* and *tail* of the rarefaction. In eq. (2.40) one of the + or – regions is generally the star region so nature of the wave depends on the solution in this region. *Note that the origin of this nomenclature can be traced back to the compressible gas dynamic field, so a depression, i.e. a decrease of depth, in the SWE corresponds to a decrease of density in the gas.* Across a shock wave, which is a line in the x-y space, a jump of u_1 and u_2 occurs; no abrupt variation of u_3 occurs. The rarefaction wave is instead a wide region where a gradual variation of the u_1 and u_2 takes place, being only their x-derivatives discontinuous at the boundary of the rarefaction fan. The u_3 variable again varies continuously across this wave. The presence of the y momentum in (2.23) allows for the presence of a third wave, which is associated with the linearly degenerate eigenvalue λ_2 and is a shear or contact wave. It is located in the star region and all the quantities continuously vary across it, except for u_3. Being concentrated only on the x-split of eq. (2.23), the variable u_3 here behaves like a non reactive scalar contaminant.

It is worth stressing that, being the wave patterns straight lines, the solution at each point of the *x-t* plane can be found as a *similarity solution*, that is, depends only on the ratio *x/t* : in other words every wedge separated by two waves indentifies a region with constant solution $\mathbf{U}$.

As will be exhaustively explained in chapter 4, the Riemann problem is a building block for most numerical shock capturing numerical models.

2.3 Simplified SWE models

Although the SWE is one of the simplest mathematical model that can be derived from the NSE set, it still carries a large amount of complexity that reflects heavily on the numerical methods used to solve it. These difficulties are mainly connected to the shock development and propagation, transition between wet and dry regions, and the treatment of source terms. These topics will be covered in detail in the chapter 4.

Here a group of simplifications of the SWE will be introduced with particular attention paid to the so-called diffusive (or parabolic or noninertia) assumption. This approximation will be shown effective for the simulation of some real events in the next chapter.

For the sake of clarity the following analysis will be restricted to the 1D SWE, without loss of generality. These equations can be expressed in the form of the De-Saint Venant Equations,

$$\frac{\partial h}{\partial t}+\frac{\partial (hu)}{\partial x}=0 \tag{2.41}$$

$$I_l\underbrace{\frac{\partial u}{\partial t}}_{\text{local}}+I_c\underbrace{u\frac{\partial u}{\partial x}}_{\text{convective}}+I_p\underbrace{g\frac{\partial h}{\partial x}}_{\text{pressure}}=I_s g\left(\underbrace{S_0}_{\text{bed slope}}-\underbrace{S_f}_{\text{friction slope}}\right) \tag{2.42}$$

The various acceleration terms in the momentum equation are weighted by different indices *I*, used to define the different level of approximations:

0. *dynamic* wave: $I_l = I_c = I_p = I_s = 1$
1. *quasi-steady dynamic* wave (QSW) $\begin{cases} I_l = 0 \\ I_c = I_p = I_s = 1 \end{cases}$
2. *gravity* wave (GW) $\begin{cases} I_l = I_c = I_p = 1 \\ I_s = 0 \end{cases}$
3. *non-inertia* wave (NIW) $\begin{cases} I_l = I_c = 0 \\ I_p = I_s = 1 \end{cases}$
4. *kinematic* wave (KW) $\begin{cases} I_l = I_c = I_p = 0 \\ I_s = 1 \end{cases}$

All of these approximations make use of the same continuity equation (2.41).

In the following the non-inertia model will be also referred to as diffusive, dispersive or parabolic model. The nomenclature *diffusive* is commonly used in the hydrologic field to refer to the noninertia SWE. This can be easily explained (see section 3.1 for details) as its governing equation is similar to the diffusion of some quantity e.g. temperature diffusion (Fourier law), particles diffusion (Fick law). In general, a diffusion process is the time variation of a quantity due to the curvature of its spatial distribution.

Each of these models (1 → 4) applies a progressively higher level of simplification to the original equation set, and requires different boundary conditions, due to the fact that the corresponding mathematical model has a different eigenstructure.

The use of the NIW for unsteady flow routing has been increasing in recent years because it is the simplest among the approximations that can account for the downstream backwater effect and yields reasonably good results. Moreover, as demonstrated by Tsai (2003), the NIW model performs much better than the QSW, which is mathematically more adherent to the complete system: this is due to the fact that the local and convective acceleration balance each other in most of the real world flows: neglecting only one of the two inertial terms leads to a less accurate model. In addition, the level of complexity of the solution strategies required by the quasi steady dynamic model is much higher than the diffusive model.

The theoretical assessment of the applicability of simplified versions of the SWE has been a central topic for decades, and the first attempts can be traced back to the seventies. One of the widely recognized inequality criteria was proposed by Ponce et al. (1978). The authors used a linear stability method to investigate the response of the diffusion and kinematic wave models to a periodic perturbation of a steady uniform state. They analytically compared the celerity and the attenuation characteristics (one possible formulation of the attenuation factor is $\delta = \ln\left(a_1/a_0\right)$ where a_1 and a_0 are the wave amplitudes at the beginning and at the end of a wave period) of each model with the corresponding quantities of the full dynamic model: they postulated a criterion of the NIW model to approximate the dynamic wave model within a 95% accuracy for celerity as

$$TS_0\left(g/y_0\right)^{1/2} \geq 30 \qquad (2.43)$$

where T is the wave period of the sinusoidal perturbation to the steady uniform flow (usually twice the time of rise of the flood wave); S_0 is the channel bed slope; y_0 the uniform flow depth. The assumptions of that work were the prismatic channel and the absence of backwater effects. The latter was relaxed by Tsai (2003) who investigated the dependence of the threshold value in (2.43) on the downstream condition. Other criteria have been proposed, based on different approaches. Fread (1985) proposed his criterion based on comparisons of integrated results such as a hydrograph at the outlet of a channel:

$$T_r S_0^{1.6} \Big/ \left(q_p^{0.2} n^{1.2}\right) \geq 51 \qquad (2.44)$$

where for q_p is the peak of the inflow hydrograph (unit discharge), T_r the time to peak in inflow discharge, n Manning coefficient.

Ponce criterion has found its place in standard textbooks (French, 1986; Ponce, 1989; Chaudhry, 1993; Viessman and Lewis, 1996; Singh, 1996), and its effectiveness was recently assessed by Perumal and Sahoo (2007). The authors found that (2.43) consistently predicted narrower ranges of applicability of the NIW, thus its application is questionable, as other studies had previously stated (Zoppou and O'Neill, 1982; Ferrick and Goodman, 1998; Crago and Richards, 2000). The inaccuracies of the criteria are mainly connected to the linear stability analysis used to obtain them, as well as the various simplifications adopted (mainly the broad channel assumption). Perumal and Sahoo (2007), investigated the influence of the scaled water profile gradient, namely $\left(dy/dx\right)/S_0$, where y is the WSE and x is the station. This quantity was originally proposed by Henderson (1966), and used for the classification of flood waves as kinematic or diffusive. Price (1985) used it as a criterion for these approximations to be correctly applied, but gave a far too restrictive threshold of 0.05. Perumal and Sahoo (2007) stated that the upper limit of the scaled gradient should be around 0.11 for the Muskingum-Cunge method to be consistently applied.

All these criteria are summarised in Figure 2.2, where the applicability of the different wave approximations is shown dependent on the four quantities appearing in the criteria proposed above. It is clear that the condition at which no approximation of the dynamic wave should be applied is represented by a supercritical propagation of an impulsive wave over a flat, rough bed.

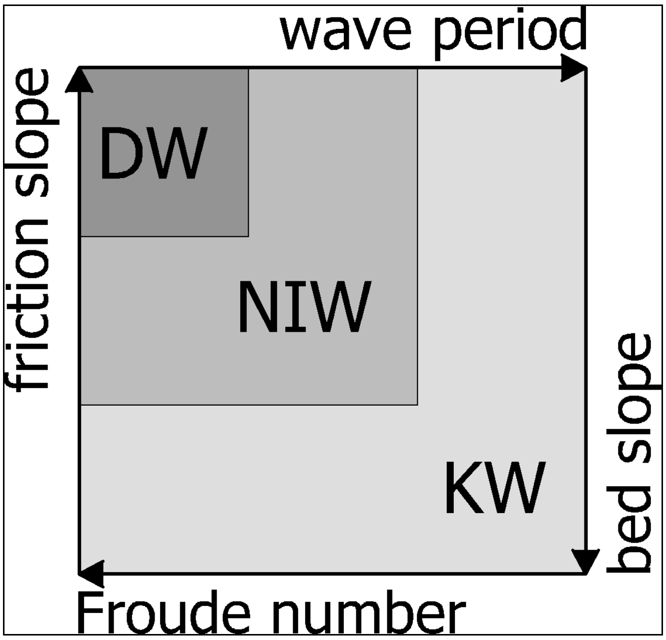

Figure 2.2 – Dependence of the applicability of simplified SWE models upon different quantities.

Given the numerous exceptions to the criteria developed, together with the major assumptions in their derivations, a more rigorous verification is needed. The next chapter will deal with the comparison of a highly inertial experimental flood with numerical results from a NI model.

3. Verification of applicability of the diffusive model

In this chapter a numerical model based on the parabolic approximation of the 2D Shallow Water Equations (SWE) is presented.

It is then tested against data from a physical model of a dam break event. The choice of a real dambreak event as a comparison term for a parabolic model is due to the assumption that, given its strong inertial characterization, it would be able to highlight the limits of the diffusive approximation. The main aim is to point out at which extent this approximation is suitable for simulating such an extreme events.

3.1 Conceptual model

Diffusive approximation of (2.23) consists of neglecting local and convective accelerations in (2.24) and (2.25) leading to:

$$\underline{\mathbf{E}}_{diff} = \begin{pmatrix} hu & hv \\ gh^2/2 & 0 \\ 0 & gh^2/2 \end{pmatrix} \qquad \mathbf{U}_{diff} = \begin{pmatrix} h \\ 0 \\ 0 \end{pmatrix} \tag{3.1}$$

which can be further expanded as follows:

$$\frac{\partial h}{\partial t} + \frac{\partial (uh)}{\partial x} + \frac{\partial (vh)}{\partial y} = q \tag{3.2}$$

$$\frac{\partial H}{\partial x} + \frac{u\sqrt{u^2+v^2}}{\chi^2 h} = 0 \tag{3.3}$$

$$\frac{\partial H}{\partial y} + \frac{v\sqrt{u^2+v^2}}{\chi^2 h} = 0 \tag{3.4}$$

where $H \equiv h + z$.

The main benefit of the diffusive approximation is that, as previously stated by Hromadka and Lai (1985), the original system of equations (2.23), in the unknown *h*, *u*, *v*, can be now simplified to obtain two explicit formulations $u = u(h)$ $v = v(h)$ coupling (3.3) and (3.4):

$$u(h) = \frac{\chi \cdot h^{1/2}}{S_{ws}^{1/2}} \nabla H \cdot \hat{e}_x \tag{3.5}$$

$$v(h) = \frac{\chi \cdot h^{1/2}}{S_{ws}^{1/2}} \nabla H \cdot \hat{e}_y \tag{3.6}$$

where $\left\{\hat{e}_x, \hat{e}_y\right\}$ is the frame reference measuring the horizontal 2D space and the quantity S_{WS} describes the local slope of water surface:

$$S_{ws} \equiv \left|\nabla H\right| \equiv \left[\left(\frac{\partial H}{\partial x}\right)^2 + \left(\frac{\partial H}{\partial y}\right)^2\right]^{1/2} \tag{3.7}$$

and results:

$$S_{ws} = \frac{-\left|\mathbf{V}\right|^2}{\chi^2 h} \tag{3.8}$$

where:
V = (u,v).
(3.5) and (3.6) can be then directly substituted into (3.2) leading to:

$$\frac{\partial h}{\partial t} + \frac{\partial}{\partial x}\left[k \nabla H \cdot \hat{e}_x\right] + \frac{\partial}{\partial y}\left[k \nabla H \cdot \hat{e}_y\right] = q \tag{3.9}$$

which is a single parabolic PDE in the only unknown *h(x,y,t)*, where *k* is the isotropic but variable in both time and space because solution-dependent, diffusion coefficient:

$$k = \frac{\chi^2 \cdot h^{2/3}}{S_{ws}^{1/2}} \tag{3.10}$$

It is worth noting the analogy between equation (3.9) and Richards equation for flow in porous medium with trasmissivity *k*. Equation (3.8) implies that the model, given any topography, finds the distribution of velocities and depth that minimizes the difference between surface and friction slope.

The parabolic approximation, neglecting inertial terms, leads to a shock-free evolution, allowing the use of much simpler numerical treatments. Moreover, boundary conditions can be thus assigned in form of an imposed arbitrary depth (Dirichlet type), an imposed arbitrary source of mass (Neumann type), or a solution-dependent condition of the type q=q(h) or equivalently h=h(q) without a-priori awareness of super or sub-critical flow state needed.

As stated in many previous works (Akanbi and Katopodes,, 1988; Brufau et al. 2002; Liao et al. 2007), the critical aspect of the SWE resides in the analytical representation and numerical discretization of the friction term connected with the simulation of the advancing and receding fronts of the flood: the main problem arising when using a Chezy-type friction term is that it would grow significantly when very small depth are encountered (Horritt, 2002) as in drying and wetting areas, thus requiring the presence of a high surface slope. This fact can have a major impact on the drying phase as the depth gradient is usually opposite to bed slope so that not always negligible volumes of water remain entrapped in the thin film of water typical of SWE simulations. This is the main issue of the full dynamic model that remains qualitatively unchanged in the diffusive model.

3.2 Numerical model

The numerical scheme used here is developed from the storage cell method originally proposed by Zanobetti et al. (1970), Cunge et al. (1976) and successively used in Estrela (1994) and Romanowicz et al. (1996), Bates and De Roo (2000): in these works cells are constructed onto an equally spaced grid derived from DEM topography. Intercell fluxes are determined by means of uniform flow formulae such as Manning and weir-type equations. Successive applications, while still dealing with rectangular grids, applied a finite difference technique to determine the fluxes based on the diffusive bidimensional scheme (Prestininzi and Fiori, 2006; Horritt and Bates, 2001). This approach has been analysed by Bates and De Roo (2000), who found that in real case applications the diffusion wave treatment employed with the storage cell method out-performed two-dimensional full dynamic finite element schemes because the simplified treatment of flow routing on the floodplain allowed a much higher density representation of floodplain topography. The simplified process representation also offers the possibility of model upscaling to much larger spatial scales, as computational limitations are reduced (Horritt and Bates, 2001).

The storage cell scheme based on structured grid, is here applied to a non-structured mesh. The method utilizes cell-centred depth values to determine fluxes at interfaces. Depth field is piecewise constant over the domain; linear variation of surface height is used in discretization of diffusive terms.

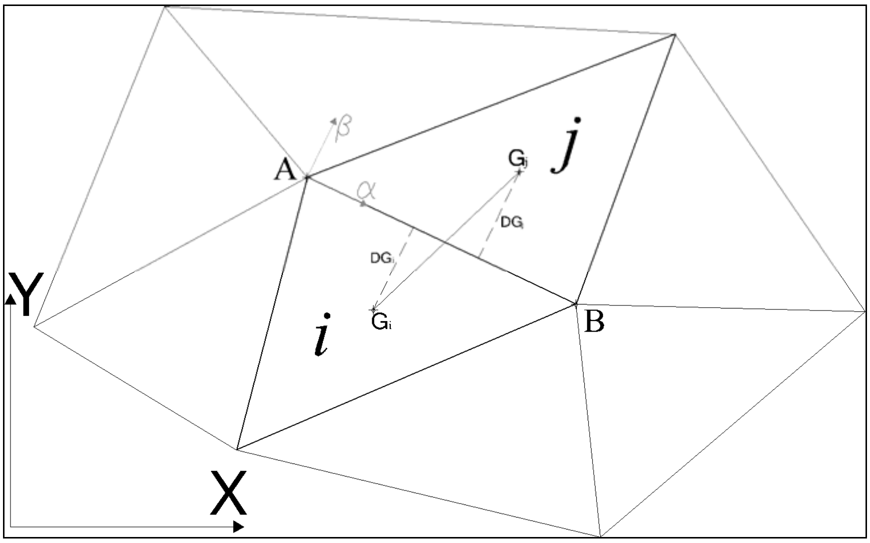

Figure 3.1 – Local frame reference used to determine intercell flux: $\{X, Y\}$ is the global frame reference, $\{\alpha, \beta\}$ is the local frame with respect to the interface ($\overline{\mathrm{AB}}$) between elements i and j, G_i and G_j are cells' barycentres, DG_i and DG_j their distance from the edge, drawn in dashed lines.

Given the intercell flux is only determined by β component of velocity (make reference to Figure 3.1 for notation meaning), it can be computed from equation (3.5) expressed in local coordinates, thus splitting the original vectorial problem into three scalar ones:

$$w = \mathbf{V} \cdot \hat{e}_\beta = \frac{\chi \cdot h^{1/2}}{S_{ws}^{1/2}} \nabla H \cdot \hat{e}_\beta \tag{3.11}$$

where derivatives can be approximated by discrete formulations:

$$\nabla H \cdot \hat{e}_\beta = \frac{\partial H}{\partial \beta} \cong \frac{H_j - H_i}{DG_{i,j}} \tag{3.12}$$

$$\nabla H \cdot \hat{e}_\alpha = \frac{\partial H}{\partial \alpha} \cong \frac{Hnod_{A_{i,j}} - Hnod_{B_{i,j}}}{L_{i,j}} \tag{3.13}$$

with:
$L_{i,j}$ length of the edge AB
$DG_{i,j} = DG_i + DG_j$

$$Hnod_k = z_k + \frac{1}{N_k} \sum_{\Omega_k} h_l \qquad k = A_{i,j}, B_{i,j} \tag{3.14}$$

where:
z is the node bed elevation, Ω_k is the group of elements that share the node k, N_k is their number and h_l their depth.
It follows that the stencil area used to determine water surface gradient is different for longitudinal and transverse slope, as depicted in Figure 3.2. It is worth noting that the stencil area is determined a-priori, depending only on the mesh geometry, and not influenced by flow dynamic, as, for example in upwind schemes.

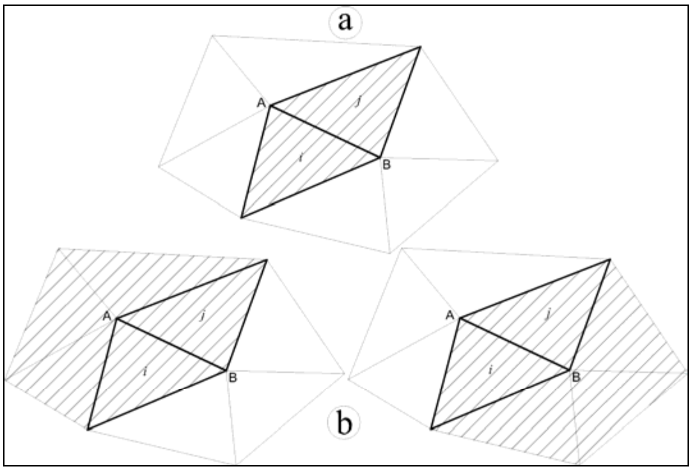

Figure 3.2 – Stencil areas for approximation of a) longitudinal, and b) transverse water surface slope.

The mesh used to describe topography is made of sloping faces, so that the numerical scheme must deal with partially wet elements. To overcome this problem, cell bottom is considered horizontal and its elevation equal to the elevation of the centre of mass of the face: this assumption not only helps significantly in managing wet-dry-wet transitions, but also lets the volume of water stored in a cell be the volume of the triangular prism whose height is the local depth.

This simplification, however, obliges to adopt a special treatment for the bed friction term. The source of the problem resides in the assumption, adopted by almost all 2D shallow water modellers, that the hydraulic radius contained in the friction term, can be approximated by water depth. The origin of this postulation is due to the broad channel 1D approximation that substitutes the wetted perimeter with the free surface width. When transferred to bidimensional modelling, and not carefully used, this assumption automatically neglects wall friction (Molls et al., 1998). Moreover, when the cell bottom is assumed horizontal, in presence of high bed slope, the broad channel assumption leads to another source of error, as depicted in Figure 3.3: the free surface width within the single element is not comparable to the bottom width so that:

$$\Re_i = \frac{A_i}{P_i} = \frac{b_i h_i}{B_i} = h_i \cos(\alpha_i) \qquad (3.15)$$

where $\cos(\alpha_i)$ can be seen as a correction of the hydraulic radius $\Re_i$, or, if Strickler equation is used, a correction of the friction coefficient:

$$\chi = \kappa_{str} \Re^{1/6} \cong \chi_{BC} \cos(\alpha)^{1/6} \qquad (3.16)$$

where

κ_{str} is Strickler nondimensional coefficient, χ_{BC} is the Chezy friction coefficient in the Broad Channel approximation which is then corrected by the term $\cos(\alpha)^{1/6}$.

The fluxes computed for three edges of the cell are then used to update the volume stored in the element. An explicit time-marching approach is used to predict the volume, and consequently the depth in each cell:

$$h_i^{t+\Delta t} = h_i^t + \frac{\Delta t}{\mathrm{A}_i}\left(\tilde{Q}_t + \sum_{\Psi} Q_i\right) \qquad (3.17)$$

where:

Q_i is the volume discharge between cell *i* and each cell of the group Ψ containing the adjacent ones, A_i is the planar area of cell *i*; Δt is the time step, $\tilde{Q}_t$ is an external discharge source

A weighted average of $h_i^{t+\Delta t}$ and h_i^t is then used to determine new fluxes and a final depth field.

This predictor-corrector scheme, while slightly enhancing numerical stability, has been chosen to correctly manage wetting and drying phases, as will be described exhaustively in the next section.

Given equations (3.11),(3.12) and (3.13) discharge between cell *i* and *j* can be computed:

$$Q_{i,j} = w L_{i,j} h_{flow} \qquad (3.18)$$

flow depth h_{flow} has been defined by Bradbrook et al. (2004) as the difference between the highest water free surface in the two cells and the highest bed elevation. This formulation seems more adherent to the way of computing discharge by means of weir formula. A simpler solution, the arithmetic average of the two depths, has been empirically found to improve numerical stability, while, at the same time, producing comparable results:

$$h_{flow} = \left(h_i + h_j \right) / 2 \qquad (3.19)$$

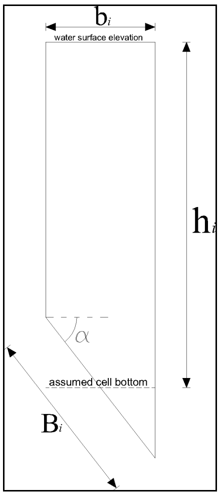

Figure 3.3 – Schematization used for friction term correction

Some numerical difficulties still remain despite the simplification in both mathematical approach and numerical treatment. Next section explains how wet-dry-wet transitions are dealt with.

3.2.1 Wetting and drying

The wetting and drying procedure takes advantage of the two-step temporal integration described in the previous section: during the first phase (prediction) the new depth field is determined by means of internal end external discharges calculated using the depth field from the preceding time step. The position of the advancing and receding fronts predicted in this phase is frozen and passed to the second phase (correction). The second phase determines the final location of fronts, with two main constraints:

1) the front cannot advance more than 1 cell at time (outlet velocity of an element wetted in the first phase is set to zero)
2) a receding front from the prediction phase cannot become an advancing front (inlet velocity of an element dried in the first phase is set to zero).

The second phase, however, is iterated until fronts come to rest: the only difference between one iteration and the (possible) next one, is the imposition of the previous two constraints over still moving fronts. This algorithm has proven to work well, both for idealized case, and for real events on complex topography. In order to fulfil mass balance, every time a cell dries up (negative depth appears), both during the prediction and the correction phase, the volume stored in it at the beginning of time step is distributed to the surrounding elements, proportionally to the fluxes previously estimated by means of (3.18). Its edges are thus considered receding fronts and rule number 2) is then applied. Expansion and contraction of the wet portion of the model domain thus proceeds at a maximum rate of one cell per time step.

3.3 Toce river test case

The physical model of a river located in Occidental Alps (Italy) was built up at ENEL HYDRO laboratories (Milan, Italy) under the EU funded project CADAM (Concerted Action on Dam Break Modelling). Refer to TESTA (2000) for details. The model consisted of a 1:100 scaled replication of almost 5km of the river near to Pié di Lago, resulting in a 55x13 m installation. A shaded reconstruction of the model is shown in Figure 3.4: it is made of concrete and covers almost the entire width of the valley including the tiny and almost invisible thalweg. The numerical modellers participating in the project were given a detailed description of the topography by means of a dense (5x5 cm, 140 000 points) uniform grid. The model included several groups of buildings, whose height is given separately as the decision whether to include them or not in numerical modelling was up to the participants. Two bridges, a barrage and a big reservoir are also present. Their modelling was optional in the project. A set of 33 water probes scattered over the entire model were used to record time evolution of water depth. Recordings are available for only some of them, whose locations are shown in Figure 3.4.

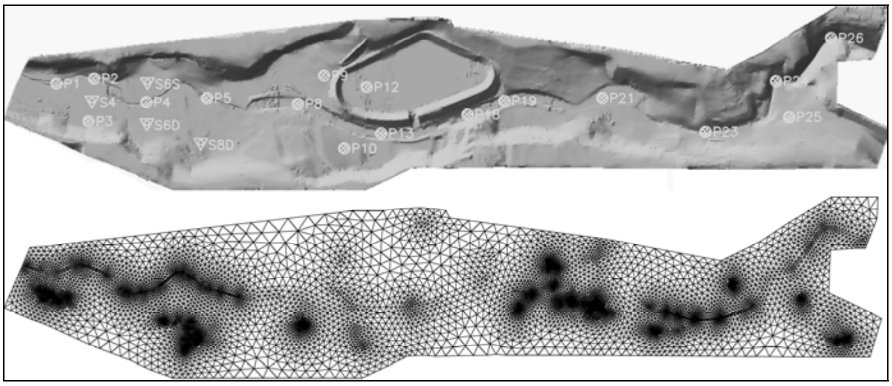

Figure 3.4 – Toce river shaded view (upper panel), with location of available gauges, mesh used for numerical simulation, approximately 16 500 elements (lower panel).

The valley is very steep, with a mean slope of 2%, while some parts present abrupt drops, as depicted in Figure 3.5 which shows the elevation profile of the thalweg.

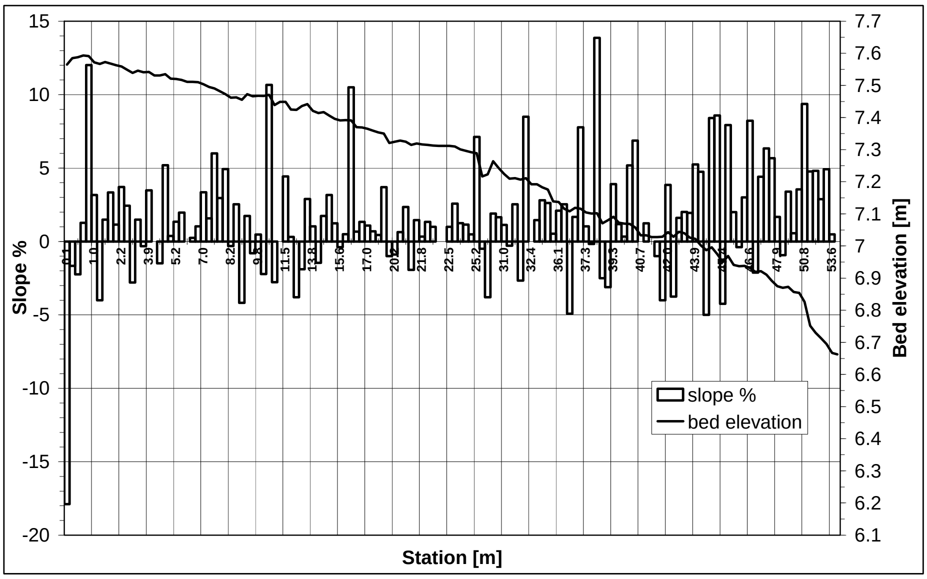

Figure 3.5 – Bed elevation and local slope along thalweg: average slope of the entire valley is 1.68 %

The big reservoir is located in the central part of the valley, occupying almost the whole section. It is delimited by levees, with an opening at the river side, always kept closed during experiments.

The upstream boundary is connected with a tank whose level is regulated with a pump. When the level rises above the bottom of the first section of the model, water flows into the valley, while discharge can be measured through monitoring of outflow of the electronically controlled pump. The downstream end of the physical domain is modelled as a free fall into a tank. Critical flow occurs at the outlet, so that its influence on the upper part should be minimal.

Two extreme flood events have been replicated: the first simulating a dambreak whose inundation was able to overtop reservoir levees, while the other one left the reservoir empty. The model is completely dry at the beginning of each simulation.

Several pictures of the inundation are available in Soares Frazão and Testa: they depict how the flow easily submerges buildings and overtops bridges, producing very high vertical flow jets, which demonstrate the intensity of the events.

Stage and discharge hydrographs for the second scenario are depicted in Figure 3.6.

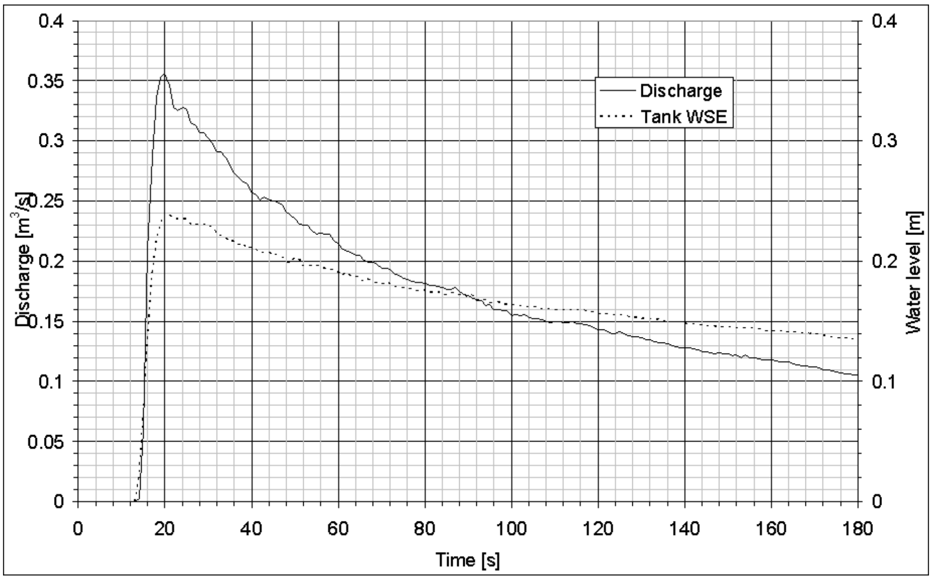

Figure 3.6 – Inlet hydrographs for second scenario: the solid line is the discharge from pump record and the dashed line is the water surface elevation in the inflow tank.

3.3.1 Numerical experiments

Some modellers directly used the topography provided by the project organization team to build the mesh or grid needed to develop numerical simulation, thus resulting in a huge number of structured elements (2·106) (Liang et al., 2007; Ying et al., 2004). Others (Caleffi et al., 2003) decided to hold one point every two or four, and then connect them to obtain two regular meshes for a grid refinement analysis. All the models discussed here used FV schemes.

The mesh used for this numerical simulation is a non structured, non uniform triangular mesh, whose nodes' elevation were draped to the surface obtained by quadratic interpolation of the provided DEM. Mesh size ranges from 0.03 m to 1 m (side length) according to topographical features, and to the presence of buildings: some constraints on elements shape were imposed to the mesh generator in order to obtain gradual transitions. Buildings are modelled by raising local topography to the roof level: this is to allow overtopping of some of them. Time step size was set to 10-4s. Both scenarios have been simulated: accuracy of prediction is identical for both situations. Only the highest hydrograph is reported here, for brevity. Imposition of discharge or level type upstream boundary conditions was found to give matching results, probably because of the high slope of the valley. Serious doubt are still present on the upstream flow condition: Caleffi et al. (2003) highlight that imposing a subcritical or critical condition produces results not matching experimental data, while imposing supercritical conditions results in a better behaviour. Further details in form of a discharge per unit width are needed to impose a more accurate condition. The present model overcomes this kind of problems because, as stated in the description of the parabolic approximation, no distinction between super and subcritical flow condition exists. No boundary condition needs to be applied at lateral border, because flow never reaches it. Zero depth is imposed at downstream section. The initial condition is of dry bed on the whole domain. The duration of the simulation is 180 s for the second scenario. Strickler coefficient was set to 61.728 $m^{1/3}/s$ as recommended by the ENEL. No velocity measurements are available, and the absence of scale effects on viscous forces can be assessed only analysing predicted numerical velocities: Reynolds number arising from this investigation is about 10^5; Friction index can be evaluated as $\lambda = 8gn^2 / h^{1/3}$ whose value is about 0.04; the corresponding metric roughness is 1.8 mm, compatible with smoothed concrete: the related turbulent state is on the frontier between transition zone and fully turbulent flow state, where viscous and friction forces start losing their dependence on Reynolds number.

3.3.2 Results and discussion

Comparison between experimental and numerical data is given in Figure 3.7, in terms of water surface elevation, for the present model and three other full dynamic models for which published results are currently available (Caleffi et al., 2003; Liang et al., 2007; Ying et al., 2004).

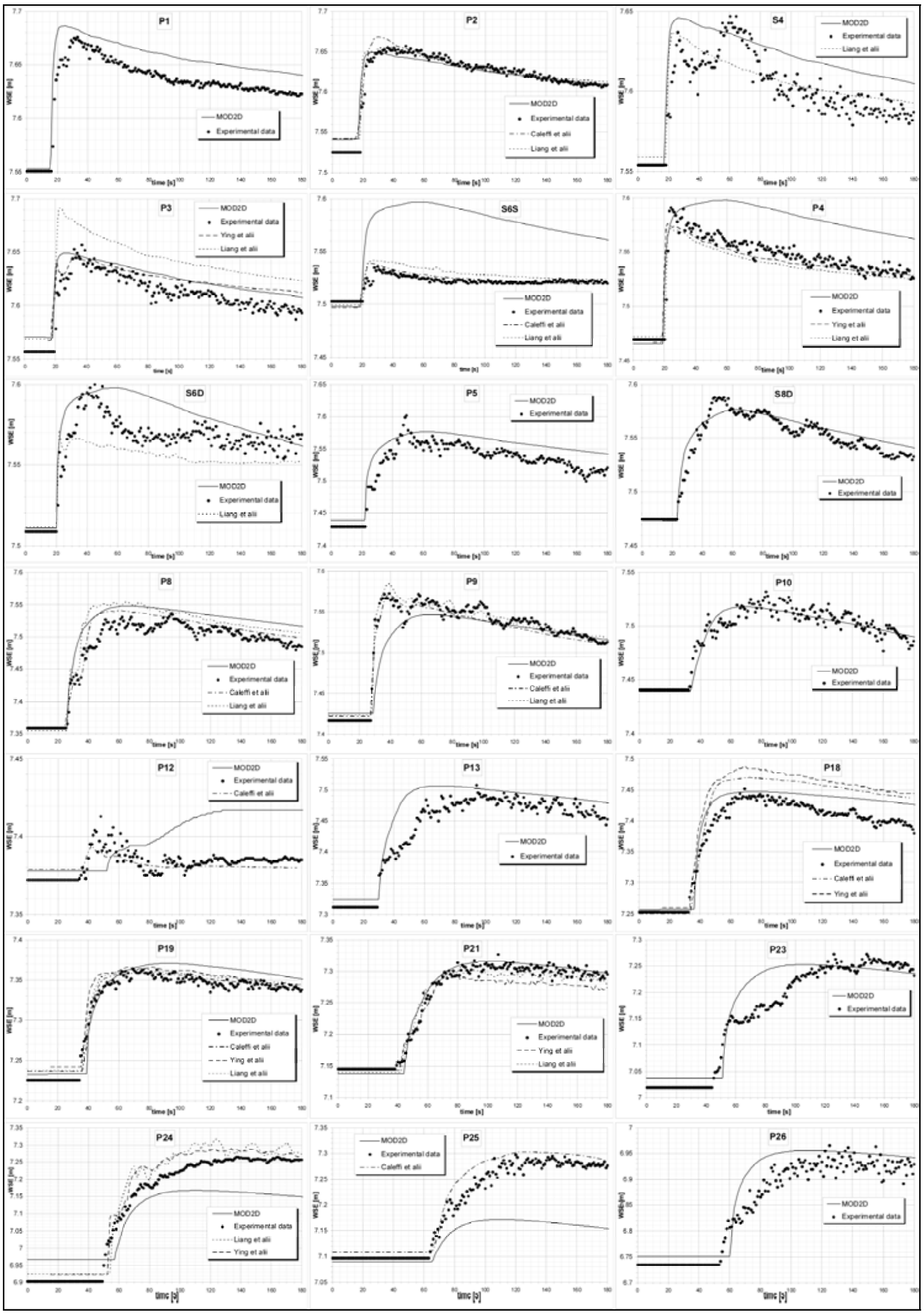

Figure 3.7 – Comparison between experimental data and result of a group of numerical models: numerical data of some models are not available for all gauges. Present model results are referred to as “MOD2D”

Arrival times of the front were another factor analysed in the project: Figure 3.8 shows discrepancies between numerical and experimental data in terms of delay or advance.
The numerical front is considered to arrive when the depth is greater than 10^{-4} mm, 10 times greater than gauges precision.

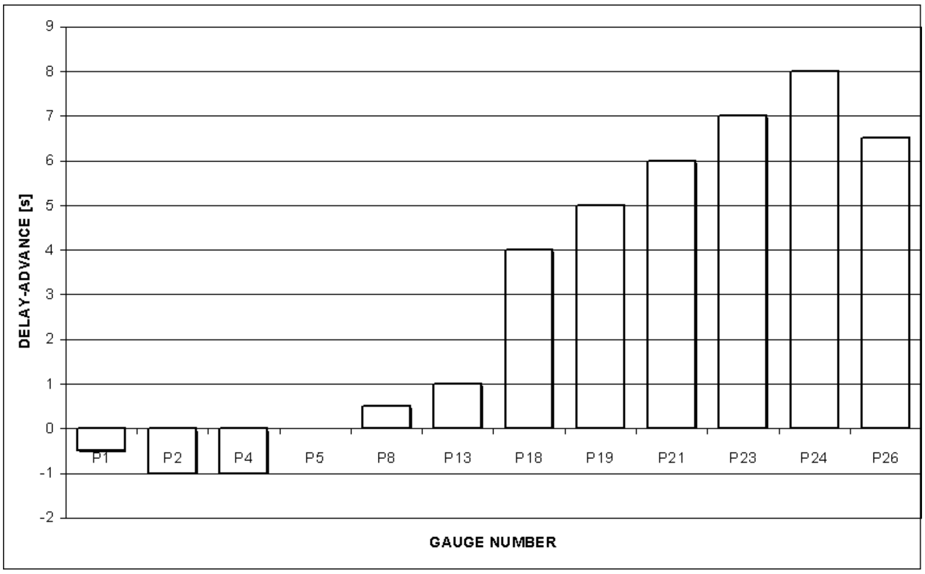

Figure 3.8 – Advance or delay of front predicted by numerical model with respect to experimental data: only thalweg gauges are considered.

Propagation of inundation is depicted in Figure 3.9, while some pictures of predicted velocity field are shown in Figure 3.10.

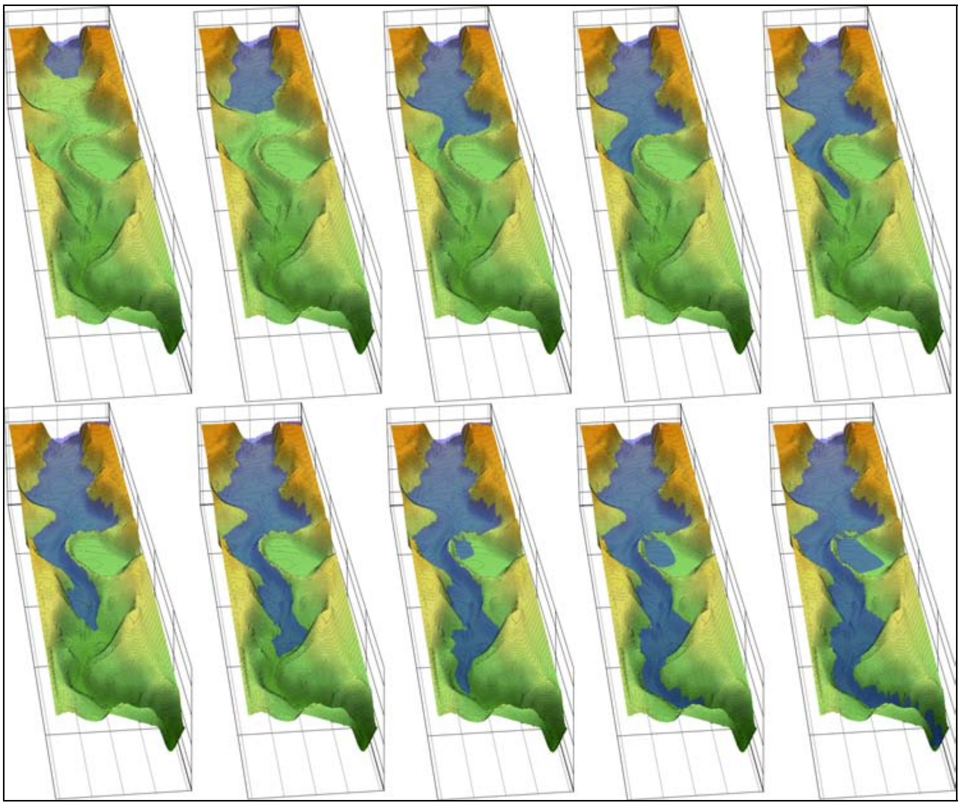

Figure 3.9 – 3D view of propagation of inundation through the valley; pictures are ordered left to right, up to bottom, and are taken at the following instants 19 – 24 – 29 – 34 – 39 – 44 – 49 – 54 – 59 – 64 s. Vertical distances are 4 times grater then horizontal ones. On very steep walls, some graphical artefacts are visible.

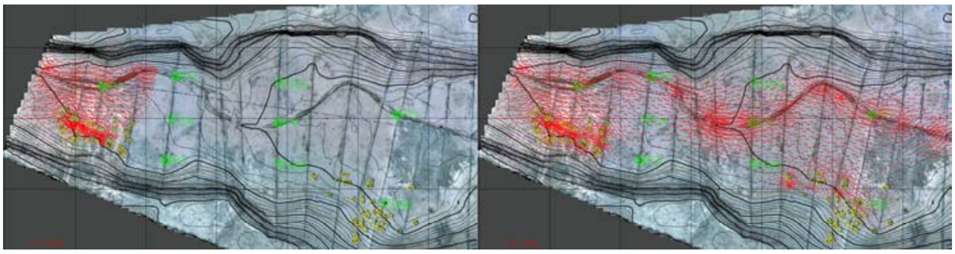

Figure 3.10 - Velocity field for two frames of figure 7 (19 and 29 s): it is worth noting how the inundation does not follow the thalweg at all, and maintains a 1D dynamic with the exception of local flow between buildings. Vectors' scale in the lower left corner. Yellow boxes are modelled buildings.

The event simulated clearly shows the same features as a dam break occurrence: the inflow hydrograph has a vertical raising phase followed by a slow falling limb. The resulting dynamic is of a sharp front, which moves forward through the dry valley with high propagation speed, not following the thalweg, and behaving essentially as a one-dimensional wave in many parts of the domain. Only after passing the reservoir section, the flood develops two-dimensional features as it leaves the channel and spreads through floodplains. Flood shows an abrupt acceleration in the downstream part of the domain, due to the raise of the bottom slope and the rapid reduction of flow area. As a result of changes in the valley slope and shape, the flow continuously passes through critical condition. These features can be simulated accurately only if the conceptual model is based on the full form of SWE, and if the numerical solver is capable of dealing with sharp interfaces. The criteria discussed in section 2.3, which define the applicability of a diffusive wave model to a specific event, are here recalled. The criterion proposed by Ponce (1978), eq. (2.43), if applied to the Toce river physical model, returns a value of 4, about 7 times smaller than the threshold (30) proposed by the author. The criterion proposed by Fread (1985), eq. (2.44), yields a value of 2.2, about 23 times greater than the threshold 51. The more recently proposed criterion by Perumal and Sahoo (2007), based on the comparison between surface and bed slopes $\left(dy/dx\right)/S_0 < 0.11$, is more difficult to employ, as the experimental surface gradient is highly variable in both space (in this case even in 2 dimensions) and time. An attempt has been made, analysing the front advancement for the upper part of the Toce river model, including only gauges S2, P1, S4, P4, P5, P8, P13, P18, P19. The front is shown in Figure 3.11 together with the corresponding time variation of the Perumal and Sahoo (2007) criterion. Even this analysis shows that the case simulated is far from being in the range of applicability of a non-inertia model. Moreover, even if the value of the WS scaled gradient decreases in time, it asymptotically converges to a value about 10 times greater than the limit value of 0.11, indicating that the flow motion continues to be dominated by inertial effects.

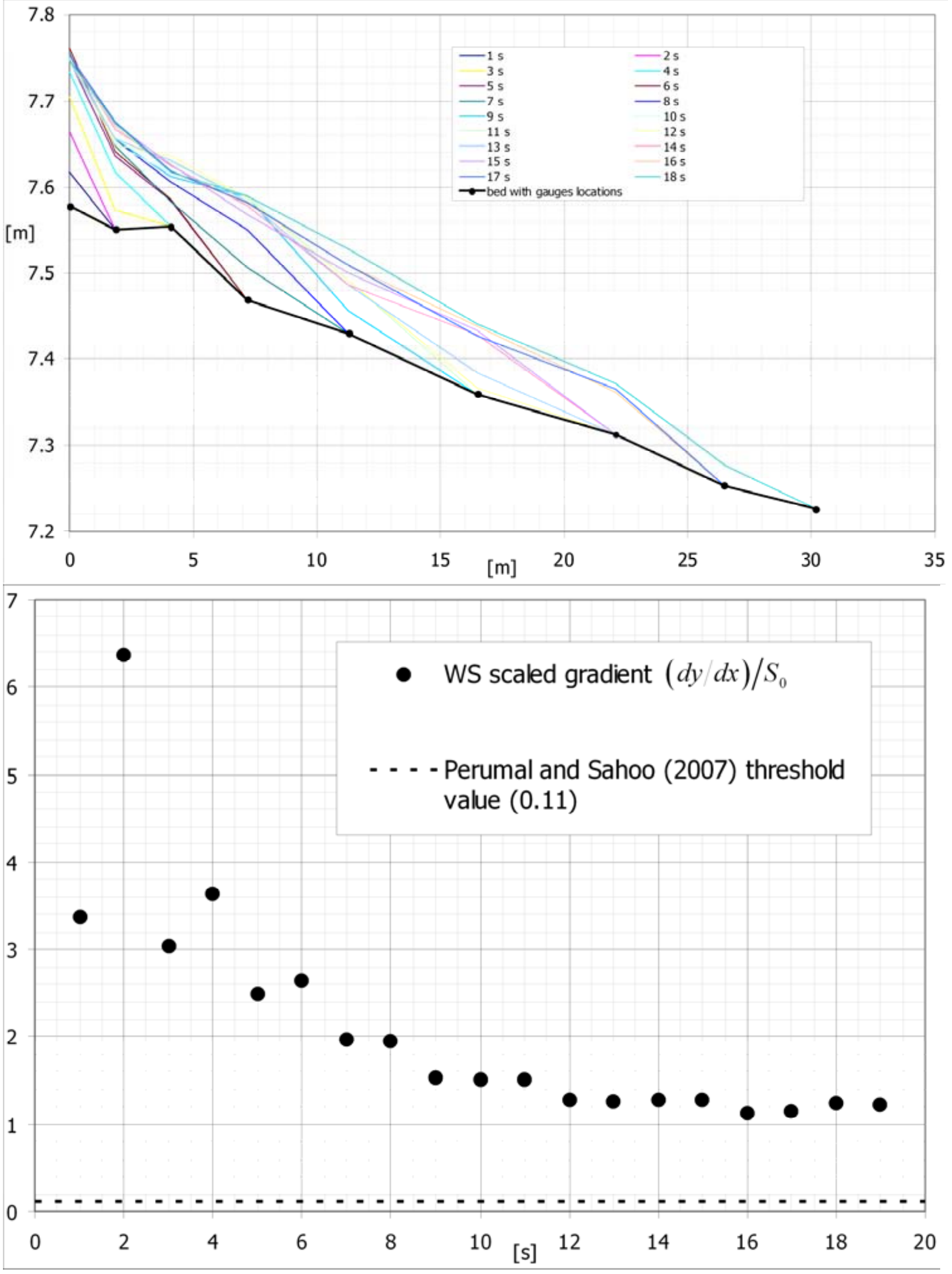

Figure 3.11 – Upper panel: longitudinal view of the experimental front advancing over the upstream part of the physical model; lower panel: comparison between the experimental WS scaled gradient and the threshold value proposed by Perumal and Sahoo (2007) defining the range of applicability of a parabolic wave model.

However, such phenomena do not preclude the application of a much simpler model, from both conceptual and numerical point of view. A diffusive model, such as the one described in this study, appears to be a wise balance between computational charge and robustness on the one hand, and results' quality on the other. Comparison with experimental data demonstrates that the overall dynamic of the event is well simulated. The robustness of the model is exhibited by both the absence of spurious oscillation in any part of the simulation and the matching results of the application of a discharge-type or level-type upstream boundary condition. Furthermore, the model's predictions are not the outcome of a calibration procedure, since the only parameter to be calibrated in the model is the friction term, whose value was provided by ENEL-HYDRO.

Detailed analysis of results has been undertaken, in order to establish the limits of application of the parabolic model. For this reason, all the observations at all the available gauges are reported. A quantitative analysis has been conducted (Table 1), examining the values of RMSE calculated comparing predicted and measured depth series. The following examination consists of an inspection of results from the upstream section toward downstream.

At gauge P1, the model predicts a higher level than the experimental data, while no quantitative results are available from other numerical models. This overestimation does not seem to influence the flow immediately downstream, as the model correctly predicts at gauge P2. Conversely, the huge, low frequency oscillation of water surface at gauge S4 in the first half of simulation period is not reproduced neither by this diffusive model nor by Liang full dynamic model: both smooth out results, but while the diffusive model is capable of predicting the peak level almost exactly (though advanced in time), the falling limb is locally simulated better by Liang model. High frequency oscillations, present in this last part of the recorded hydrograph, are obviously not reproduced by any of them. The overall performance in terms of RMSE is similar. Gauge P3 measurements show that the main peak of the hydrograph is preceded by a smaller one. Both diffusive and Ying model, the latter being also able to reproduce first peak, behave well here, producing a similar RMSE. Liang model and diffusive model actually smooth out the first peak, but Liang model overestimates both the main peak magnitude and the falling limb, leading to a much higher RMSE: this is due to the fact that their simulation does not include buildings that are just upstream of the gauge and act as a barrier.

Gauge S6S requires an in depth analysis as it is not apparently clear why the diffusive model completely fails to represent the whole hydrograph both qualitatively and quantitatively. What happens here is that S6S gauge is in a shadowed location: in other words the relief located just upstream of the gauge deflects the flow toward the centre of the valley, screening the gauge from the main flood wave. In fact, among the three gauges lying approximately on the same section of the valley (S6S, P4, and S6D), S6S shows the lowest peak level, 7.54m, compared with 7.59m of P4 and 7.6m of S6D. Since the front of inundation here travels parallel to the cross section of the valley, the marked difference in measured levels, at the same instant, reveals the deflection effect. Moreover, the surface level at S6S does not have a falling limb, its tail showing a slightly raising trend. This means that a relatively calm, steady recirculation occurs, also proved by the absence of high frequency oscillations, followed by an alignment with P4 level at 7.525 m. A diffusive model neglects this purely inertial effect, predicting exactly the same WSE for those three gauges.

Peak level at gauge P4 is well predicted by both the diffusive model and other numerical models, which however overestimate the rest of the hydrograph. Level at gauge S6D is fairly well simulated. Peak flow is well predicted though delayed. Liang model does not simulate well because the gauge is just in front of a group of buildings, which are not included in their simulation. RMSE of diffusive model quickly lowers moving away from the screen mentioned above (from S6S to P4 to S6D). Gauge P5 and S8D are both well simulated by diffusive model. While peak level at gauge P8 is slightly overestimated by all models, the overall trend is well predicted.

Predictions of diffusive model at gauges P9 and P12 are tightly connected, as P9 is located in front of the portion of the levee of the reservoir where overtopping occurred in both the physical model and the full dynamic numerical models. The parabolic model, even if it does not underestimate water level at P9 much, it does not accurately predict levee overtopping: in fact, the overtopping occurs 1.5 m closer to the reservoir intake, where the crest of the levee is lower. The real overtopping is in this case due to a run-up caused by a conversion of kinetic into potential energy, since water level at P9 is lower than the top of the levee: in the parabolic model this transfer does not take place. As stated before, overtopping does happen in the simulation, but the volumes of water thus entering the reservoir are consequently wrong, leading to filling the reservoir and overestimating P12 levels. The delay of the hydrograph is due to the different modality and to different location of the overtopping.

Level measurement at gauge P10, P13, P18, P19 and P21 are well predicted by all models and for P18 and P21 the parabolic model gives better results than full dynamic models. Trend recorded by gauge P23 shows a step behaviour which could be caused by transition through critical state or by the overtopping of barrier located in the main channel upstream of the gauge, which causes a high RMSE for the diffusive model, although the final level after the step is well predicted.

Behaviour of the parabolic model at gauges P24 and P25 requires an extensive analysis: the high underestimation of water level at these locations is due to two successive changes in flow area. In fact, just upstream of gauge P25, the thalweg has a marked corner, so that part of the flow, due to its inertia, leaves the thalweg towards P25. The flow in the main channel thus slows down, raises its stage before accelerating again when the diverted flow returns into the channel, upstream of gauge P26. The parabolic model maintains a higher discharge in the main channel, thus predicting lower levels, both at gauge P24 and P25. A good agreement with measured data at gauge P26 confirms the above interpretation of the local phenomenon.

Table 3.1- RMSE [m] based on depth comparison

	MOD2D	Caleffi et alii	Liang et alii	Ying et alii
P1	0.265			
P2	0.125	0.101	0.104	
S4	0.277		0.163	
P3	0.189		0.413	0.179
S6S	0.752	0.053	0.098	
P4	0.444		0.135	0.139
S6D	0.207		0.206	
P5	0.302			
S8D	0.116			
P8	0.363	0.206	0.331	
P9	0.271	0.115	0.111	
P10	0.104			
P12	0.311	0.070		
P13	0.403			
P18	0.312	0.464		0.595
P19	0.201	0.083	0.105	0.137
P21	0.129		0.138	0.235
P23	0.432			
P24	0.914		0.513	0.423
P25	1.076	0.279		
P26	0.443			

General features in the model behaviour can be highlighted:

1) Peak level magnitude is well approximated almost everywhere, though occasionally delayed.

2) The solution is smoothed out evidently.

3) The model inability to predict local inertial effect does not influence the rest of the simulation.

As mentioned above, no velocity measurement are available and no quantitative investigation of Froude number magnitude has been published so far for 2D numerical models. Figure 3.12 depicts the spatial variation of Froude number predicted by the present model. Given that these values arise themselves from a simplification of the original SWE, some statements can still be drawn: the maximum Froude number is often greater than 1 and always connected with the propagation of the front tip over the dry bed, as stated by the theory of shallow water (Toro, 2001); Froude number decreases soon after the passage of the front, so that the falling limb of the inlet hydrograph generates a gravity-driven flow.

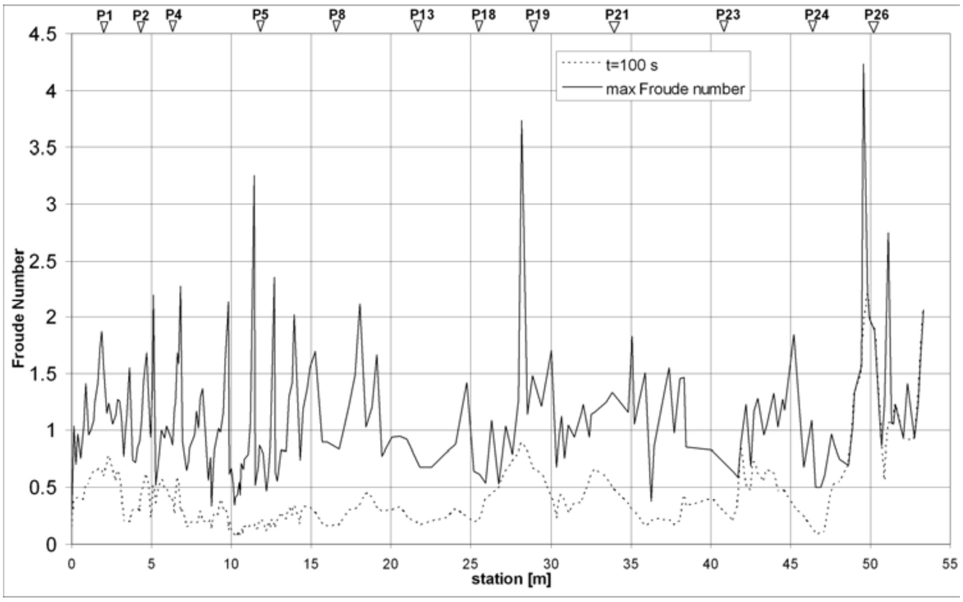

Figure 3.12 - Spatial variation of maximum Froude number over the entire simulation and its value at t=100 s

Analysis of the arrival times shows that the diffusive wave front slows down more than the experimental one. The maximum delay accumulated by the diffusive front at the end of the domain is comparable, and sometimes lower than the ones obtained by other numerical 2D models, whose results are summarized in Soares Frazão and Testa. The behaviour shown by the model, consisting of an advance of simulated front in the first part of the simulation and a delay in the last phase, can be found in other numerical models (Soares Frazão and Testa).

The results show how this simplified version of SWE can provide a robust tool to investigate the propagation of flood waves, even if caused by abrupt collapses of dams or levees. The NI model is clearly not able to simulate the formation and propagation of shock and reflections, but the influence of these local features is local and does not affect the overall dynamic.

Analysis of results allows to state that the parabolic approximation, even if it fails to reproduce some local phenomena such as high frequency oscillation, bores and run-up, is capable to simulate the propagation of such an impulsive wave over complex topography. The model is able not only to predict the general development of the event, but also to describe inundation arrival times, water levels' distribution and local peak values with precision comparable to other full dynamic numerical models on most parts of the domain. This is due to both the parabolic assumption, which intrinsically allows an easier treatment of wet–dry interfaces, and to the numerical scheme, which adequately deals with such transitions. This can be stated in view of the high impulsiveness of the considered test case. Local discontinuities are proved to have a small influence on the overall dynamic of the event: the application of models which make use of some approximations of the underlying physics is thus justified, and enforced by the minor computational effort they require. Summarizing, the present analysis suggests that the parabolic model may effectively reproduce the principal features of an inundation event, even in cases for which the diffusive approximation may seem unrealistic and the criteria proposed to assess the applicability of the NI wave may suggest the use of more complex models.

4. Full dynamic Shallow Water Models

In this chapter a numerical model to solve the SWE in full dynamic form is presented.

4.1 Numerical models

The full dynamic 2D SWE model described in section 2.2 is a hyperbolic set of nonlinear PDE. Its conservative integral form is here recalled:

$$\frac{\partial}{\partial t}\int_{\Omega}\mathbf{U}dv=-\int_{\partial\Omega}\underline{\underline{\mathbf{E}}}\cdot\hat{n}dA \tag{4.1}$$

where the vector of conserved unknown variables is:

$$\mathbf{U}=\begin{pmatrix}h & uh & vh\end{pmatrix} \tag{4.2}$$

the matrix of fluxes is:

$$\underline{\underline{\mathbf{E}}}=\begin{pmatrix}\mathbf{F} & \mathbf{G}\end{pmatrix}=\begin{pmatrix} hu & hv \\ hu^2+gh^2/2 & huv \\ huv & hv^2+gh^2/2 \end{pmatrix} \tag{4.3}$$

the vector of source terms is assumed to include the external mass source q, friction and bed slopes:

$$\mathbf{S}=-gh\begin{pmatrix}-q/(gh) & \frac{u\sqrt{u^2+v^2}}{\chi^2 h}-\frac{\partial z}{\partial x} & \frac{v\sqrt{u^2+v^2}}{\chi^2 h}-\frac{\partial z}{\partial y}\end{pmatrix} \tag{4.4}$$

where the friction slope is expressed by a Chezy type formula.
The numerical schemes implemented here are based on the Finite Volume (FV) method applied to unstructured grid. A first order solution, generally referred to as Godunov method or upwind

method, is employed. Two different higher order approaches, namely the WAF (Weighted Average Method) method and the MUSCL (Monotone Upstream-Centered Scheme for Conservation Laws) method are used as well. All the schemes are shock capturing conservative methods.

It is worth stressing the need of using conservative shock capturing methods. In fact it has been demonstrated by Lax and Wendroff (1960) that if a conservative method is convergent, then it will converge to a *weak solution* (in this context *weak solution* is used to refer to discontinuous solutions) of (2.23). Unfortunately the weak solutions of a hyperbolic PDE is not unique, and therefore a method, besides being conservative, it must be also entropy satisfying, in order to converge to the physical solution among the weak solutions (Harten, 1983). Moreover if a shock is present in the solution, a non conservative scheme will converge to the solution of a conservation law which is not (2.23). This is why it is compulsory to use a conservative scheme in presence of shocks.

4.1.1 The FV method

The FV method founds its basis on the definition of the spatial domain as a the union of non overlapping subdomains, also called cells or elements. The unknown quantities $\mathbf{U}$ are then assumed to vary over the domain but to be constant over each subdomain, i.e. piecewise constant. Let $\bar{\mathbf{U}}$ be the cell average:

$$\bar{\mathbf{U}} = \frac{1}{\int\limits_{\Omega} dv}\frac{\partial}{\partial t}\int\limits_{\Omega}\mathbf{U}dv = \frac{1}{|\Omega|}\frac{\partial}{\partial t}\int\limits_{\Omega}\mathbf{U}dv \tag{4.5}$$

assuming the cell has N_s sides defined by outward unit normal vector $\mathbf{n}_s = \left[n_S^{\langle 1\rangle}\ n_S^{\langle 2\rangle}\right]$, eq. (4.1) becomes:

$$\frac{\partial\bar{\mathbf{U}}}{\partial t} = -\frac{1}{|\Omega|}\sum_{s=1}^{N_s}\underbrace{\int\limits_{A_s}^{A_{s+1}}\left[n_S^{\langle 1\rangle}\mathbf{F}(\mathbf{U}) + n_S^{\langle 2\rangle}\mathbf{G}(\mathbf{U})\right]dA}_{F_s} \tag{4.6}$$

This semidiscrete form can be numerically implemented when a proper time approximation of the left hand time derivative together with an integration method for the left side are chosen.

Exploiting the rotational invariance of the SWE, formula (4.6), whose fluxes are expressed into global reference frame, can be rotated into a frame reference attached to the side S, using a rotation function $\mathbf{T}_S$ whose matrix representation in the global reference frame is:

$$\underline{\mathbf{T}}_S = \begin{pmatrix} 1 & 0 & 0 \\ 0 & n_S^{\langle 1 \rangle} & n_S^{\langle 2 \rangle} \\ 0 & -n_S^{\langle 2 \rangle} & n_S^{\langle 1 \rangle} \end{pmatrix} \tag{4.7}$$

the quantity in square brackets in (4.6) can be simplified to

$$n_S^{\langle 1 \rangle}\mathbf{F}(\mathbf{U}) + n_S^{\langle 2 \rangle}\mathbf{G}(\mathbf{U}) = \underline{\mathbf{T}}_S^{-1}\left\{\mathbf{F}\left[\underline{\mathbf{T}}_S(\mathbf{U})\right]\right\} \tag{4.8}$$

This means that there is no need to calculate both fluxes at each interface, as it is sufficient to apply only the x-split flux to the rotated datum $\underline{\mathbf{T}}_S(\mathbf{U})$, and then rotate the result back to the original frame. This last step guarantees the possibility to correctly sum the results of arbitrarily oriented edges.

This last property reduces the 2D formula (4.6) to a 1D expression (4.6), which is the base for unsplitted Finite Volume methods, particularly useful when dealing with unstructured meshes.

4.1.2 The Godunov method

The central point of the Godunov method is the use of wave propagation information of the hyperbolic PDE (section 2.2) to construct the numerical method. Here it will be briefly shown how. Given the rotational invariance of the SWE, eq. (4.1), posed in differential form, can be simplified to:

$$\mathbf{U}_t + \mathbf{F}(\mathbf{U})_x = \mathbf{0} \tag{4.9}$$

where x is the direction normal to the edge of the cell and centred at the interface. If, as in FV schemes, two adjacent cells have constant state at $t = t^{(n)}$, in the x local frame eq. (4.9) can be seen as a local Riemann problem with initial conditions:

$$\mathbf{U}\left(x, t^n\right) = \begin{cases} \mathbf{U}_i^n \leftarrow x < 0 \\ \mathbf{U}_{i+1}^n \leftarrow x > 0 \end{cases} \tag{4.10}$$

The Riemann problem is then used as a *building block*, that is a local Riemann problem is solved at each cell interface. Every cell will thus involve as many Riemann problems as the number of its edges. The telescopic property of conservative methods is here invoked in order to solve each Riemann problem only once.

Substituting Equation (4.8) into (4.6):

$$\frac{\partial \overline{\mathbf{U}}}{\partial t} = -\frac{1}{|\Omega|} \sum_{s=1}^{N_s} \mathbf{T}_s^{-1} \mathbf{F}\left(\mathbf{T}_s \mathbf{U}\right) \tag{4.11}$$

It is still necessary to establish how to calculate the fluxes to be integrated. The solution to the Riemann problem at interface $i + 1/2$, being a similarity solution (see section 2.2.1), is referred to as $\mathbf{U}_{i+1/2}\left(x/t\right)$. Godunov method calculates each flux exactly at the interface between the two cells:

$$\mathbf{F}\left[\mathbf{T}_s \mathbf{U}\left(x/t\right)\right] = \mathbf{F}\left[\mathbf{T}_s \mathbf{U}\left(0\right)\right] \tag{4.12}$$

Once all the Riemann problems involving all cells boundaries are solved the solution can be easily advanced in time.

The solution to the Riemann problem can be exact or approximate. In this thesis an exact solution is always used (see section 2.2.1), even for higher order schemes.

Once all the Riemann problems involving all cells boundaries are solved the solution can be easily advanced in time.

4.1.3 WAF second order method for the homogeneous equations

The WAF (Weighted Average Flux) approach was developed by Toro (1986) but has its origin in the random choice method (Toro, 1986; Toro and Roe, 1987). It is a second order scheme, both in space and time, and it is simpler and less demanding than reconstruction method like MUSCL (Monotone Upstream-centered Scheme for Conservation Laws). In fact the WAF technique assumes, as in the first order Godunov scheme analysed in the previous section, that the variables are constant over each cell. The spirit of the method resides in extending the calculation of the numerical flux at the interface, as in the first order method (eq. (4.12)), and in other positions of the wave structure originating from the local Riemann problem. The solution in the WAF method is calculated by means of the usual update formula (4.11), but the numerical flux is determined as the following integral average:

$$\mathbf{F}\left[\mathbf{T}_s\mathbf{U}\right]=\frac{1}{t_2-t_1}\frac{1}{x_2-x_1}\int_{t_1}^{t_2}\int_{x_1}^{x_2}\mathbf{F}\left[\widehat{\mathbf{U}}\left(x,t\right)\right]dx\,dt \qquad (4.13)$$

where $\widehat{\mathbf{U}}\left(x,t\right)$ is the solution of the Riemann problem over the whole wave structure and the limits of integration x_2, x_1, t_2, t_1 are arbitrary. A possible choice, justified by the good behaviour of the consequent numerical scheme, is: $x_2=\frac{\Delta x}{2}$, $x_1=-\frac{\Delta x}{2}$, $t_2=\Delta t$, $t_1=0$. If the time integral is solved using the midpoint approximation it yields:

$$\mathbf{F}\left[\mathbf{T}_s\mathbf{U}\right]=\frac{1}{\Delta x}\int_{-\frac{\Delta x}{2}}^{\frac{\Delta x}{2}}\mathbf{F}\left[\widehat{\mathbf{U}}\left(x,\Delta t/2\right)\right]dx \qquad (4.14)$$

It is useful to remark that this specific formulation is valid for uniform space discretization: being eq. (4.14) a 1D numerical flux normal to a side of a general element, the adjacent element is forced to be the same size. In order to apply the WAF scheme to a non uniform spatial discretization an extension of the method is derived in the next section. For the a general set of N conservation laws the spatial integral can be divided into $N+1$ contributes, each defining a region between two waves. Each contribute is weighted by the width of its wedge at $t=\Delta t/2$. For the SWE set $N=3$ so 4 fluxes must be averaged, as explained in Figure 4.1.

$$\mathbf{F}\left[\mathbf{T}_s\mathbf{U}\right]=\frac{1}{\Delta x}\sum_{k=1}^{N+1}\overleftrightarrow{w}_k\mathbf{F}\left[\widehat{\mathbf{U}}\left(x^{(k)},\Delta t/2\right)\right] \tag{4.15}$$

$$\mathbf{F}\left[\mathbf{T}_s\mathbf{U}\right]=\sum_{k=1}^{N+1}w_k\mathbf{F}\left[\widehat{\mathbf{U}}\left(x^{(k)},\Delta t/2\right)\right] \tag{4.16}$$

where the nondimensional weight w_k is the length of the kth segment relative to the cell width Δx, and can be expressed as function of the two bounding waves' speeds: $w_k=\frac{\Delta t}{2\Delta x}\left(S_k-S_{k-1}\right)$ where $S_0=-\frac{\Delta x}{\Delta t}$ and $S_0=\frac{\Delta x}{\Delta t}$ is the *grid speed*. Note that in Figure 4.1 the sketch is intentionally generalised to the case of non-uniform discretization, as it will be necessary to make reference to such a general case later on.

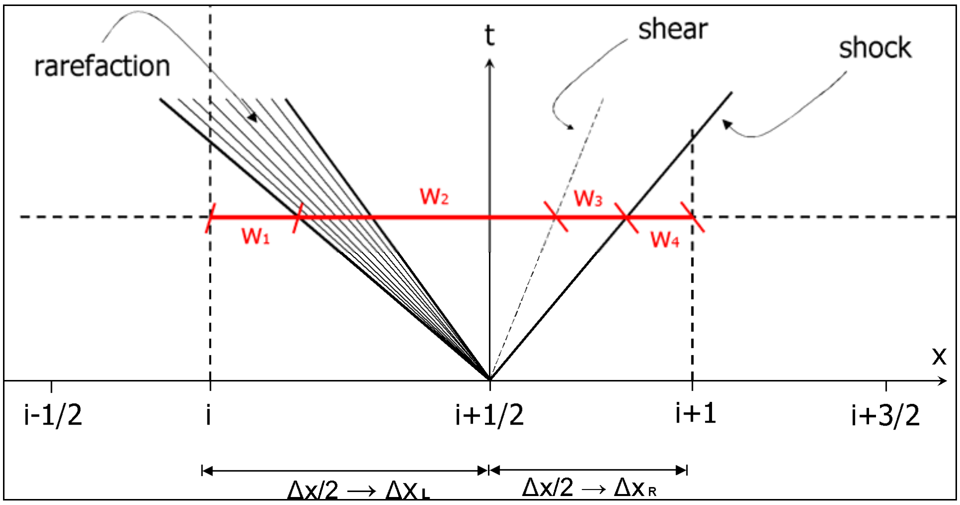

Figure 4.1 – Structure of the Riemann wave pattern at the interface between element *i* and *i+1*; WAF weights (red) for application to unstructured mesh.

If a rarefaction occurs in the wave structure, the formulation (4.15) can be considered an approximation of the exact average, as solution varies inside the rarefaction. As depicted in Figure 4.1 the rarefaction is considered an extension of the adjacent *star* region. This approximation has been empirically proved to work well provided that the rarefaction is not critical: the rarefaction is said to be critical, that is the flow passes from subcritical to supercritical state, when its tail and its head have opposite speeds. In this case, it would be safer to add in the summation in eq. (4.15) another region w_{N+2} as wide as the rarefaction wave, and evaluate the extra contribute across the wave. However, it has been found that a simpler strategy works well too: it is sufficient to replace the star solution in the augmented region (rarefaction wave + star region) with the first order Godunov flux, as in eq (4.12). If no correction is made, then the solution shows an unphysical jump in variables distribution across critical points, called entropy glitch. It is worth noting that this problem arises only if an exact Riemann solver is employed: most of the approximate solvers available integrate an entropy fix, which account for the presence of those extra unphysical solutions.

According to Godunov Theorem (Toro 1999a), this second order *linear* scheme, produces spurious oscillations when applied to non-linear equations, such as SWE. A nonlinear TVD (Total Variation Diminishing; Harten, 1983; Harten, 1984) version of the WAF scheme makes use of some limiters of the averaged flux. The formulation of the non-TVD version for uniform grid (4.16) can be simplified collecting the S_k inside the summation:

$$\mathbf{F} = \frac{1}{2}\left[\mathbf{F}^{(L)} + \mathbf{F}^{(R)} + \frac{\Delta t}{\Delta x}\sum_{k=1}^{N} S_k \ \Delta\mathbf{F}^{(k)}\right] \tag{4.17}$$

where $\mathbf{F}^{(L)} = \mathbf{F}^{(1)}$ and $\mathbf{F}^{(R)} = \mathbf{F}^{(4)}$ are the fluxes evaluated at the two initial states of the Riemann problem, namely the two adjacent cells; $\Delta\mathbf{F}^{(k)} = \mathbf{F}^{(k)} - \mathbf{F}^{(k+1)}$ is the difference of the flux across the wave.

The spirit of the TVD version (Roe, 1981) is to continuously investigate the behaviour of the solution near the cell interface (namely evaluating the gradients), analysing the variations of the quantities across each wave. Based on this investigation a strategy for a smart use of the numerical viscosity is chosen, by means of the so called *limiter function*. The variation $r^{(k)}$ of the quantities across the kth wave is then used to evaluate a limiter function $LF\left(r^{(k)},\left|S_k\right|\right)$, where $r^{(k)}$ is:

$$r^{(k)} = \begin{cases} \dfrac{q_i^{(k)} - q_{i-1}^{(k)}}{q_{i+1}^{(k)} - q_i^{(k)}} & S_k > 0 \\ \dfrac{q_{i+2}^{(k)} - q_{i+1}^{(k)}}{q_{i+1}^{(k)} - q_i^{(k)}} & S_k < 0 \end{cases} \tag{4.18}$$

The quantity $r^{(k)}$ compares the variation of the quantity *q* across the kth wave in the upstream direction ($i-1/2$ or $i+3/2$), with the variation at the interface $i+1/2$ (local change). For the application to the x-split of the 2D-SWE, the depth can be chosen as the variable *q* in (4.18), except for the middle wave (*k=2*), for which the only discontinuous variable available is the tangential particle velocity *v*. The construction of TVD limiters (either flux limiters or slope limiters) must follow some specific rules deduced from the analysis of data compatibility concepts, which, though very stimulating, are not reported here (see Toro, 1999 for a deduction of the TVD limiters). The most common limiters functions are the ULTRABEE (Roe, 1983), SUPERBEE (Roe, 1983), VANLEER (van Leer, 1973a-b), VANALBADA (van Albada et alii, 1982) and MINBEE (Roe, 1983). Their formulation can be found in Toro (1999), here only the SUPERBEE function is recalled, as it will be necessary in the following section:

$$LF\left(r^{(k)},\left|c_k\right|\right) \equiv LF_k = \begin{cases} 1 & r^{(k)} \le 0 \\ 1-2r^{(k)}\left(1-\left|c_k\right|\right) & 0 \le r^{(k)} \le 1/2 \\ \left|c_k\right| & 1/2 \le r^{(k)} \le 1 \\ 1-r^{(k)}\left(1-\left|c_k\right|\right) & 1 \le r^{(k)} \le 2 \\ 2\left|c_k\right|-1 & r^{(k)} \ge 2 \end{cases} \quad (4.19)$$

where $c_k = S_k / S_0$ is the Courant number of the kth wave, so that $\operatorname{sign}(c_k) = \operatorname{sign}(S_k)$. The TVD version of the WAF scheme is then:

$$\mathbf{F}^{TVD} = \frac{1}{2}\left[\mathbf{F}^{(L)} + \mathbf{F}^{(R)} + \sum_{k=1}^{N} \operatorname{sign}(S_k)\, LF_k\, \Delta\mathbf{F}^{(k)}\right] \quad (4.20)$$

In order for the limiter function to maintain high accuracy for smooth solutions, it must be equal to 1 at regions with low gradients ($r^{(k)} = 1$), so that no numerical viscosity is added.

In the next section a modification of the WAF TVD scheme is introduced, to work on non-uniform (and potentially unstructured meshes) grids.

4.1.3.1 WAF limiters for unstructured mesh

The method described in the previous section is here extended to work with non-uniform grids, and a TVD version introduced.

The SWE code built in this part of the thesis is specifically made to work with non-uniform unstructured triangular meshes. It is worth recalling that while an unstructured mesh is a set of nodes/elements whose locations in the space is not deducible from their indices (ie *(x,y)= f(i,j)*), a non-uniform mesh, obviously, is a mesh whose elements have different sizes and/or shapes. A structured mesh has many coding advantages (mainly due to memory storage techniques) and a uniform mesh usually yields much better results in terms of accuracy, but both make it difficult (or impossible) to conform a single block to a complicated boundary shape (cut cell methods are required in case of uniform grids), or obtain a local coarsening without much distortion of the elements.

In the following non-uniform and unstructured meshes will be simply referred to as *unstructured meshes*.

It is necessary to reformulate the weights in (4.16), with reference to Figure 4.1:

$$w_k = \frac{1}{\Delta x_L + \Delta x_R} \begin{cases} \Delta x_L + S_1 \, \Delta t/2 & k = 1 \\ (S_2 - S_1)\,\Delta t/2 & k = 2 \\ (S_3 - S_1)\,\Delta t/2 & k = 3 \\ \Delta x_R - S_1 \, \Delta t/2 & k = 4 \end{cases} \qquad (4.21)$$

The same approximations discussed in the previous section regarding the sonic rarefactions are used here.

This simple modification is sufficient to ensure applicability of non-TVD version to non-uniform meshes, and substitution of (4.21) into (4.16) yields the required formula for the flux, corresponding to (4.17):

$$\mathbf{F} = \frac{1}{\Delta x_L + \Delta x_R} \left[\Delta x_L \mathbf{F}^{(L)} + \Delta x_R \mathbf{F}^{(R)} + \frac{\Delta t}{2} \sum_{k=1}^{N} S_k \; \Delta \mathbf{F}^{(k)} \right] \qquad (4.22)$$

In order to obtain a suitable TVD version, instead of using a nondimensional limiter function, as in eq. (4.20), a *limited wave speed* S_k^{lim} is used directly in eq. (4.22):

$$\mathbf{F} = \frac{1}{\Delta x_L + \Delta x_R} \left[\Delta x_L \mathbf{F}^{(L)} + \Delta x_R \mathbf{F}^{(R)} + \frac{\Delta t}{2} \sum_{k=1}^{N} S_k^{lim} \; \Delta \mathbf{F}^{(k)} \right] \qquad (4.23)$$

where S_k^{lim}, if a SUPERBEE is again taken as an example, is:

$$S_k^{lim}=\begin{cases}\Delta x_{R,L}/\Delta t & r^{(k)}\le 0\\ \left(1-2r^{(k)}\right)\Delta x_{R,L}/\Delta t+2r^{(k)}\left|S_k\right| & 0\le r^{(k)}\le 1/2\\ \left|S_k\right| & 1/2\le r^{(k)}\le 1\\ \left(1-2r^{(k)}\right)\Delta x_{R,L}/\Delta t+r^{(k)}\left|S_k\right| & 1\le r^{(k)}\le 2\\ 2\left|S_k\right|+\Delta x_{R,L}/\Delta t & r^{(k)}\ge 2\end{cases} \qquad (4.24)$$

This limited wave speed depends on the sign of the speed itself, namely:

$$\Delta x_{R,L}=\Delta x_L+\Delta x_R+\operatorname{sign}\left(S_k\right)\left(\Delta x_R-\Delta x_L\right) \qquad (4.25)$$

Analogous expressions corresponding to the other common limiter functions (see the previous sections) can be easily obtained and are not reported here for the sake of brevity.

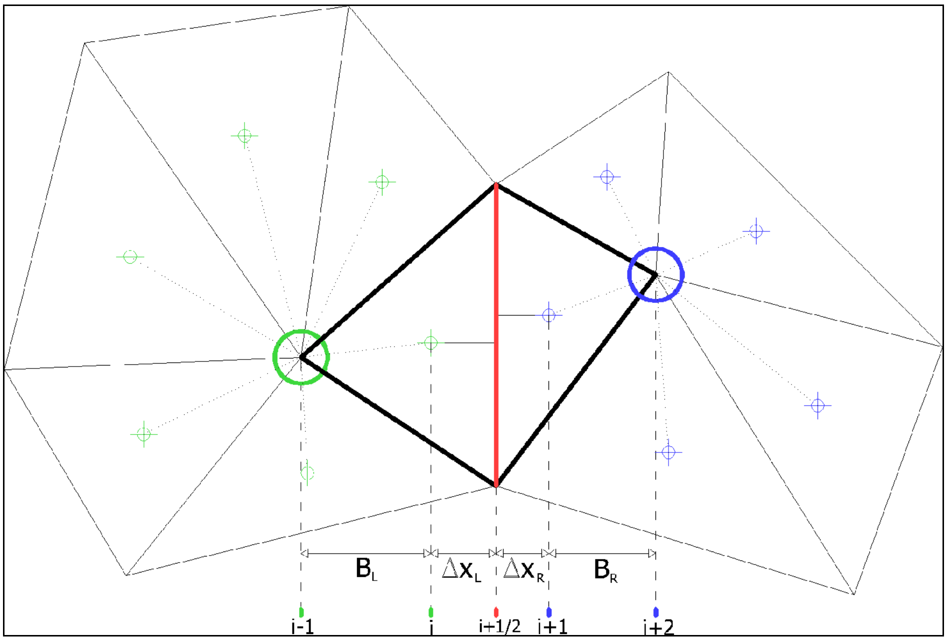

Figure 4.2 – Green and blue triangles contributes to the average nodal value, used in the non-uniform unstructured TVD gradient evaluation.

Finally, the quantity which measures the gradient of the variable, and then weighs the limiting of the flux, namely $r^{(k)}$, needs to be modified as well:

$$r^{(k)} = \begin{cases} \dfrac{\Delta x_L + \Delta x_R}{B_L} \dfrac{q_i^{(k)} - q_{i-1}^{(k)}}{q_{i+1}^{(k)} - q_i^{(k)}} & S_k > 0 \\ \dfrac{\Delta x_L + \Delta x_R}{B_R} \dfrac{q_{i+2}^{(k)} - q_{i+1}^{(k)}}{q_{i+1}^{(k)} - q_i^{(k)}} & S_k < 02\Delta x_R \end{cases} \tag{4.26}$$

The quantities B_L and B_R depend on the type of mesh used. They are the distances between the two interfaces at which the values of the variable q is evaluated. For a structured, though non-uniform mesh, there are always two *left* and *right interfaces* at which the variable can be evaluated. For a triangular non-uniform unstructured mesh, like the one used in this thesis, no such interfaces exist. A different approach is chosen here (making reference to Figure 4.2): the variables $q_{i-1}^{(k)}$ and $q_{i+2}^{(k)}$ appearing in (4.26) are approximated by the nodal values at the two nodes opposite to the central interface $i+1/2$. The nodal values are the weighted averages of the neighbouring cells, where the weights are the distances of the barycentres from the nodes.

4.1.3.2 Boundary conditions

Dirichlet-type boundary condition is implemented in both Godunov and WAF models. This type of BC can be then used to model absorbing, reflecting or flux-imposed BC. A standard technique making use of *ghost cells* is used here. It consists of adding a fictitious cell for every boundary edge, and imposing the required mathematical boundary condition (values of the averaged quantities) on that cell. The *bounding cell* (which is the cell in the domain that has at least one side at the boundary) can be connected to more than one ghost cell (up to n-1 for a n-sided cell). The technique is straightforward and no particular treatment is needed as the ghost cells are considered part of the domain. Moreover there is no need to examine the flow state (super or subcritical) at the boundary in order to determine whether perturbations are allowed to enter the domain or not: this is accounted for automatically as the boundary edges are treated like all other internal edges.

Some problems arise when a higher order scheme is employed, as the stencil area in these methods generally is broader than first order schemes. For second order scheme the limiter function requires the evaluation of gradient (4.18) which cannot be accomplished using only the values of the two elements involved. The procedure used here for unstructured meshes is explained in the previous section. When dealing with boundary edges, the nodal value at the right of the interface (*i+2* in Figure 4.2) is taken equal to the value of the ghost cell. This procedure has empirically proven to preserve high order at the boundary only when the bottom of the bounding cell is horizontal: the presence of a sloping boundary leads to a loss of accuracy, as will be shown in section 4.2.4. This issue is currently undergoing further investigation.

4.1.4 Source terms treatment

Source terms numerical treatment is the crucial point in the SWE solution. All the methods explained in the previous sections are aimed at solving the homogeneous form of the conservation law, as in eq. (4.9). Here some standard techniques that can be used when source terms arise, are applied and their effectiveness is discussed. Some slight modifications are then examined, which lead to better results.

The inhomogeneous problem is:

$$\begin{aligned} &\mathbf{U}_t + \mathbf{F}(\mathbf{U})_x = \mathbf{S}(\mathbf{U}) \\ &\mathbf{U}\left(x, t^{(n)}\right) = \mathbf{U}^{(n)} \end{aligned} \qquad (4.27)$$

The standard technique in order to advance the solution in time, when in presence of source terms, the so-called *splitting* or *fractional-step* methods. It should be highlighted that, in order to avoid confusion, in the context of source term treatment, the word *splitting* refers to *time*-splitting: however the same expression is also used to refer to *space*-splitting when eq (2.23), for example, is solved by integrating separately the *x* and *y* contributes to the divergence. These methods basically solve the homogeneous part of the PDE, and then use the solution just obtained as the initial value for a ODE in time. The above strategy can be formally written as:

$$\textit{step 1} \left\{ \begin{array}{l} \mathbf{U}_t + \mathbf{F}(\mathbf{U})_x = \mathbf{0} \\ \mathbf{U}\left(x, t^{(n)}\right) = \mathbf{U}^{(n)} \end{array} \right\} \xrightarrow{\Delta t} \mathbf{U}^{(adv)} \tag{4.28}$$

$$\textit{step 2} \left\{ \begin{array}{l} \dfrac{d\mathbf{U}}{dt} = \mathbf{S}(\mathbf{U}) \\ \mathbf{U}\left(x, t^{(n)}\right) = \mathbf{U}^{(adv)} \end{array} \right\} \xrightarrow{\Delta t} \mathbf{U}^{(n+1)} \tag{4.29}$$

where step 1 is any solution scheme for the homogeneous SWE. Step 1 is often referred to as the *advection* operator $A^{(\Delta t)}$ while step 2 is called the *source* operator $S^{(\Delta t)}$. Both operators advance the solution in time of Δt but the overall strategy does not advance the solution of $2\Delta t$ because each step only uses some information of the original inhomogeneous PDE. The overall accuracy of the method is the crucial part of the problem. In general the splitting strategy (4.28), (4.29) introduces a splitting error $O(\Delta t)$ independently of the single schemes used in the two steps. Even if, for example, second order accurate schemes are used for $A^{(\Delta t)}$ and $S^{(\Delta t)}$, this does not imply that the final result, i.e. $\mathbf{U}^{(n+1)}$, will be second order accurate. The opposite obviously holds, namely, if a kth-order accurate solution is sought then two kth-order operators must be used. There are special cases for which the use of two kth-order accurate operators is enough to obtain a kth-order accurate solution. These kind of equations also enjoy the properties of *commutation* of the two operators. They introduce no splitting error, that is the solution by means of non-splitting scheme is exactly the same as the one obtained by a splitting procedure. This is because the process represented by the source term acts on the solution independently of the its spatial and temporal location. The following example will help to clarify the problem.

$$\begin{aligned} & d_t + u d_x = -\beta d \qquad \forall x \in \mathbb{R}, \quad \forall t \in \mathbb{R}^+ \\ & d(x,0) = \tilde{d}(x) \end{aligned} \tag{4.30}$$

This linear advection-reaction equation is used to model the transport of a contaminant whose concentration d in a fluid moving at constant speed u. Its concentration decreases at a constant rate, as result of some chemical reaction. In this case the exact solution is the advection of the initial distribution $\tilde{d}(x)$, damped by the action of β, namely:

$$d(x,t) = e^{-\beta t}\tilde{d}(x-ut) \tag{4.31}$$

Note that the solution is the solution of the homogeneous part $\tilde{d}(x-ut)$, times the damping factor which is independent of d. Applying the step 1 (4.28) for a time step Δt would lead to:

$$d^{(adv)}(x,\Delta t) = \tilde{d}(x-u\Delta t) \tag{4.32}$$

and step 2 (4.29) would then be used to solve:

$$\begin{aligned} & d_t = -\beta d \\ & d(x,0) = \tilde{d}(x-u\Delta t) \end{aligned} \tag{4.33}$$

whose solution is exactly (4.31).

If the reaction is influenced by the position of the particle of the contaminant, namely $\beta = \beta(x)$, a splitting error would appear, causing the degrading of the overall accuracy to first order. This is intuitive, as the advection of the contaminant prior to its reaction would modify the reaction itself. Unfortunately, this is also the case of the SWE with source terms. However, a modification of the splitting process can lower the splitting error, and take the overall accuracy back to the minimum of the accuracy used in step 1 and 2. As usual in the numerical procedures, the idea is to halve the time step to allow for the two process mutual interaction. The idea is to apply the following solution chains:

$$d^{(n+1)} = S^{(\Delta t/2)} A^{(\Delta t/2)} S^{(\Delta t/2)} d^{(n)} = A^{(\Delta t/2)} S^{(\Delta t/2)} A^{(\Delta t/2)} d^{(n)} \qquad (4.34)$$

This procedure, often called Strang splitting (Strang, 1968), implies a higher computational effort compared to simple splitting, because two source operators (or two advective operators) must be applied to advance the solution of Δt (the order of application of $A^{(\Delta t/2)}$ and $S^{(\Delta t/2)}$ does not change the final result). However it can be proven that, if a simple splitting procedure as in (4.28) and (4.29) is applied to an even numbers of advancements in time, and if the two operators are applied with alternate orders, then the whole method reproduces the Strang splitting. the shortcoming of this approach is that within a single time step only two operators must be applied, as in the original simple splitting. However care must be taken when the method is applied to algorithm with variable time step: a smooth variation of the time step is usually enough to ensure accuracy.

Within the splitting strategy an ODE solver must be chosen.

For the SWE, when step 1 (4.28) is solved with a first order accuracy, and when source term includes only bed slope, a standard solution by means of forward Euler method (FE) is exact over a time step Δt. This is because in the source term (4.4) can be written as:

$$\mathbf{S} = -gh\begin{pmatrix} 0 & \dfrac{\partial z}{\partial x} & \dfrac{\partial z}{\partial y} \end{pmatrix} \qquad (4.35)$$

the bed slope terms depending only on the depth value, which is constant in a first order solution. Note that in this case the application of Strang procedure is not necessary.

When the homogeneous part (4.28) in solved with higher order methods, a more accurate ODE solver has to be used as well.

A *multistep* solver is not feasible because no solution is known from previous time steps. The IC $\mathbf{U}^{(adv)}$ of the ODE problem cannot be coupled to other solutions, e.g. $\mathbf{U}^{(n-1)}$, because they are solution to different problems, namely the whole inhomogeneous problem.

A *multistage* solver must then be used and a Runge-Kutta (RK) explicit solver has been implemented here. The order of accuracy of the solver is equal to the number of stages employed, if lower than 5. The RK4 method is therefore implemented here.

When the friction term is included, the RK method is required even for a 1st order solution.

4.1.4.1 SGM-like for WAF for unstructured mesh

The fractional-step method is quite effective when used to simulate varying flows. It is well known that it is not accurate when applied to steady or quasi-steady flows. The first to notice this inaccuracy was Ambrosi (1995), when using Roe's approximate Riemann solver. The problem, quite simple to identify, is still central in the research field. In the context of FV schemes, the use of upwind methods to solve the homogeneous part of the SWE cannot be coupled with discretization of source terms which does not take into account the wave structure, i.e. depends only on the local values of the unknowns. The usual centred discretization of the source terms in fact leads to non-conservative schemes because of the imbalance between the flux gradients, upwinded, and source terms, centered. Bermúdez and Vázquez (1994) and Vázquez-Cendón (1999) proposed upwind methods for the treatment of the bed slope source terms. Hubbard and Garcia-Navarro (2000) extended this numerical treatment to higher-order TVD schemes. These methods greatly improved the accuracy of the numerical solution. They are quite simple to implement but computationally heavy: they almost double the computational effort, as they numerically treat source terms like gradient of fluxes.

A simple but helpful reasoning shows how an explicit scheme applied along with source term simple splitting (4.28) and (4.29), cannot preserve mass balance. The following example is a case of water at rest, over a indefinite sloping bed. For the sake of simplicity the fluxes can be calculated with a first order Godunov model as in eq. (4.12). Fluxes are decreasing from left to right ($F_k > F_{k+1}$), in fact the following relations hold:

$$\begin{aligned} & h^*_{i-1/2} > h^*_{i+1/2} \qquad u^*_{i-1/2} > u^*_{i+1/2} \\ & \mathbf{F}_{i-1/2} = \mathbf{F}\left(h^*_{i-1/2}, u^*_{i-1/2}\right) > \mathbf{F}\left(h^*_{i+1/2}, u^*_{i+1/2}\right) = \mathbf{F}_{i+1/2} \\ & \mathbf{U}^{(adv)} = \mathbf{U}^{(n)} - \frac{\Delta t}{A}\left[\mathbf{F}_{i+1/2} - \mathbf{F}_{i-1/2}\right] \end{aligned} \tag{4.36}$$

In each cell $\mathbf{U}^{(adv)} > \mathbf{U}^{(n)}$. The first element of $\mathbf{U}$ is h so this yields $h^{(adv)} > h^{(n)}$. The *advection* operator so increases the water levels everywhere as it cannot distinguish between the two situations in Figure 4.3. The *source* operator acts only on the momentum equation so it cannot correct the wrong mass balance enforced by the *advection* operator. It then results, for every cell

$$h^{(n)} < h^{(adv)} = h^{(n+1)} \tag{4.37}$$

Now it should be clearer how the Strang splitting enhances accuracy: if the *source* operator had acted before *advection* operator, it would have modified velocities (again, it does not act on depth field) so that the *advection* operator could have predicted a lower mass balance error.

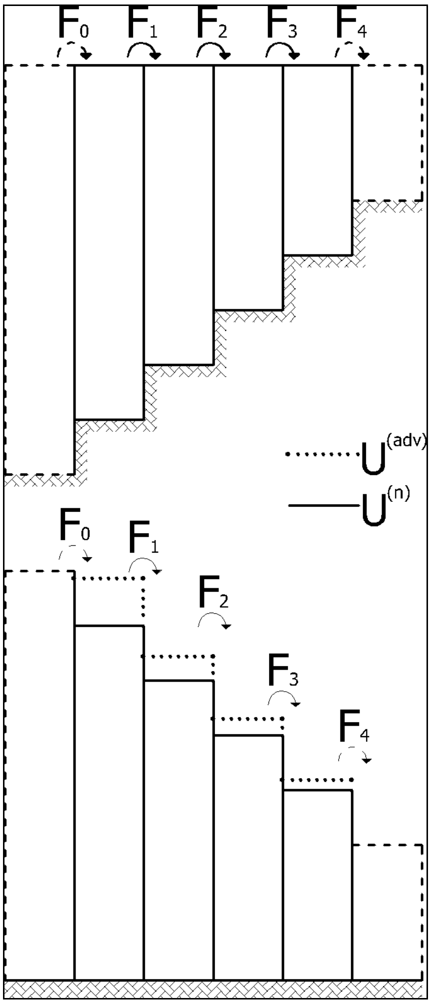

Figure 4.3 – Advancing the solution with explicit scheme, using a fractional step method. The mechanism of formation of spurious motion starting from still water over a sloping bed.

The Strang approach only improves the accuracy, but does not guarantee the ability to exactly simulate water at rest. However its simplicity balances the inaccuracy of the results, as it will be clearer further on. The failure of the system is obviously connected to the independence of the two steps in the splitting scheme. In fact the advection phase acts only on the *depth field*, as if the bed was flat. The source operator then acts like a correction, but, as seen in the previous simple example, it is not enough. A modification in order to let the advection operator *know* some information about the bed slope is therefore needed, and is implemented in the present work. The idea behind the strategy applied in this thesis was initially proposed by Zhou et al. (2001). They developed a simple Surface Gradient Method (SGM) for treating source terms based on an accurate reconstruction of the conservative variables at cell interfaces. The method was applied to MUSCL technique. The original simple idea is to maintain the *centered* discretization for the source term while incorporating the influence of the bed slope into the numerical flux, by using the water surface gradient instead of the depth gradient. Formally this approach is feasible when the source term takes the form of a derivative. It is possible to incorporate some part of the source term that can be expressed as a derivative within the numerical flux, and then apply an appropriate discretization to the remaining component of the source.

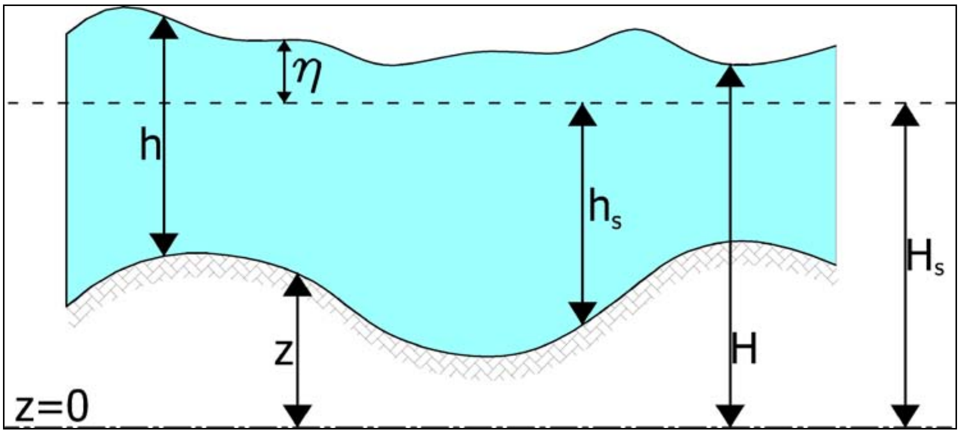

Figure 4.4 – Sketch of the reference used for the SWE on uneven bottom.

Making reference at Figure 4.4 the following relations hold:

$$\begin{aligned} & H = h + z = H_s + \eta \quad , \quad h = h_s + \eta \\ & \frac{\partial h_s}{\partial x} = -\frac{\partial z}{\partial x} \quad , \quad \frac{\partial H}{\partial x} = \frac{\partial \eta}{\partial x} \end{aligned} \tag{4.38}$$

The term $h\frac{\partial \eta}{\partial x}$ is generally split into:

$$h\frac{\partial\eta}{\partial x}=\frac{\partial\left(h^2/2\right)}{\partial x}+h\frac{\partial z}{\partial x} \tag{4.39}$$

the first part being part of the flux as in eq. (4.3), and the residual assigned to source terms. In order to pass information about the surface field, and not only the depth field, to the advection operator, the term $h\frac{\partial\eta}{\partial x}$ can be split in different ways:

$$\begin{aligned} & h\frac{\partial\eta}{\partial x}= \\ & \text{a)}\frac{1}{2}\frac{\partial}{\partial x}\left(\eta^2+2\eta h_s\right)-\eta\frac{\partial h_s}{\partial x} \\ & \text{b)}\frac{1}{2}\frac{\partial}{\partial x}\left(h^2-h_s^2\right)-\eta\frac{\partial h_s}{\partial x} \\ & \text{c)}\frac{1}{2}\frac{\partial}{\partial x}\left(h^2+z^2\right)-H\frac{\partial z}{\partial x} \end{aligned} \tag{4.40}$$

All of these modifications have the property to generate a term in form of *x*-derivative that can be substituted to the first part of (4.39), without affecting the hyperbolicity of the homogeneous SWE. Moreover if the approach c) is chosen in (4.40) the flux, as expressed originally, can be easily modified as follows:

$$\widehat{\mathbf{F}}^{(1)}=\begin{pmatrix} hu \\ hu^2+1/2\left(h^2+\delta z^2\right) \\ huv \end{pmatrix} \tag{4.41}$$

where $\delta=1,0$ is used as a switch to activate this approach. Obviously the source term must be modified, but the modification required is straightforward:

$$\widehat{\mathbf{S}}=-g\left(h+\delta z\right)\begin{pmatrix} 0 & -\frac{\partial z}{\partial x} & -\frac{\partial z}{\partial y} \end{pmatrix} \tag{4.42}$$

4.1.5 Wet-dry transition management

The wet-dry (WD) transition is a critical step in the modelling of shallow water flows. As stated in section (2.2) the original SWE set is strictly hyperbolic for positive depth, hyperbolic at dry locations and loses its hyperbolicity whenever negative depths are calculated. Although the local Riemann problem admits an exact solution for dry initial states (see section 2.2), and thus allow for the propagation over dry areas, the numerical application suffers of several problems.

One of the first authors to try to carry out an analysis on this topic was Balzano (1998). He stated that WD issues are two-fold: (i) a physical one related essentially to the insufficient knowledge of suitable resistance laws which apply to situations characterized by a thin water film on ground irregularities of the same order of magnitude (Kowalik and Murty, 1993); (ii) a numerical one related to the occurrence of mass unbalance, wiggles or even real instabilities in the computations based on fixed grids Leendertse, 1987; Stelling, 1984.

The first issue, that is the appearance of other phenomena not accounted for in the SWE, though very important, will not be discussed here.

The second one is still a central part of recent research. The main difficulty is connected to the abrupt transition between dry and wet states, intrinsically implied by a numerical approach, compared to the smooth transition that occurs at natural fronts. In the framework of discrete mathematics the minimum depth available would be only dependent on the precision of the number representation used. Moreover, if the SWE in conservative form are used, then over/underflows inevitably arise when evaluating particle velocities, or, at best, rounding errors become dominant in the solution $\left(U = Uh/h\right)$. This implies that an artificial minimum depth must be used to identify the wet areas.

Tchamen and Andkahawita, (1998) also give an extensive description of the problems related to WD treatment. They strongly state that the accuracy of the definition of both the numerical bed and the water surface variation is crucial in order to obtain a coherent numerical scheme. Most of the techniques described there are still used in the SWE numerical modelling. Some of them treat the wet-dry interface as a moving boundary: this approach would imply that some specific and arbitrary boundary condition should be found in order to resemble the behaviour of a WD front, together with some laws that describe the movement of the mesh. This Lagrangian approach implies the presence of a moving mesh capable of tracking fronts' position (Vasiliev, 1970; Katopodes and Strelkoff 1978; Lynch and Gray, 1980; Di Monaco and Molinaro, 1984; Okamoto et al. 1992; Zelt, 1986; Akanbi and Katopodes, 1988; Stockstill et al. 1997), Other more general adaptive grid algorithms, which allow nodes to be added or deleted dynamically (Titov and Synolakis 1995), are still cumbersome, particularly if long-term computations are to be carried out, as in the case of environmental problems. Eulerian , or fixed grid, algorithms can be generally classified into minimum positive depth (MPD) and non-MPD. In the first class, the negative water depths are artificially substituted by an imposed depth able to guarantee numerical stability. Non-MPD models force a higher threshold depth on the whole domain, so that no dry cells exist according to some sort of depth-based cell classification like Tasi (2000). Regardless of the numerical techniques adopted, all numerical models presented so far, make use of some sort of tolerance in the water depth, then used to trigger some special treatment, which is often no more than a programming trick.

The most common approaches are (i) the ones derived from Brufau et al. (2002) who adopted a temporary modification of the bed elevation that renders the cell completely wet, in conjunction with a fairly complicated permutation of the source term upwinding technique: when topography emerges at an interface it is redefined in the dry cell in order to avoid the appearance of spurious pressure forces and to satisfy condition; (ii) the ones similar to the solution originally proposed by Titov and Synolakis 1995 and recently presented by Bradford and Sanders (2002) and Begnudelli and Sanders (2006) who substitute the momentum equation at front interface with an extrapolation of the particle velocity from the wet portion to the dry one. This is to address the problem of setting a zero particle velocity at the front, which often causes numerical instabilities with negative depths being prone to appear in the solution. Even if this problem rarely occurs in the wetting phase, it is quite common in the drying one, as the water surface slope cannot exceed the bottom slope (Horritt, 2002); (iii) Tao (1984) proposed the so-called slot-method which introduce a porous bed, in order to avoid the distinction between wet and dry elements; similar approaches have been adopted by several authors, in the field of Boussinesq-type equations for runup in the coastal hydraulic field (Kennedy et al., 2000; Ip et al., 1998), finite element methods (Jiang and Wai, 2005; Heniche et al. 2000); the marsh porosity concept was then used (MacArthur et al., 1990) and implemented in commercial codes like RMA2 (King 2000; Donnell et al. 2001), though its parameters are found to markedly affect the propagation features (Nielsen and Apelt, 2003).

Though the problem is intrinsic to the propagation over dry bed, it is exacerbated by the presence of slope and friction source terms. The effect of the friction term is two-fold: if it is computed with a Manning-type formula, it can result in an unrealistically large prediction of the shear stress in very shallow regions near wet/dry boundaries, or even cause numerical overflow when particle velocities is non-zero. On the other hand the large resistance causes the front to propagate with higher surface gradient, thus limiting the region of the tip, where the lowest depth form. This eventually helps the modelling of the advancing front.

As stated above, the solution of the analytical Riemann problem accounts for the presence of a dry state, and predicts a rarefaction wave whose tail is the wet interface, propagating on the dry bed with speed $U_{WD}=U_{wet}+2\sqrt{gh_{wet}}$ (see section 2.2). This implies that if some sort of artificial wetting is used over the whole domain, then the Riemann solver would predict a wrong wave structure, made of a non-physical shock instead of the rarefaction wave. If the *star* solution for very low values of the threshold depth can be very similar to the solution in the rarefaction wave, the speed of this non-physical shock remains much slower than speed of the tail of the rarefaction. Toro (2001), demonstrates this issues by propagating a dam break over a flat bed and analysing the delay of the threshold approach over the correct one.

In order to avoid the above problem, a simple technique is employed here: it still makes use of a threshold method, but takes advantage of the possibility yield by the exact Riemann solver employed to manage wet-dry transition. The method is extremely simple but reveals to produce reasonable results with both the first order Godunov and the second order WAF scheme. It consists to evaluate the flux function only if the depth is higher than the threshold. The flux function is called both by the first and the second order solver, to evaluate the flux respectively at the interface, and at the various regions of the wave structure.

This implies that a real dry state exists and the Riemann solver yields corrects wave speed.

The drying phase is, if possible, a more critical point, as no numerical schemes is naturally able to provide a transition from a finite positive depth to zero. During a drying phase negative depth occur almost everywhere along the WD interface. Thus a procedure similar to the one discussed in section 3.2.1 is employed: the only difference is that the technique is here organised over a single step, as no prediction-correction method is present. An exact mass balance is met, while the momentum law is obviously violated. This feature has not been tested exhaustively, and will be examined carefully in future works. It has to be stressed that, probably because of its minor relevance in the field of flood risk assessment, the drying problem has been paid minor attention in the fluvial hydrology, while it is still a central topic in the coastal research, because it plays a crucial role in the correct modelling of the morphodynamics in the swash zone (Briganti and Dodd, 2008).

> *"Pochi fra gli scienziati teorici impegnati in un programma di ricerca prestano eccessiva attenzione alle 'confutazioni'. Essi seguono una politica di ricerca a lungo termine che anticipa tali confutazioni. Questa politica, o ordine di ricerca, è ciò che viene programmato – più o meno dettagliatamente – nell'euristica positiva del programma [...]" L'euristica positiva consiste di un insieme parzialmente espresso di proposte e suggerimenti su come cambiare, sviluppare, le 'varianti confutabili' del programma di ricerca [...] L'euristica positiva traccia un programma che prefigura una catena di modelli sempre più complicati che simulano la realtà." (I. Lakatos, La metodologia dei programmi di ricerca scientifici, 1974)*

4.2 Validation tests

In this section several validation tests are presented. Some tests are aimed at verifying the capabilities of the numerical methods used to correctly solve the SWE set, and compare numerical and analytical solutions. Others are used to assess the performance of both the SWE conceptual model and the numerical method to simulate complex flows. Some of them involve 1D flows, others are intrinsically 2D, but the code tested solves the 2D SWE for all cases.

4.2.1 1D dam break

This test simulates the sudden collapse of an idealised dam which initially separates two regions with different water depth at rest (h_u and h_d water depths respectively upstream and downstream the dam). The test is intrinsically 1D. The consequent dynamic is of a rarefaction wave that propagates upstream in the region with the larger initial depth. The downstream dynamic is instead dependent on the presence of a positive depth in the lower depth region: in the case of propagation over a dry bed the rarefaction wave which propagates upstream the dam location has its tail at the dry-wet interface; when a wet downstream bed is simulated a shock forms and moves forwards over the wet region. Both cases are simulated and compared with the analytical solutions (Stoker, 1957).
Initial conditions for case 1 are (h_u=2m, h_d=1m, uh=vh=0ms^{-1}).
Initial conditions for case 2 are (h_u=1m, h_d=0m, uh=vh=0ms^{-1}).
Results are presented in Figures (4.5 - 4.8).

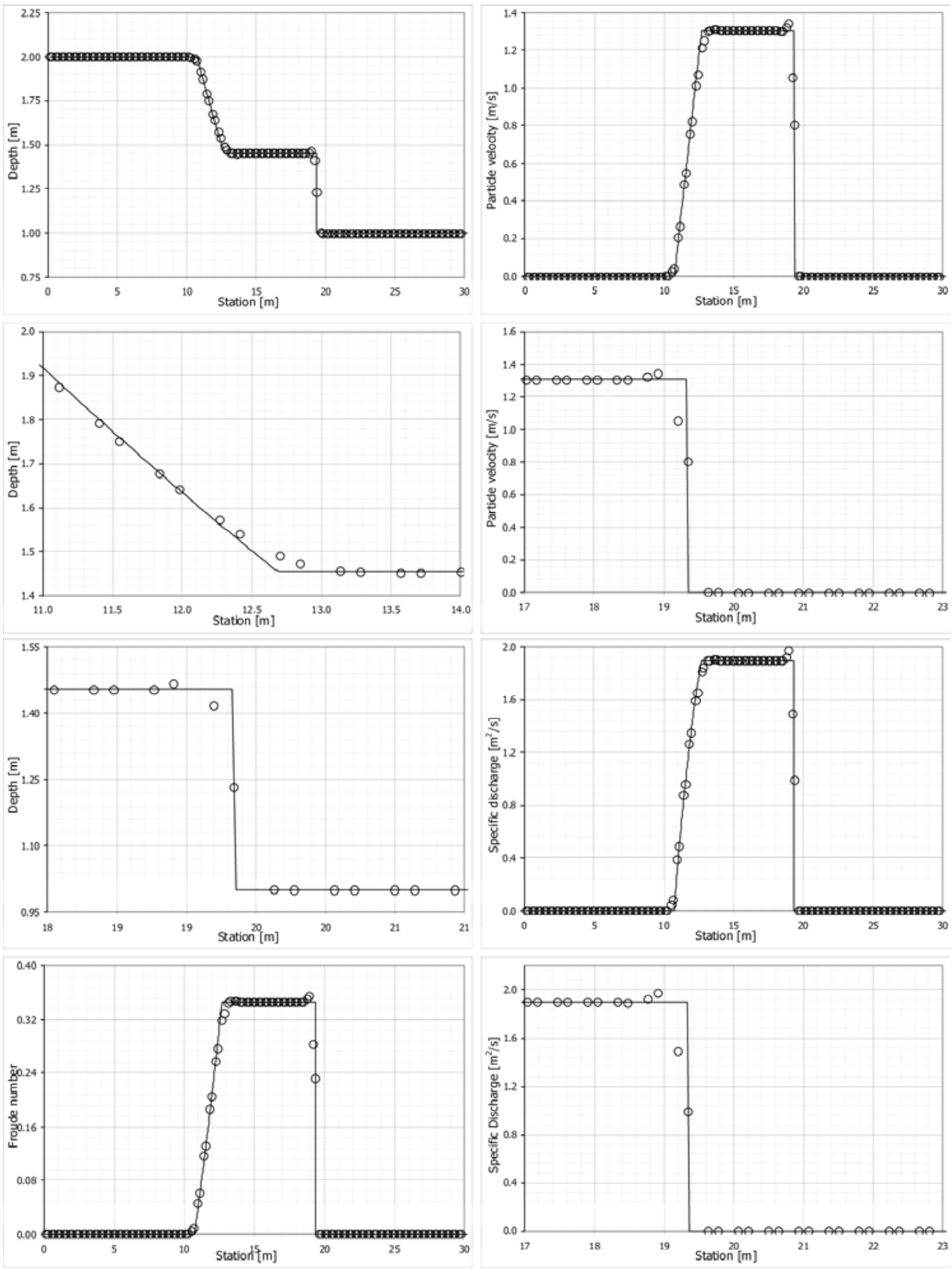

Figure 4.5 – 1D dam break t=1s – Case 1: wet bed; analytical solution (trace) compared to numerical solution (circles), for depth (h), specific discharge and particle velocity (u) along x-axis (uh), Froude number.

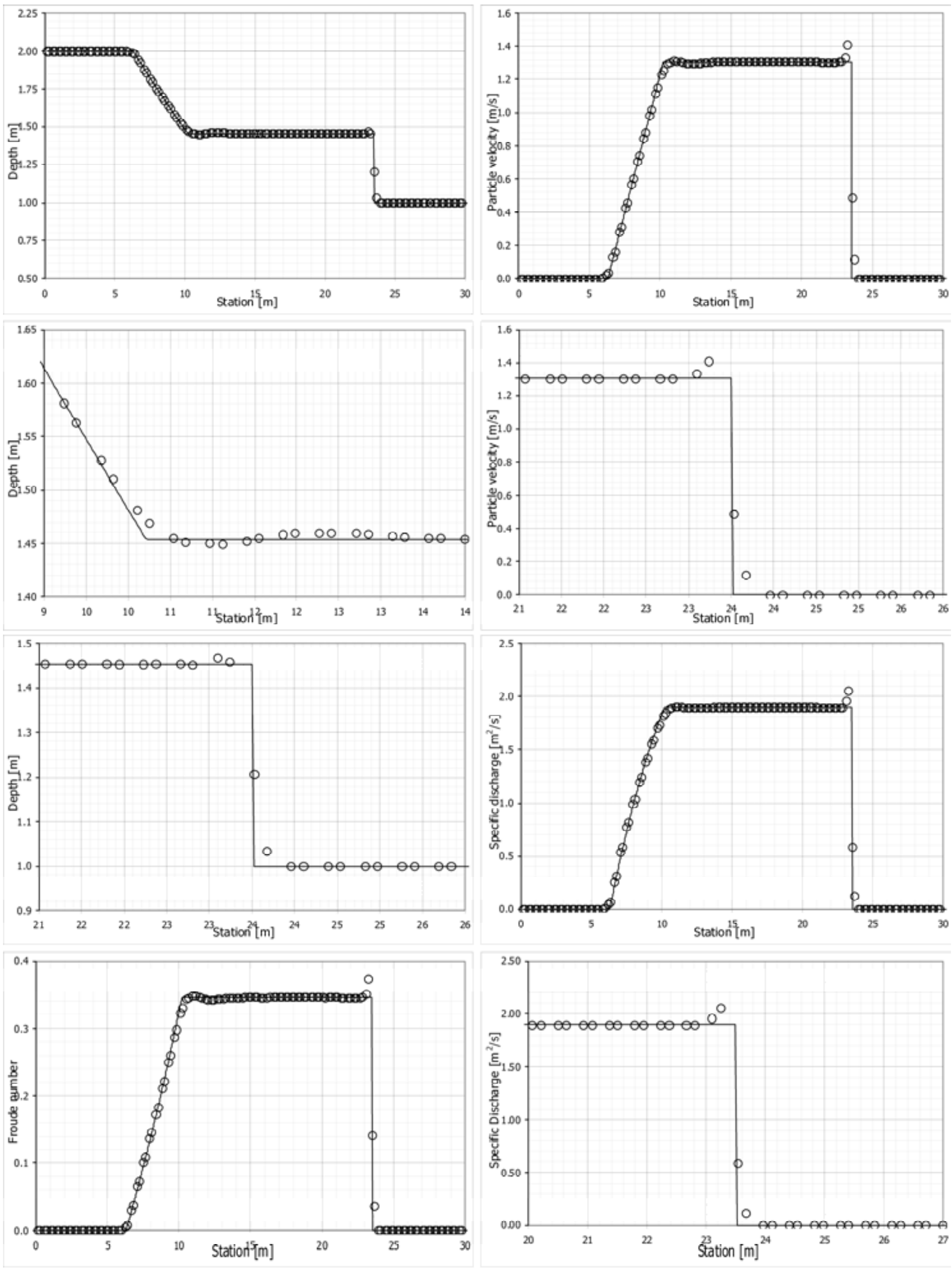

Figure 4.6 – 1D dam break t=2s – Case 1: wet bed; analytical solution (trace) compared to numerical solution (circles), for depth (h), specific discharge and particle velocity (u) along x-axis (uh), Froude number.

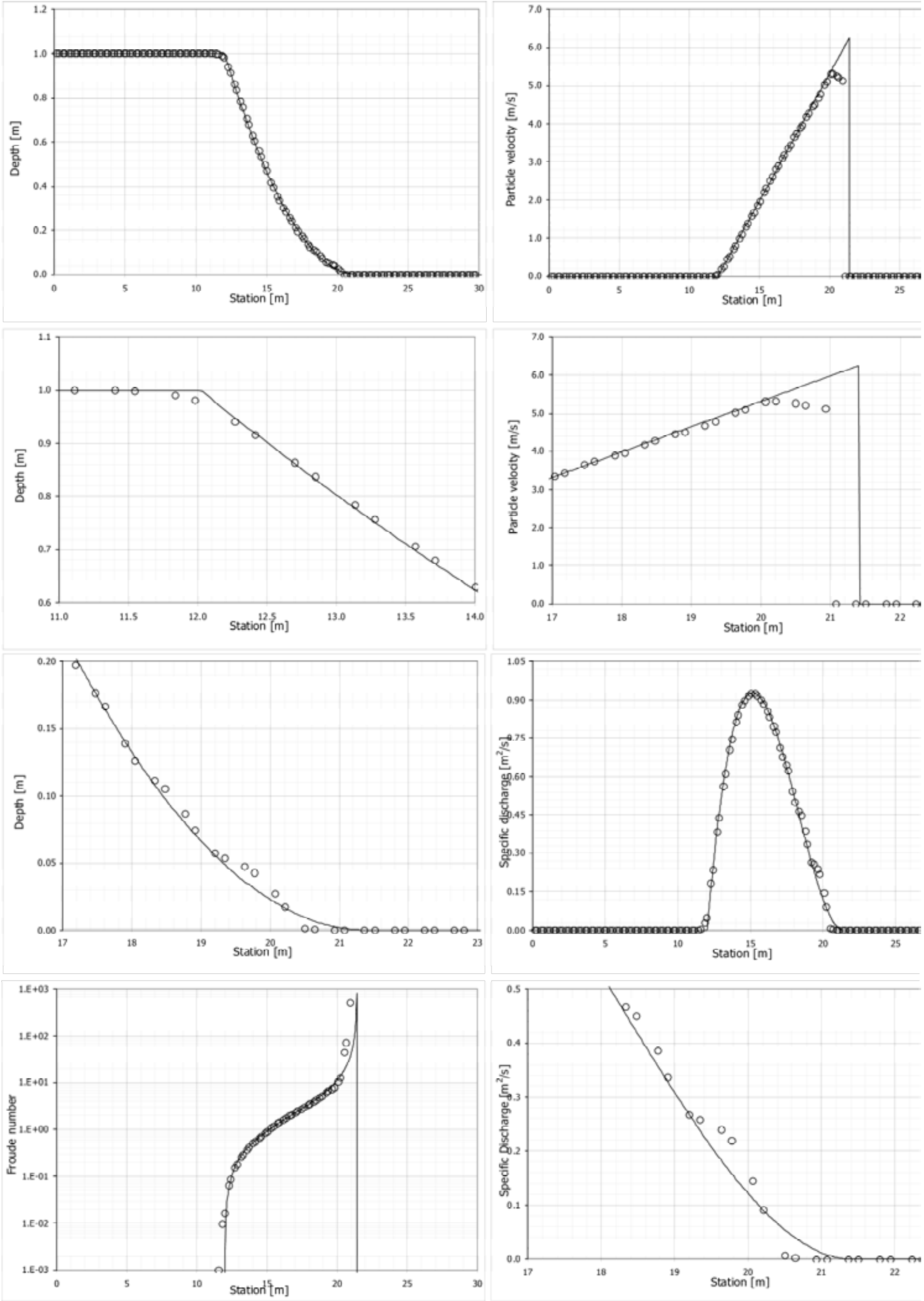

Figure 4.7 – 1D dam break t=1s – Case 2: dry bed; analytical solution (trace) compared to numerical solution (circles), for depth (h), specific discharge and particle velocity (u) along x-axis (uh), Froude number.

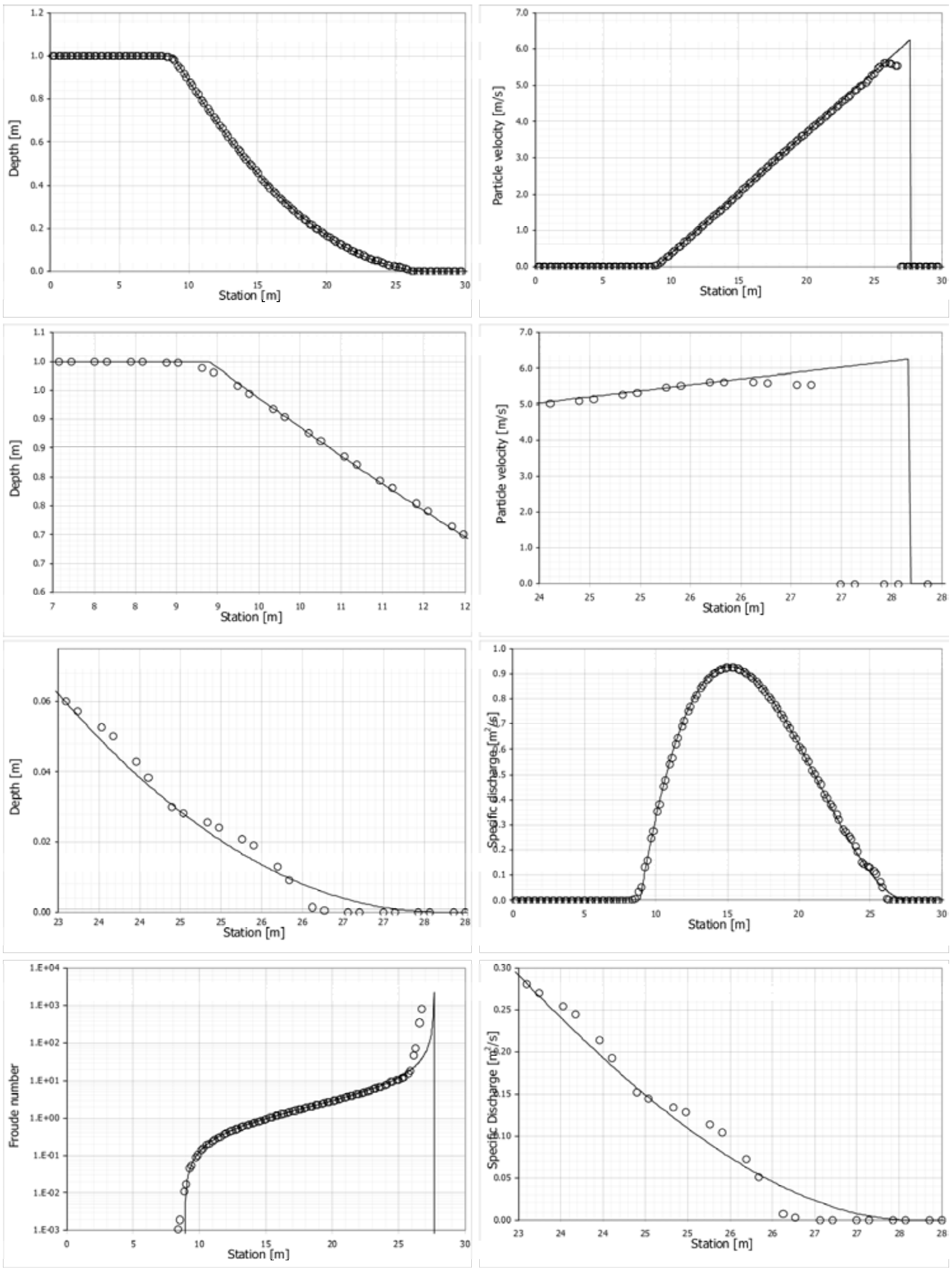

Figure 4.8 – 1D dam break t=2s – Case 2: dry bed; analytical solution (trace) compared to numerical solution (circles), for depth (h), specific discharge and particle velocity (u) along x-axis (uh), Froude number.

4.2.2 2D oblique shock

This is a fully 2D test, simulating a stationary shock that develops when a supercritical flow in a rectangular channel is deflected by the right wall of the channel which is bent at an angle θ_{wall} (see Figure 4.9). The channel is 40m long and 30m wide; upstream boundary conditions are h_u=1m, uh=8.57ms^{-1}, vh=0ms^{-1}, Froude number is then 2.74; transmissive downstream boundary conditions are imposed. The oblique shock originates at the section at which the channel is restricted, and forms an angle θ_{shock} with the wedge, which can be determined examining the Rankine-Huguinot jump conditions across the shock itself: using a wall angle $\theta_{wall} = 8.95°$, the angle formed by the shock is 30°, the water depth downstream the shock (h_d) is 1.5 m, the Froude number is 2.075 (Alcrudo and Garcia-Navarro, 1993).

Numerical results yield a very good approximation of the exact solution, with the shock sharply reproduced, and located correctly. The accuracy is not assessable by visual inspection of plots, thus table 4.1 summarises the relative error between the numerical and the analytical solution for the shock angle, the depth field upstream and downstream the shock. Non-dimensional root mean square errors are determined as:

$$RMSE = \frac{1}{N}\sqrt{\sum_{N}\left(\frac{\square_{ex} - \square_{num}}{\square_{ex}}\right)^2} \quad (4.1)$$

where the group of cells involved in the summation is different for each of the three quantities examined. For the evaluation of the shock angle prediction accuracy, the group of cells is formed by the one belonging to the “head” of the shock. A cell is assumed to be at the head of the shock if its depth is above 1.01 m, and at least one of its neighbouring cells has a depth lower than $1.0+1.0\cdot10^{-5}$. For the remaining two quantities, namely the depths in the two regions, the cells examined are the ones located respectively upstream and downstream the exact location of the shock, that is the red line in Figure 4.10. Note that the downstream mean error is considerably higher than the other two, because the shock is numerically represented by an abrupt, but still smooth, jump in the water depth: some cells with an intermediate depth (see lower panel of Figure 4.10) belonging to the “downstream” region, are compared against the higher depth, namely 1.5m, and this significantly lowers the overall accuracy.

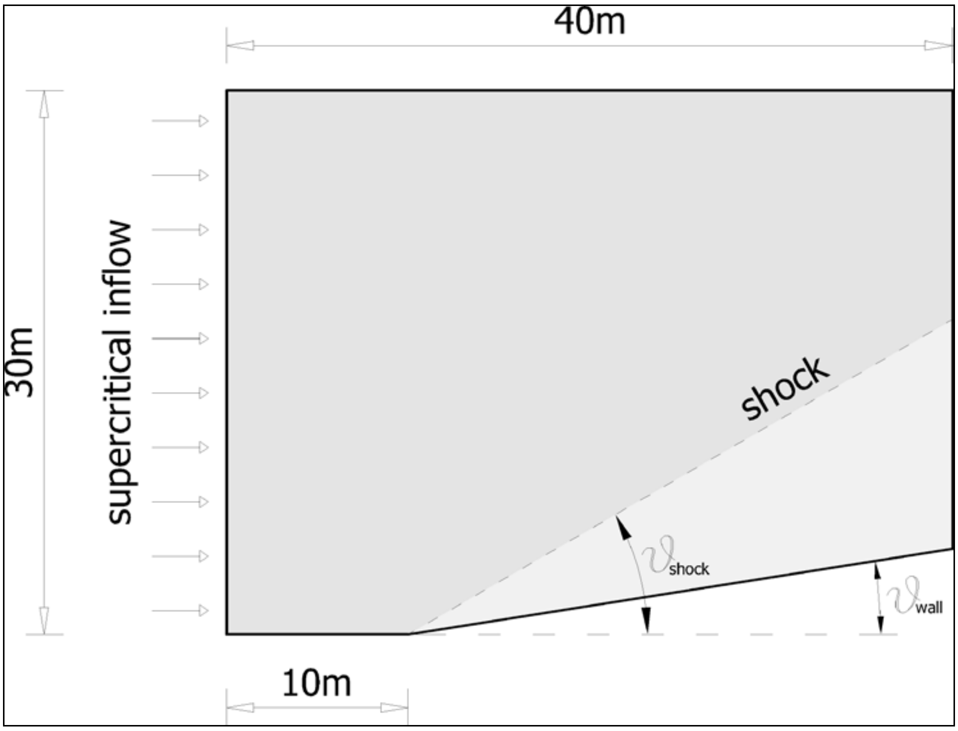

Figure 4.9 – Oblique shock test: sketch of the rectangular channel. Dark and light grey areas are respectively the lower (h_u) and higher (h_d) depth regions.

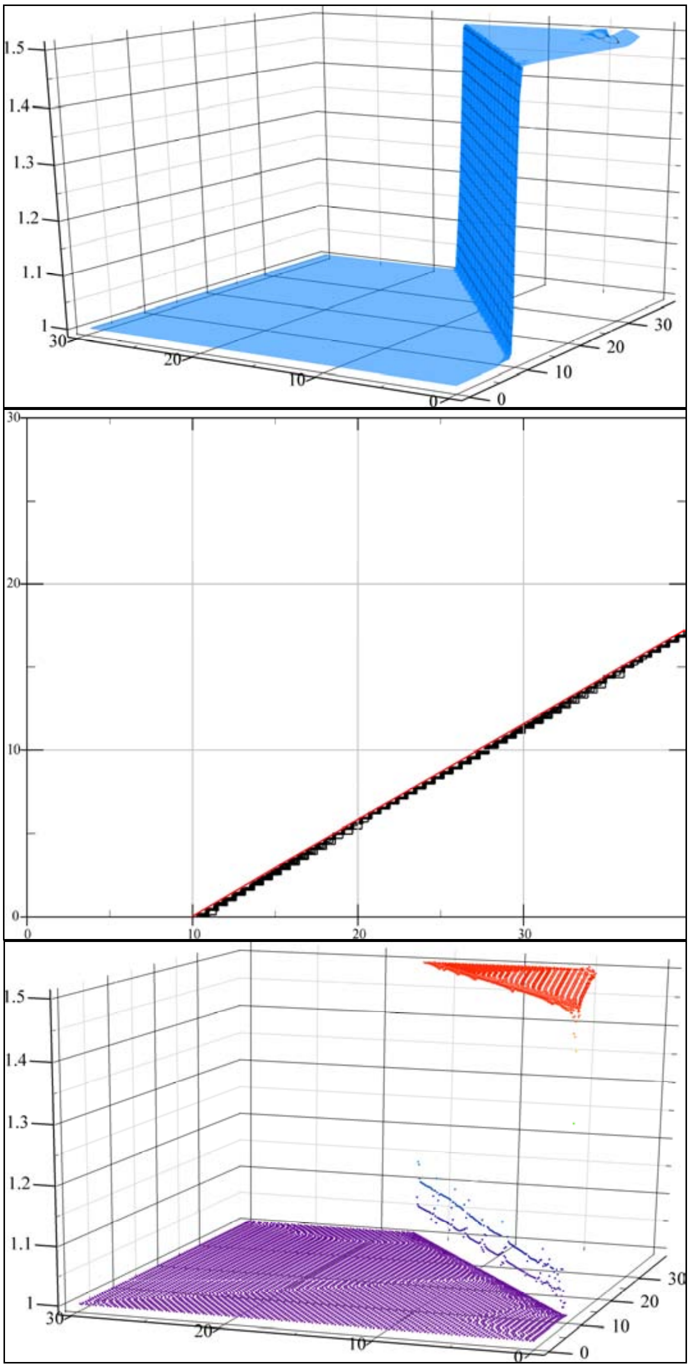

Figure 4.10 – Water depth for the oblique shock test; upper panel shows a 3D view of the channel; in the middle panel 20 contours are plotted and the red line is the exact location of the shock; the lower panel shows the WSE as a scatter field.

Table 4.1- Oblique shock test accuracy:
non-dimensional RMSE [m]

θ_{shock}	$5.2 \cdot 10^{-3}$
h_u	$1.0 \cdot 10^{-10}$
h_d	$1.06 \cdot 10^{-1}$

4.2.3 Dam break over 90° bend

This is a fully 2D experimental test conducted at the laboratory of the Civil Engineering Dept. of the Univ. Catholique de Louvain, Belgium, within the CADAM project (Soares Frazão et al. 2000), and successively improved (Soares Frazão and Zech, 2002). The experiment reproduces a dam break in a rectangular channel with a 90° bend. The installation is depicted in Figure 4.11. The channel is 0.495 m wide, is made of glass, the reach upstream the bend is longer than the downstream one. The upstream reservoir has dimensions of 2.44 m x 32.39 m. The whole channel has a horizontal bed, but its elevation is 0.33m higher than the bottom of the reservoir with a vertical step at the gate position. The outlet of the channel is open (free chute).

The initial conditions are of dry bed in the channel, and water at rest in the reservoir with surface level at 0.25m above channel bed.

The channel roughness Manning coefficient was measured for stationary flow, and the suggested value is 0.013 s/m$^{1/3}$.

The numerical code does not account for discontinuous variations of the bed across the domain, but neglecting the 0.33m high step would introduce a discrepancy in the celerity of the rarefaction that propagates into the reservoir once the gate has been removed. This assumption is not expected to affect the initial phase of the experiment much, as the dam break wave at early stages is mainly influenced by the depth above the channel bed; however, the slower speed of the rarefaction would later modify the discharge exiting the reservoir consistently, leading to a loss of accuracy.

Thus the two bed elevations are connected by a smooth, though steep, transition, as in Figure 4.12.

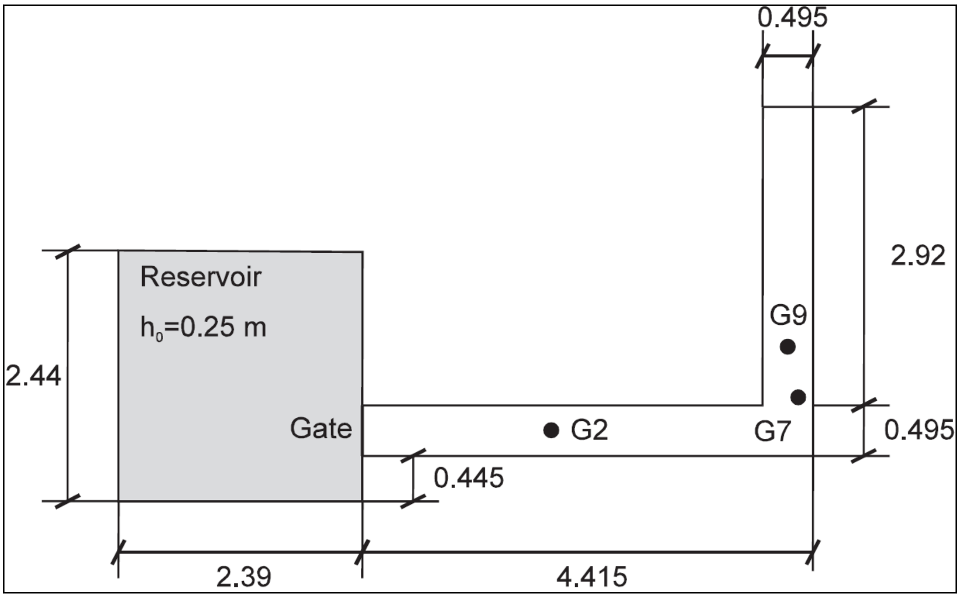

Figure 4.11 – Dam break over 90° bend: schematic view of the experimental setup

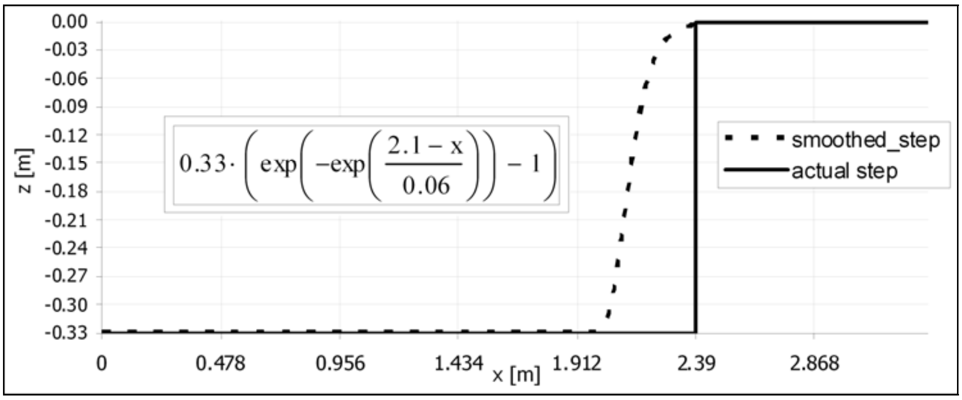

Figure 4.12 – Dam break over 90° bend: function used to smooth the step of the bed between the reservoir and the channel.

The numerical results are compared against the experimental results after Soares Frazão and Guinot (2007). The comparison involves the water level measurements at the three locations shown in Figure 4.11. The three time series are plotted in Figure

4.13. The overall accordance is good for the evolution of the surface level. The prediction of the arrival time is impressive, with gauge G7 even accounting for the little jump in the front tip, which is caused by the advancement of the tip prior to the collapse of the column of water that had previously risen hitting the outer wall of the bend. The evolution of the WSE is well simulated at all three gauges. The low frequency oscillations downstream the bore are completely filtered out, and no numerical model presented so far is able to model them. The prediction of the bore receding towards the reservoir is poor both in terms of maximum predicted level at the front of the shock and in terms of its speed. The numerical shock is considerably slower and other numerical models show a similar behaviour (Zhou et al. 2004). The discrepancy cannot be imputed to a wrong choice of roughness parameter, as its influence, using plausible values of the Manning coefficient for glass, has been empirically shown to be negligible. The roughness parameter value was calibrated by Soares and Zech (2002), who conducted the experimental simulations, for uniform flow. However the same authors suggest that some discrepancies can be due to errors in the measurements. Apart from the value of the Manning coefficient (or any other roughness parameter obtainable from the Chezy formula), the modelling of the bottom roughness by means of a Chezy-type formula can introduce some discrepancies, because the flow conditions that appear in the physical model are markedly different from the ones for which this formula was deduced. The experiment shows a distinct three dimensional dynamic, at the dam location, in the first phase after the collapse, and at the bend. These peculiarities are not taken into account by the SWE model.

The receding bore and the 2 quasi-steady wave patterns are clearly visible in figure Figure 4.14: the first pattern, symmetrical about the reach centreline, originates at the corners of the gate and develops upstream the bore; the second, anti-symmetrical, originates at the inner corner of the bend and develops downstream the bend. These reflections pattern can be the cause of the overestimation of WSE at gauge G9, as a small error in the location of a steady wave front results in a persistent error through most of the simulation.

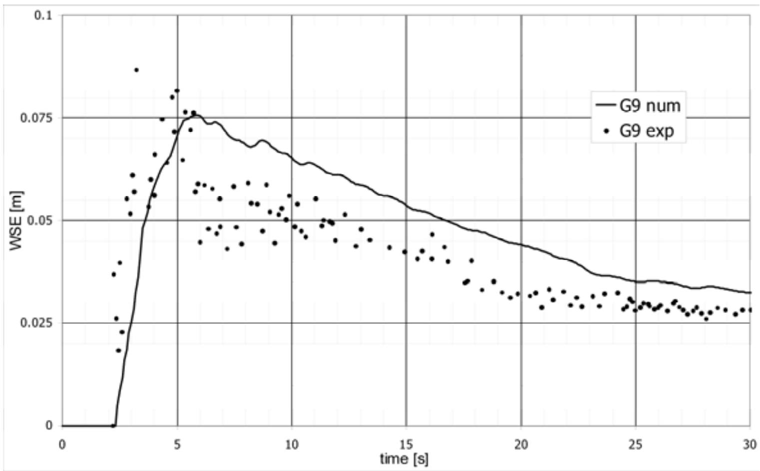
0.1
0.075
0.05
0.025
0
WSE [m]
0
5
10
15
20
25
30
time [s]
G9 num
G9 exp

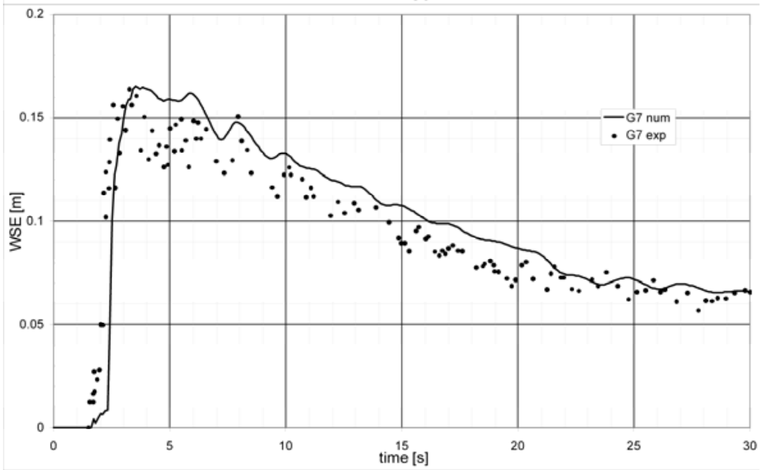
0.2
0.15
0.1
0.05
0
WSE [m]
0
5
10
15
20
25
30
time [s]
G7 num
G7 exp

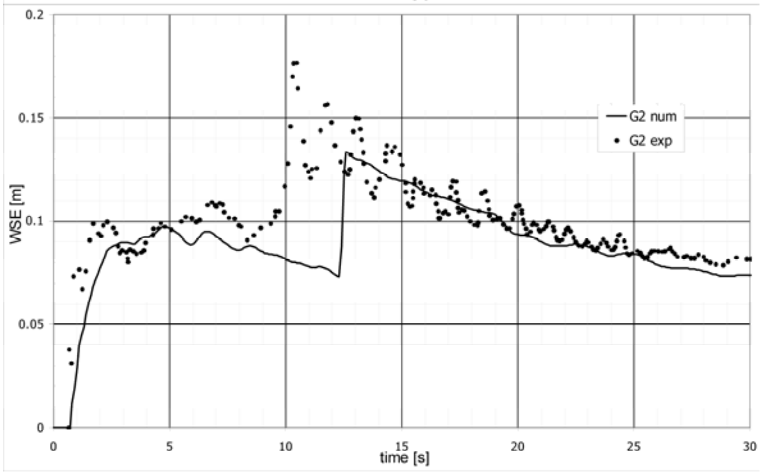
0.2
0.15
0.1
0.05
0
WSE [m]
0
5
10
15
20
25
30
time [s]
G2 num
G2 exp

Figure 4.13 – The three experimental water level series (dots), compared to numerical results (line).

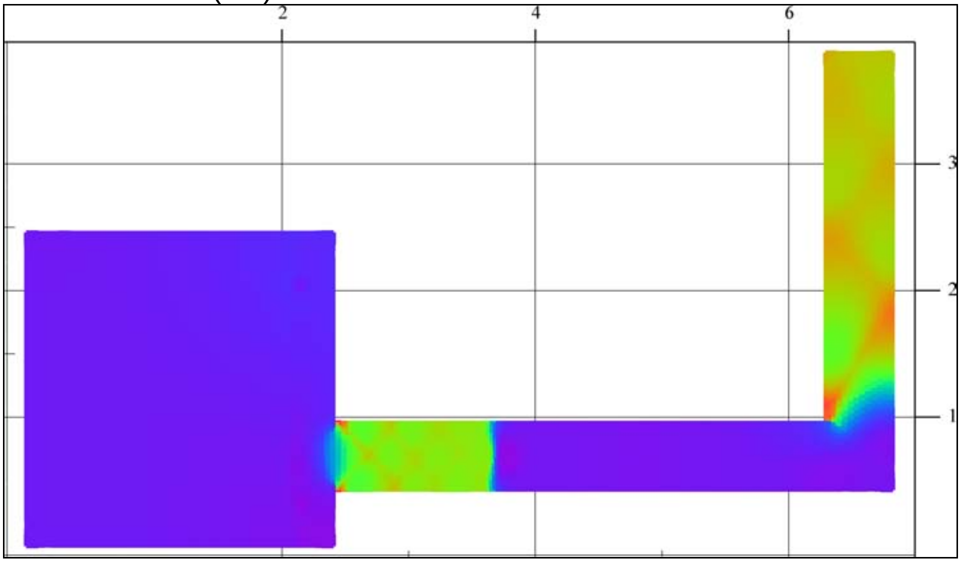

Figure 4.14 – Water surface level for the numerical simulation at time t=14 s (colour transition from low to high levels is red→green→blue→purple).

4.2.4 1D flow over bump

This is a 1D steady state test with variable bed elevation and no wet-dry interface. A uniform subcritical current in a rectangular frictionless channel flows over a bump of the bed. Three cases are simulated: i) the flow is subcritical both upstream and downstream the bump; ii) the flow passes through critical condition on the bump and maintains supercritical condition downstream the bump; iii) the flow passes through the critical condition on the bump but the subcritical boundary condition imposed at the downstream end of the channel forces a drowned hydraulic jump.

The numerical results are compared against the analytical solution obtained from the momentum conservation 1D equation.

This test assesses the accuracy of the source term management strategy and the ability of the whole model to correctly locate transitions through critical depth.

Case 1 - Subcritical flow with no critical transitions: the imposed boundary conditions are h=2m and uh=4.42 m^2/s both upstream and downstream.

Case 2 – Single transition through critical state: a unit discharge of uh=1.53 m^2/s is imposed at the upstream boundary and a depth of h=0.66 m (subcritical flow) is imposed downstream until the flow develops into a supercritical state and no downstream boundary condition is needed any longer.

Case 3 – Double transition through critical state: the subcritical upstream flow passes trough critical state at the top of the bump and develops again into a subcritical flow through a bore. A unit discharge of 0.18 m^2/s is imposed upstream and a depth of 0.33 m downstream, both being subcritical states.

The comparison with the reference solution shows a good agreement for all three cases (Figure 4.15 to Figure 4.17). The unit discharge highlights the inaccuracies of the bed source term discretization: the small jumps reveal the expected non exact balance, but their magnitude is extremely small. Case 1 shows a slight overestimation of the water level upstream the bump. All three cases suffer from a problem associated with the treatment of the bed slope term at the boundary: the problem is likely to be due to the approximations used when calculating nodal values for the ghost cells to be used in the limiter functions, as exposed in section 4.1.3.2: this conjecture is supported by the fact that a first order Godunov simulation does not reveal the same issue. Further investigation is being carried on. This problem causes a small 2D perturbation, in form of 2 waves, that start at the lateral walls of the channel and converge to the centre axis. The effect is more visible for unit discharge distribution for case 3. It’s worth recalling that a section along the axis of the channel is used for all the graphical comparisons.

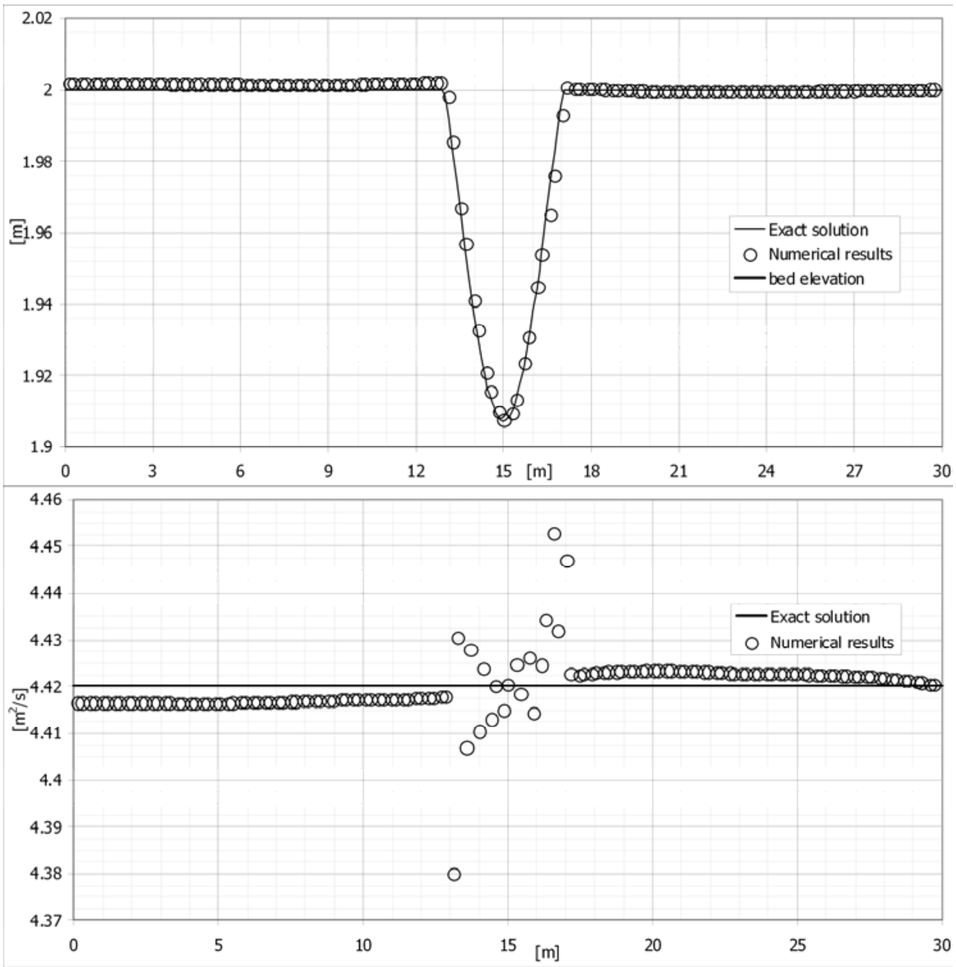

Figure 4.15 – Flow over bump - Case 1 – Water surface elevation (top) and unit discharge (bottom) for the subcritical case with no transition.

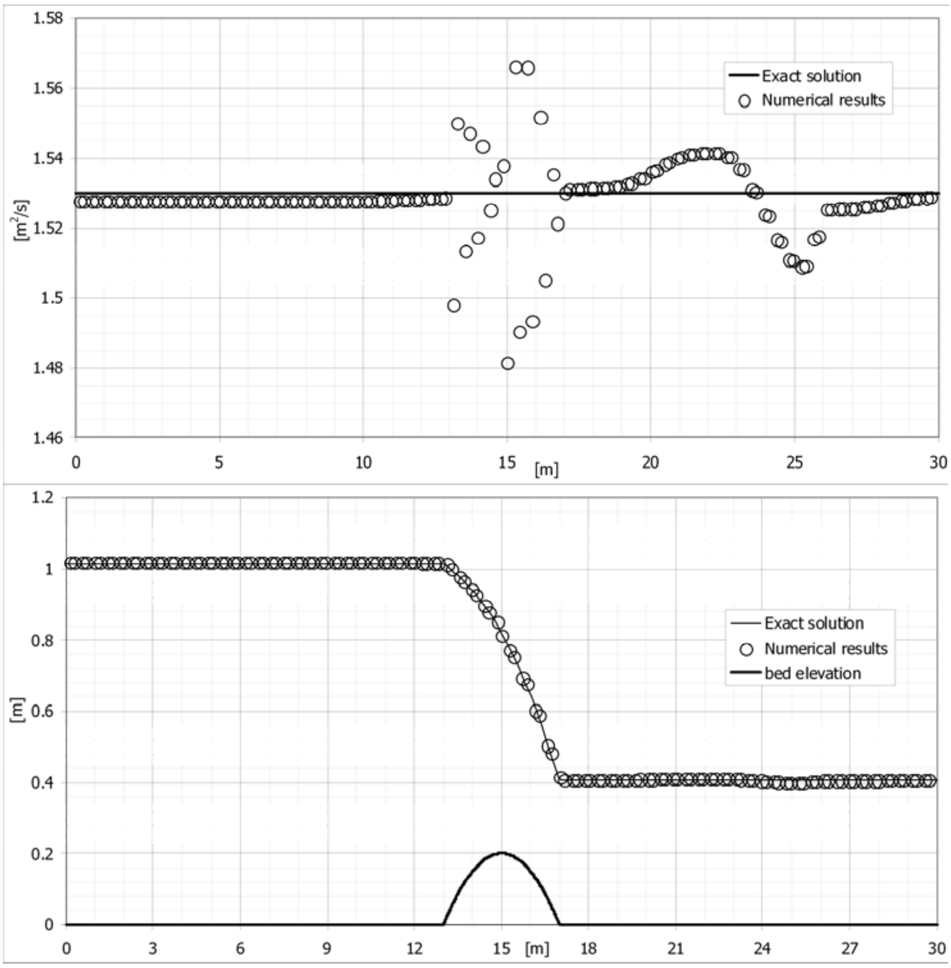

Figure 4.16 – Flow over bump - Case 2 – Water surface elevation (top) and unit discharge (bottom) for the single transition case.

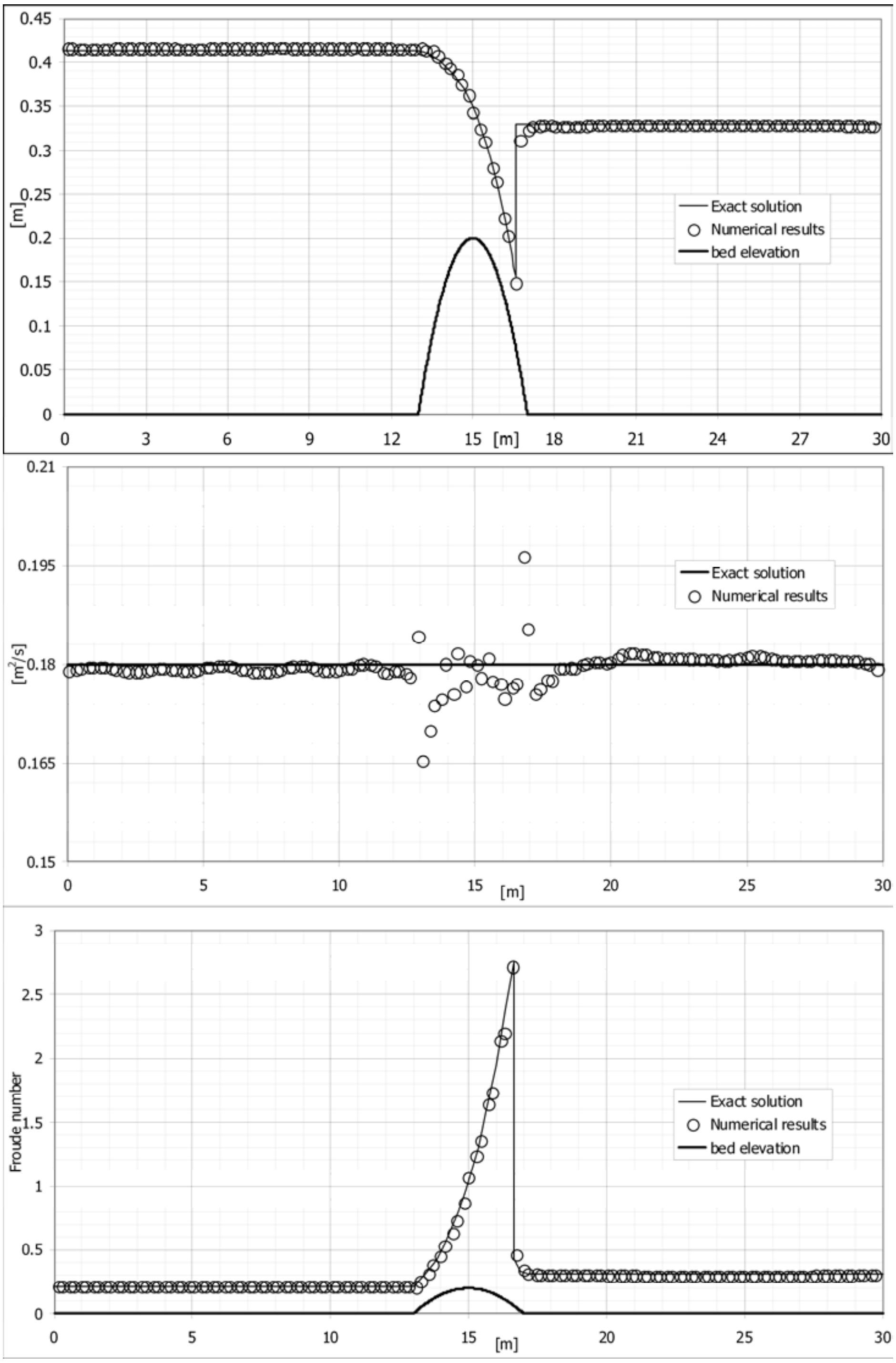

Figure 4.17 – Flow over bump - Case 3 – Water surface elevation (top), unit discharge (middle) and Froude number (bottom) for the double transition case.

5. Conclusions

In this thesis the numerical approach to the simulation of floods has been investigated. The proposed methods are based on the solution of the Shallow Water Equations (SWE).

In the first part of the study a simplified version of the SWE, namely the parabolic model, has been analysed and its capabilities investigated. The conceptual model employs the zero-inertia assumption, thus its application would be restricted to slowly varying events, dominated by gravitational force. Several attempts were made in the past to provide the modeller with various types of guidelines to decide whether a simplified wave model was suitable for the simulation of a certain event. The validity of such criteria are limited and their efficacy often denied. Nonetheless, the increased availability and precision of topographical information, often covering large areas, is encouraging the use of simplified SWE models, which provide robustness and relatively lower computational requirements, if compared to full dynamic models. These models are attractive also because several side issues, such as the wet-dry transition or the source terms management, are dealt with naturally or with limited difficulties. These aspects altogether determine the need of a more precise assessment of the capabilities of these models, especially when complex configurations, such as 2D flows, are to be modelled. A comparison with a controlled physical simulation of a dam-break propagation over a narrow, highly sloping valley, was chosen to accomplish the assessment. The analysis of results allows to state that the NI (Non Inertia) approximation, even if it fails to reproduce some local phenomena such as bores and run-up, is capable to simulate the propagation of such very impulsive waves over complex topography.

The second part of the thesis deals with the numerical solution of the full dynamic 2D SWE set. A code has been developed which is able to solve the hyperbolic set of equations on irregular unstructured mesh, maintaining second order of accuracy in both space and time. The technique employed, namely the WAF method by Toro (1999a, 1999b), has been adapted to correctly handle highly irregular meshes. The wet-dry transition handling and the treatment of source terms have been aimed at limiting the recourse to non-physical procedures, such as the ones often appearing in literature, by means of a better posed, though not numerically exact, efficient method. Several tests have been performed based on the comparison with both analytical solutions and experimental data. The benchmarks were able to assess the good quality of the approach proposed, and a high level of accuracy, comparable to the more recent numerical works, can be asserted. The comparison with the experimental data, in particular, allows to highlight the capability of the model to handle also non idealised events, where many complex phenomena simultaneously occur.

The numerical treatment of the SWE has experienced a high thrust since the methods of the gas-dynamic were transferred to this field. However many peculiar problems have emerged, and are currently not fully solved, if not at the expenses of computational efficiency (the upwinding of the source terms being the clearest example). While these numerical methods are able to preserve the high order of accuracy which can in theory justify the use of the full dynamic SWE set, they still require an amount of computational effort which indeed raises some serious suspicions about their possible employment on the simulation of large scale, real events. For these cases it is nowadays clear that the main sources of inaccuracies do not reside in the assumptions adopted in the underlying conceptual model but they are often to be seeked in the side problems treatment (boundary conditions modelling, wet-dry management, source term discretization, etc).

Future developments of this wide field will certainly be aimed at providing these models with an uncertainty assessment methodology, which can itself act as a guideline to order the possible sources of inaccuracies and thus direct the research efforts to specific areas.

References

Abbott, M. B. 1979. *Computational Hyraulics*, Pitman.

Akan, A.O., Yen, B.C., 1977. *A nonlinear diffusion wave model for unsteady open channel flow*. Proceedings of the 17th IAHR Congress, August, Baden-Baden, Germany, vol. 2, pp. 181± 190.

Akanbi, A. A. and Katopodes, N. D. 1988. *Model for flood propagation on initially dry land*, J. Hydraul. Engng, 114, 689:706.

Alcrudo F. and Garcia-Navarro P. 1993. *A high resolution Godunov-type scheme in finite volumes for the 2d shallow water equations*, Int. J. Numer. Methods Fluids 16, 489.

Ambrosi, D.1995. *Approximation of shallow water equations by Roe's Riemann solver*. International Journal for Numerical Methods in Fluids; 20:157–168.

Bates, P.D., De Roo, A.P.J. 2000. *A Simple Raster-Based Model For Flood Inundation Simulation*. Journal of Hydrology 236, 54–77

Balzano A. *Evaluation of methods for numerical simulation of wetting and drying in shallow water flow models*. Coastal Engineering 1998; 34:83–107.

Begnudelli, L., and Sanders, B. F. 2006. *Unstructured grid finite volume algorithm for shallow-water flow and scalar transport with wetting and drying* J. Hydraul. Eng., 132,4, 371–384.

Bradbrook, K.F., Lane, S.N., Waller, S.G., Bates, P.D., 2004. *Two dimensional diffusion wave modelling of flood inundation using a simplified channel representation*. International Journal River Basin Management 2, 211–223.

Bradford SF, Sanders BF., 2002. *Finite-volume model for shallow water flooding of arbitrary topography*. Journal of Hydraulic Engineering; 128(3):289 –298.

Briganti, R, Dodd, N. 2008. *Shoreline Motion in non-linear shallow water coastal models*. Coastal Engineering In Press, Available online 19 December 2008, doi:10.1016/j.coastaleng.2008.10.008

Brufau, P., Vàzquez-Cendòn, M. E. and Garcìa-Navarro, P. 2002. *A numerical model for the flooding and drying of irregular domains*. International Journal For Numerical Methods In Fluids 39, 247–275

Bermúdez, A., Vázquez, M.E. 1994. *Upwind methods for hyperbolic conservation-laws with source terms*. Computers and Fluids; 23(8):1049–1071.

Caleffi, V., Valiani, A., Zanni, A. 2003. *Finite volume method for simulating extreme flood events in natural channels*. Journal of Hydraulic Research 41 167–177

Chaudhry, M. H. 1993. *Open-Channel Flow*, Prentice-Hall, Upper Saddle River, N. J.

Crago, R. D., and S. M. Richards 2000. *Nonkinematic effects in storm hydrograph routing*, J. Hydrol. Eng., 5(3), 323–326.

Cunge, J.A., Wegner, M., 1964. *Intégration numérique des equations d'écoulement de B. de St. Venant par un schéma de différences finies*, La Houille Blanche No. 1, SOGREAH, Grenoble.

Cunge, J.A., Holly Jr., F.M., Verwey, A., 1976. *Practical Aspects of Computational River Hydraulics*. Pitman, London.

Cunge , J.A., Holly , F.M. & Verwey , A. 1980. *Practical Aspects of Computational River Hydraulics*. Pitman Publishing, London, 420 pp.

Di Monaco, A. and Molinaro, P. 1984. *Lagrangian finite element model of dam-break wave on dry bed versus experimental data*, Hydrosoft'84 Hydraulic Engineering Software, Proceedings of the International Conference, Yugoslavia, September 1984, pp. 2-111:2-120.

Donnell, B. P., et al. 2001. *User's guide for RMA2 version 4.5*, U.S. Army, Engineer Research and Development Center, Waterways Experiment Station, Coastal and Hydraulics Laboratory, Vicksburg, Miss.

Estrela, T., 1994. *Use of a GIS in the modelling of flows on flood-plains* In: White, W.R., Watts, J. (Eds.). Proceedings of the 2ndInternational Conference on River Flood Hydraulics, Wiley, pp.177–189

Ferrick, M. G., and N. J. Goodman 1998. *Analysis of linear and monoclinal river wave solutions*, J. Hydrol. Eng., 124(7), 728–741.

Fread, D. L. 1985. *Applicability criteria for kinematic and diffusion routing models*, Laboratory of Hydrology, National Weather Service, NOAA, U.S. Dept. of Commerce, Silver Spring, Md.

French, R. H. 1986. *Open-Channel Hydraulics*, McGraw-Hill, New York.

Harten A., 1983. *High Resolution Schemes For Hyperbolic Conservation Laws*. J. Comput. Phys. 49:357-393.

Harten A. 1984. *On a class of High Resolution Total-Variation-Stable Finite. Difference Schemes*; SIAM J. Numer. Anal., V21, pp. 1-23

Heniche M, Secretan Y, Boudreau P, Leclerc M., 2000. *A two-dimensional finite element drying–wetting shallow water model for rivers and estuaries*. Advances in Water Resources, Elsevier Science; 23:359 –372.

Horritt, M. S. and P. D. Bates, 2001. *Predicting floodplain inundation: raster-based modelling versus the finite-element approach* Hydrological Processes 15, 825–842

Horritt, M.S., 2002. *Evaluating wetting and drying algorithms for finite element models of shallow water flow* International Journal for Numerical Methods in Engineering 55, 835–851.

Hubbard ME, Garcia-Navarro P., 2000. *Flux difference splitting and the balancing of source terms and flux gradients*. Journal of Computational Physics; 165(1):89–125.

Ip, J.T.C., Lynch, D.R., Friedrichs, C.T., 1998. *Simulation of estuarine flooding and dewatering with application to Great Bay, New Hampshire*. Estuarine, Coastal and Shelf Science 47, 119–141.

Isaacson, E., Stoker,J.J., Troesch, A., 1958, *Numerical solution of flow problems in rivers*, Journal Of Hydraulic Engineering ASCE, Vol 84.

Jiang, Y.W., Wai, O.W.H., 2005. *Drying-wetting approach for 3D finite element sigma coordinate model for estuaries with large tidal flats*. Advances in Water Resources 28, 779–792.

Kant, I., 1787. *Kritik der reinen Vernunft*, *Transzendentale Analytik* (*Critique of Pure Reason, Transcendental Analytic*). Second Edition.

Katopodes, N. D., and Strelkoff, T. 1977. *Hydrodynamics of borderirrigation-complete model*. J. Irrig, and Drain. Div., ASCE, 103(3),309-323.

Katopodes, N., and Strelkoff, T. 1978. *Computing two-dimensional dam-break flood wav*es J. Hydraul. Div., Am. Soc. Civ. Eng., 104~9, 1269–1288.

Kennedy, A.B., Chen, Q., Kirby, J.T., Dalrymple, R.A., 2000. *Boussinesq modelling of wave transformation, breaking and runup. I: one dimension*. Journal of Waterway, Port, Coastal and Ocean Engineering 126, 39–47.

King, I. P. 2000. *RMA2 Version 6.6 User Manual*, Publication of Resource Management Associates, Inc., Suisun, Calif.

Kowalik, Z., Murty, T.S. 1993 *Numerical simulation of two-dimensional tsunami runup* Marine Geodesy vol.16, no.2, 87-100

Lax P.D. and Wendroff B., 1960. *Systems of Conservation Laws*. Comm. Pure Appl. Math, 13:217-237.

Liang, D., Binliang, L. and Falconer, R. A., 2007. *Simulation of rapidly varying flow using an efficient TVD–MacCormack scheme*. International Journal For Numerical Methods In Fluids. 53, 811–826

Liao C. B., Wu, M. S., and Liang, S. J., 2007. *Numerical simulation of a dam break for an actual river terrain environment*. Hydrological Processes. 21, 447–460

Leendertse, J.J., 1987. Aspects of SIMSYS, A System for Two-Dimensional Flow Computations. RAND Publication R-3572-USGS, February.

Lynch, D. R. and Gray, W. G. 1980. *Finite element simulation of flow in deforming regions*, J. Comp. Phys., 36, 135±153.

Ma Dong-Jun, Sun De-Jun and Yin Xie-Yuan, 2007. *Solution of the 2-d shallow water equations with source terms in surface* *elevation splitting form* Int. J. Numer. Meth. Fluids; 55:431–454

MacArthur, R.C., Dexter, J.R., Smith, D.J., King, I.P., 1990. *Two dimensional finite element simulation of the flooding characteristics in Kawainui Marsh, Hawaii*. In: Proceedings of 1990 National Hydraulic Engineering Conference, ASCE, New York, 0-87262-774-8, pp. 664–669.MacArthur et al. (1990)

Martin, C.S., Fazio, F.G., 1969, *Open channel surge simulation by digital computer*, Journal Of Hydraulic Engineering ASCE, Vol 95.

Mei Chiang C., 1999. *The applied dynamics of Ocean surface waves* in Advanced Series on Ocean Engineering, v.1, Eds. World Scientific Co. Pte. Ltd, Singapore.

Molls, T., Zhao, G., Molls, F., 1998. *Friction slope in depth-averaged flow*. Journal of Hydraulic Engineering 124, 81–85.

Nielsen, C., Apelt, C., 2003. *Parameters affecting performance of wetting and drying in a two-dimensional finite element long wave hydrodynamic model*. Journal of Hydraulic Engineering 129 (8), 628–636.

Okamoto, T., Kawahara, M., Ioki, N., and Nagaoka, H., 1992. *Two-dimensional wave run-up analysis by selective lumping finite element method* Int. J. Numer. Methods Fluids, 14, 1219–1243.

Perumal, M., and Sahoo, B., 2007. *Applicability criteria of the variable parameter Muskingum stage and discharge routing methods*. Water Resources Research, VOL. 43, W05409, doi:10.1029/2006WR004909

Ponce, V.M., 1989. *Engineering Hydrology*, Principles and Practices, Prentice-Hall, Upper Saddle Rive, N. J.

Price, R.K., 1974. *Comparison of four numerical methods for flood routing*. ASCE J. Hydrani. Div., 100(HY7): 879-899.

Prestininzi, P., Fiori, A., 2006. *A two-dimensional parabolic model for flood assessment* Italian Journal Of Engineering Geology And Environment , 1.

Roe, P.L., 1981. *Numerical Algorithms For The Linear Wave Equation*. Technical Report 81047, Royal aircraft Establishment, Bedford, UK

Roe, P.L., 1983. *Some contributions to the modelling of discontinuous flows*. In Proceedings of the SIAM/AMS Seminar, San Diego.

Romanowicz, R., Beven, K.J., Tawn, J., 1996. *Bayesian calibration of flood inundation models*. In: Anderson, M.G., Walling, D.E., Bates, P.D. (Eds.). Floodplain Processes, Wiley, Chichester, 333–360

Singh, V. P., 1996. *Kinematic-Wave Modeling in Water Resources: Surface*- Water Hydrology, John Wiley, New York.

Soares Frazão, S., Morris, M., and Zech, Y., 2000. editors. *Concerted Action on Dam Break Modeling: Objectives, Project Report, Test Cases, Meeting Proceedings* CD-Rom, Univ. catholique de Louvain, Civ. Eng. Dept., Hydraulics Division, Louvain-la-Neuve, Belgium.

Soares Frazão S., and Testa, G., 1999. *3rd CADAM meeting - The Toce River test case: Numerical results analysis*

Soares Frazão, S. and Zech, Y., 2002. *Dam Break in Channels with 90° Bend* Journal Of Hydraulic Engineering 128:11 (956)

Soares Frazão, S. and Guinot V., 2007. *An eigenvector-based linear reconstruction scheme for the shallow-water equations on* *two-dimensional unstructured meshes* Int. J. Numer. Meth. Fluids; 53:23–55

Strang G., 1968. *On the construction and comparison of difference schemes*. SIAM J. Numer. Anal., 5, pp. 506-517

Stelling, G.S., 1984. On the construction of computational methods for shallow water equations. Rijkswaterstaat communication No. 35r1984.

Stoker, J. J., 1957. *Water waves*, Interscience, New York.

Stockstill, R.L.; Berger, R.C.; Nece, R.E. 1997. *Two-dimensional flow model for trapezoidal high-velocity channels* Journal Of Hydraulic Engineering – ASCE. 123,10 : 844-852

Tao, J., 1984. *A numerical model of wave running up and breaking on a beach*. Acta Oceanal Sinica 6, 693–700.

Tasi CH., 2000. *Numerical simulation of flow and bed evolution in alluvial river with levees*. PhD thesis, National University of Cheng Kung, Taiwan, ROC.

Tchamen, G.W., Andkahawita, R.A., 1998. *Modelling wetting and drying effects over complex topography*. Hydrological Processes 12, 1151–1182.

Titov, V. V., and Synolakis, C. E., 1995. *Modeling of breaking and nonbreaking long-wave evolution and runup using VTCS-2* J. Waterw., Port, Coastal, Ocean Eng., 121~6, 308–316.

Toro, E.F., 1986. *A New Numerical Technique For Quasi-Linear Hyperbolic Systems Of Conservation Laws*. Technical Report CoA-8608, Colelge of Aeronautics, Cranfield Institute of Technology, UK

Toro, E.F., Roe, P.L., 1987. *A Hybridized High-Order Random Choice Method For Quasi-Linear Hyperbolic Systems*. In

Grönig, editor, Proc. 16th Internationale Symposium on Shock Tubes and Waves, pp 701-708, Aachen, Germany, July 1987

Toro, E.F., 1999a. *Riemann Solvers And Numerical Methods For Fluid Dynamics – A Practical Introduction*, Springer, Berlin.

Toro, E.F., 1999b. Shock-capturing methods for free-surface shallow/flows, Wiley, New York.

Toro, E.F., 2001. *Shock-capturing methods for free-surface shallow/flows*, Wiley, New York.

Tsai C.W., 2003. *Applicability of kinematic, noninertia, and quasi-steady dynamic wave models to unsteady flow routing* Journal of Hydraulic Engineering - ASCE, 129, 8, 613-627

van Albada G.D., van Leer B. and Roberts, W.W., 1982. *A comparative study of computational methods in cosmic gas dynamics*. Astron. Estrophysics, 108:76-84

van Leer B., 1973a. *Towards The Ultimate Conservative Difference Scheme I. The Quest Of Monotonicity*. Lecture notes in Phisics, 18:1663-168.

van Leer B., 1973b. *Towards The Ultimate Conservative Difference Scheme II. Monotonicity And Conservation Combined In A Second Order Scheme*. Lecture notes in Phisics, 18:163-168.

Vasiliev, O. F., 1970. *Numerical solution of the non-linear problems of unsteady flows in open channels*, Proceedings, Second International Conference on Numerical Methods in Fluid Dynamics, Berkeley, California.

Vázquez-Cendón M.E., 1999. *Improved treatment of source terms in upwind schemes for the shallow water equations in channels with irregular geometry*. Journal of Computational Physics; 148(2):497–526.

Viessman, W., Jr., and G. L. Lewis, 1996. *Introduction to Hydrology*, 4th ed., HarperCollins, New York.

Ying, Xinya, Wang, Sam, S. Y., and Abdul A. Khan, 2004. *Upwind Conservative Scheme for the Saint Venant Equations*. Journal of Hydraulic Engineering, Volume 130, Issue 10, pp. 977-987

Zanobetti, D., Lorgeré, H., Preissmann A., Cunge, J.A., 1970. *Mekong Delta mathematical model program construction*. Journal of Waterways Harbours Division 181–199.

Zelt, J.A., 1986. *Tsunamis: the response of harbors with sloping boundaries to long wave excitation*, Tech. Rep. KH-R-47. California Institute of Technology.

Zhou J.G., Causon D.M., Mingham C.G., Ingram D.M., 2001. *The surface gradient method for the treatment of source terms in the shallow-water equations*. Journal of Computational Physics; 168(1):1–25.

Zhou J. G., Causon D. M., Mingham C. G., Ingram D. M., 2004. *Numerical Prediction of Dam-Break Flows in General Geometries with Complex Bed Topography* Journal Of Hydraulic Engineering 10.1061 332

Zoppou, C., and I. C. O’Neill, 1982., *Criteria for the choice of flood routing methods in natural channels*, in Proceedings of Hydrology and Water Resources Symposium, Melbourne, pp. 75 – 81, Inst. of Eng., Barton, A. C. T.